Wood-derived Biopolymers for Photonics

by

Farsad Imtiaz Chowdhury

A thesis submitted in partial fulfillment of the requirements for the degree of

Doctor of Philosophy

in

Microsystems and Nanodevices

Department of Electrical and Computer Engineering

University of Alberta

Abstract

Currently, conventional plastics and composites that we mostly use are derived from petroleum which is a non-renewable resource. Plenty of these plastics are designed for a single purpose such as water bottles and food packaging and end up in landfills, causing significant environmental impact since the degradation rate is extremely slow and can take centuries. The unstable market of petroleum and its contribution to global warming are other concerns associated with conventional plastics. On the other hand, plant-based natural polymers or biopolymers are sustainable, yearly renewable, and environment-friendly solution to the current problem associated with conventional plastics. Biodegradable polymers such as cellulose and lignin can be obtained from plants and have applications in various fields e.g. construction, agriculture, fuel, etc.

Initially in this work, wood-derived cellulose nanocrystals (CNCs) are utilized as a matrix material to guide light in the luminescent solar concentrator. Acrylic polymer emulsion, otherwise known as PMMA, is the most commonly used polymer for such purposes. Though this polymer is biocompatible, it is not biodegradable. The recycling of acrylic polymer is also complicated and if not properly done it might release harmful fume during combustion. Here waveguides made of acrylic polymers and cellulose are fabricated with organic dyes and it is found that cellulose has the potential to be used as matrix material. Easy recyclability of a cellulose-made waveguide is another factor that is investigated, and no significant performance drop is reported when waveguided made of recycled cellulose is characterized.

Afterward, CNCs and lignin, another wood-derived polymer, have been investigated for their suitability to be used as radiative cooling material. Different structures have been proposed over the last few years for radiative cooling but most of these structures are not realistic for

mass production due to associated cost and complex fabrication process. In these works, two structures made of cellulose and lignin are found to have a cooling temperature of 3.97 °C and 3.7 °C below ambient temperature respectively, with significant cooling power. Attaching these polymer structures on the solar cells has shown a performance enhancement by lowering the operating temperature of the solar cell. By offering a very simple and low-cost fabrication process as well as compatibility with large-scale production using an earth-abundant material, these developed structures provide an excellent opportunity to mass implement biopolymers.

In the end, the scattering property of CNCs is leveraged to show their potential for enhancing the light quality of light-emitting diode (LED). White LED is the most common one and can be conveniently fabricated using phosphor and blue LED chip. It is demonstrated that CNCs can scatter the blue light effectively which would increase blue to yellow light conversion and improve the uniformity of correlated color temperature. The proposed structure for white LED has shown better light quality and ~30% enhancement in luminous flux compared to a conventional LED structure without using CNCs.

Overall, this thesis work focuses on different aspects of biopolymer properties and shows their potential application in different fields of photonics.

Preface

This thesis is an original work by Farsad Imtiaz Chowdhury under the supervision of Dr. Xihua Wang at the Department of Electrical and Computer Engineering, University of Alberta.

Chapter 2 of this thesis has been published as Farsad Imtiaz Chowdhury, Carson Dick, Lingju Meng, Seyed Milad Mahpeykar, Behzad Ahvazi, and Xihua Wang, "Cellulose nanocrystals as host matrix and waveguide materials for recyclable luminescent solar concentrators" in RSC Advances (https://doi.org/10.1039/C7RA04344A). I was responsible for experimental design, device fabrication, data analysis, and drafting the manuscript. Carson Dick was involved in experimental design. Lingju Meng and Seyed Milad Mahpeykar were involved in data analysis. Behzad Ahvazi led the group that synthesized CNC and Xihua Wang was the corresponding author and conceived this project. Xihua Wang was also involved in manuscript editing.

Chapter 3 of this thesis has been submitted to journals for publication as Farsad Imtiaz Chowdhury, Qiwei Xu, Kaustubh Sinha, and Xihua Wang, "Novel Application of Lignin Biopolymer for Radiative Cooling". I was responsible for the design of the study, fabrication, and characterization of the lignin-based radiative cooler, data analysis, and drafting the manuscript. Qiwei Xu and Kaustubh Sinha were involved in data analysis. Xihua Wang conceived and supervised the whole project. Xihua Wang was also involved in manuscript editing.

Chapter 4 of this thesis has been submitted to journals for publication as Farsad Imtiaz Chowdhury, Qiwei Xu, Kaustubh Sinha, and Xihua Wang, "Cellulose-Upgraded Polymer Films for Radiative Sky Cooling". I was responsible for the design of the study, fabrication, and characterization of the cellulose-based radiative cooler, data analysis, and drafting the manuscript. Qiwei Xu and

Kaustubh Sinha were involved in data analysis. Xihua Wang conceived and supervised the whole project. Xihua Wang was also involved in manuscript editing.

Chapter 5 of this thesis has been published as Farsad Imtiaz Chowdhury, Qiwei Xu, and Xihua Wang, "Improving the light quality of white light-emitting diodes employing cellulose nanocrystal filled phosphors" in Advanced Photonics Research (https://doi.org/10.1002/adpr.202100006). I was responsible for the design of the study, performing simulation, fabricating and characterizing samples, data analysis, and drafting the manuscript. Qiwei Xu was involved during simulation and data analysis. Xihua Wang conceived and supervised the whole project. Xihua Wang was also involved in manuscript editing.

To all my teachers and friends who helped me in this journey

"God, His angels and all those in Heavens and on Earth, even ants in their hills and fish in the

water, call down blessings on those who instruct others in beneficial knowledge."

- The Prophet Muhammad (PBUH)

Acknowledgments

I would like to start by expressing utmost gratitude to my supervisor Dr. Xihua Wang who has been a caring mentor from the first day at the University of Alberta. The work presented in this thesis was only possible because of his constant help, encouragement, and extensive knowledge. Whenever I failed to achieve the desired result, he was always there for me and encouraged me which has helped me to come this far. I am greatly thankful for the opportunities that he provided me to pursue my ambition and dreams and I am sure that my time as a doctorate student would have been very difficult if I were deprived of his great care, kindness, and impacts on my personal development which go far beyond just the grad school life.

I would also like to thank the members of my supervisory committee, Dr. Sandipan Pramanik, and Dr. Vien Van, whose constructive comments and thoughtful remarks during my program helped me to polish my research. Additionally, I have been fortunate to develop a great friendship with kind and knowledgeable lab mates Qiwei Xu, Lingju Meng, Carson Dick, and Kaustubh Sinha who contributed to my research in many ways and made my school life more fun and enjoyable.

I would also like to mention my parents, Faruk Ahmed Chowdhury and Monnu Jahan Begum, who always believed in me. Even though we were thousands of miles away, their love and encouragement always lifted my spirit whenever I felt down. I would also like to acknowledge my wife Fatema and daughter Warizah for being there for me all the time and giving continuous support and making sacrifices. Special kudos to my brother, Farhan, my sister-in-law, Kolly, and my lovely nephew, Areez whom their kindness and support made studying abroad much easier. None of my accomplishments would have had any meaning to me without the never-ending love and support from my family.

Table of Contents

List of Tables

List of Figures

Chapter 1: Introduction

1.1. Biopolymer

Biopolymers are polymeric biomolecules made of monomeric units that are bonded covalently to form larger molecules. Here the prefix 'bio' means these types of polymers are produced by living organisms. A variety of materials are termed biopolymers which are derived from sources like microorganisms, plants, or trees. Some materials are produced by synthetic chemistry from different biological sources like sugars, fats, resins, proteins, vegetable oils, etc. can also be described as biopolymer [1]. Compared to synthetic polymers produced from petroleum, most biopolymers are biodegradable by different aerobic and non-aerobic procedures in nature, sediments, or landfills [2].

1.1.1.   Motivation for developing biopolymers

In recent years, due to the huge expansion of industries across the world, global warming has increased alarmingly which accelerated the use of sustainable materials and limit the use of carbon resources. At the same time, the cost of petroleum has increased significantly which has risen interest globally to use green and renewable resources as the basis of consumer products. This has influenced the production of polymers from renewable sources. Apart from this, there are lots of side effects of polymers that do not biodegrade or disintegrate easily into smaller fragments. For example, a lot of species are susceptible to entanglement by polymers and a study found more than 100 marine species that are vulnerable to such incidents [3]. Other studies found that polymer-based packing loops are a threat to sea lions and fur seals in

California and Australia [4,5]. These polymer-based materials can mimic natural food sources in our environment and severe side effects can be seen due to ingestion of polymers. It was found that ingesting polymer-based particles could cause intestinal blockage in fish, lower steroid hormone levels, and cause ovulation delay that may result in reproductive failure, etc. [6]. The ingestion of such particles by different species may potentially pass these particles up the food chain which has already been reported in a previous study where such polymer particles were recovered from fur seal scats [7]. Also, petroleum-based polymer such as acrylic polymer, which has found widespread use, is difficult to recycle and can produce harmful by-products during recycling if not properly done [8].

1.1.2. Classification of biopolymers

Biopolymers that are found in living organisms act as a structural component of tissue. These include mainly protein and polysaccharides. The most commonly known polysaccharides are cellulose, hemicellulose, and starch and proteins are collagen, soy, and silk[9]. Bacteria and fungi-derived biodegradable polyesters such as polylactic acid (PLA), polyglycolide (PGA), etc. are considered biopolymers. These types of polymers are commonly used for drug delivery and short-term implants [10,11]. Figure 1 shows an overall classification of biopolymers that includes synthetic biopolymers derived from natural sources.
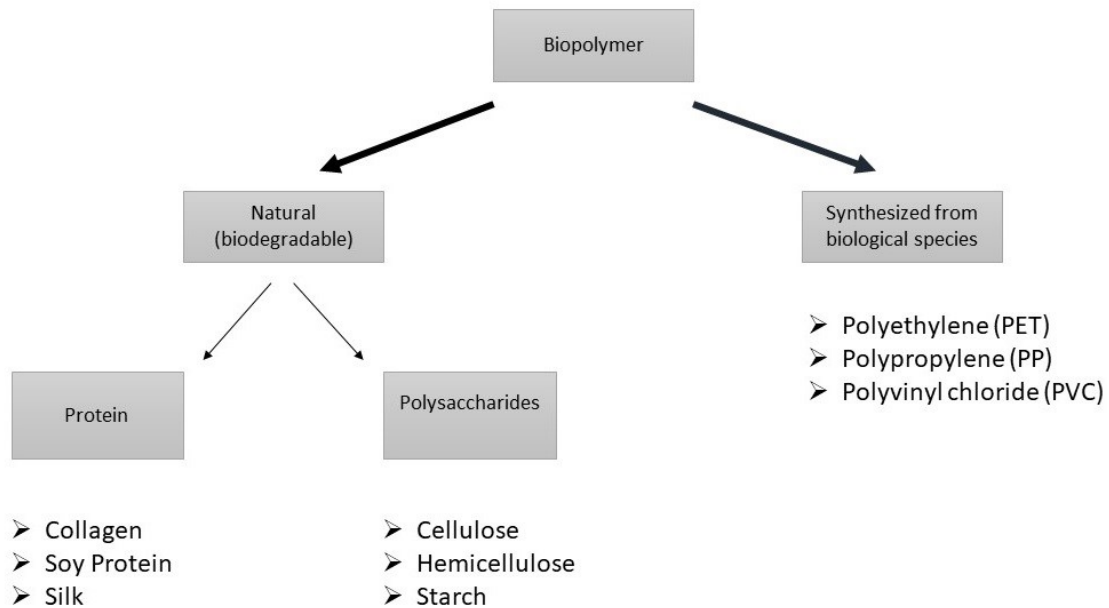
Figure 1. Classification of biopolymers [12].

1.2. The development of biopolymers

Biomaterials can be derived from bio-based materials or can be chemically synthesized from biological starting materials. Microorganisms, plants, and animals act as sources from which polymers can be derived directly whereas sugar and starch can be chemically modified to derive polymers.

Biopolymers derived from first-generation feedstocks such as sugar, starch, plant oil, etc. are most popular. Ethanol is produced by fermentation of sugars derived from sugarcane and beets or by the hydrolysis of starch derived from corn. This ethanol is then used as raw material to produce a variety of biopolymers. Though there has been an increasing concern over these types of biopolymers as they are in direct competition with food and animal feed production. These biopolymers are claimed to have similar side effects associated with biofuels e.g.

increased food cost and deforestation. This has led the industry to seek alternative feedstocks that do not compete with the food market and currently two categories of feedstocks are dominating research which are second-generation feedstock and alternative sources (shown in Table 1)

Food waste products and lignocellulose are considered second-generation feedstocks. Non-edible waste cooking oil or gat and waste potato skins can be considered as food waste that can be utilized. Short-rotation coppice such as willow and poplar, and corn straw, wood, etc. act as feedstocks for lignocellulose. The main components of this material are cellulose, hemicellulose, and lignin. Various sugars are produced by the hydrolysis of cellulose and hemicellulose by either an acidic or enzymatic route. These sugars are later fermented in the presence of various microorganisms. Unfortunately, second-generation biomass does not provide a higher yield than sugarcane and most second-generation biorefinery plants based on cellulose are still a few years away from commercial production. Lignocellulose materials can be transformed into synthesis gas (a mixture of CO and H_2) by gasification. This process can practically transfer all the carbon content of any form to carbon monoxide. This synthesis gas can be used to produce methanol which in turn is used to produce propylene. But due to the high cost of the process as a whole, there is still no commercial unit in operation for the production of synthesis gas from biomass.

Table 1. Feedstocks for producing biopolymers [13].

First-generation (edible and non-edible biomass)			Second-generation (non-edible biomass)			Other sources
Starch-rich plants	Sugar-rich plants	Oily plants	Lignocellulose (short rotation coppice)	Lignocellulose by-products	Willow	Natural rubber
Corn	Sugarcane	Sunflower seeds	Forestry waste (e.g. wood chips)	Waste vegetable oil (e.g. cooking oil)	Switchgrass	Microalgae
Potato	Sugar beet	Soybean seeds	Poplar	Animal fat (lard tallow, waste grease)	Potato skins	Greenhouse gas (CO_2)
Rice	Castor seeds	Grain	Paper waste			

1.3. Wood-derived biopolymer

One of the most abundant sources of a biopolymer is wood with a production capacity of approximately 3,900 million cubic meters per year [14]. Wood has been an integral part of modern society and has always contributed to the development of mankind. The role of wood will only grow as it will play a critical role to capture carbon and a fundamental feedstock for bio-based fuels. Wood mainly consists of cellulose, hemicellulose, and lignin as shown in Figure 2. Wood is typically classified into two groups: softwood and hardwood. Sugar-based polymers (cellulose and hemicellulose, 65-75%) and lignin (18-35%) are the major biopolymers of wood cell walls [15]. Considering the dry-weight, wood typically has 49% carbon, 44% oxygen, and 6% hydrogen [16]. The amount of biopolymers varies between softwood and hardwood as well as amount species. In general softwood contains a comparable cellulose content (40-44%), higher lignin (26-34%) and relatively low hemicellulose (20-32%) contents compared to hardwood which contains 40-44% cellulose, 23-30% lignin and 15-35% hemicellulose [15,16].
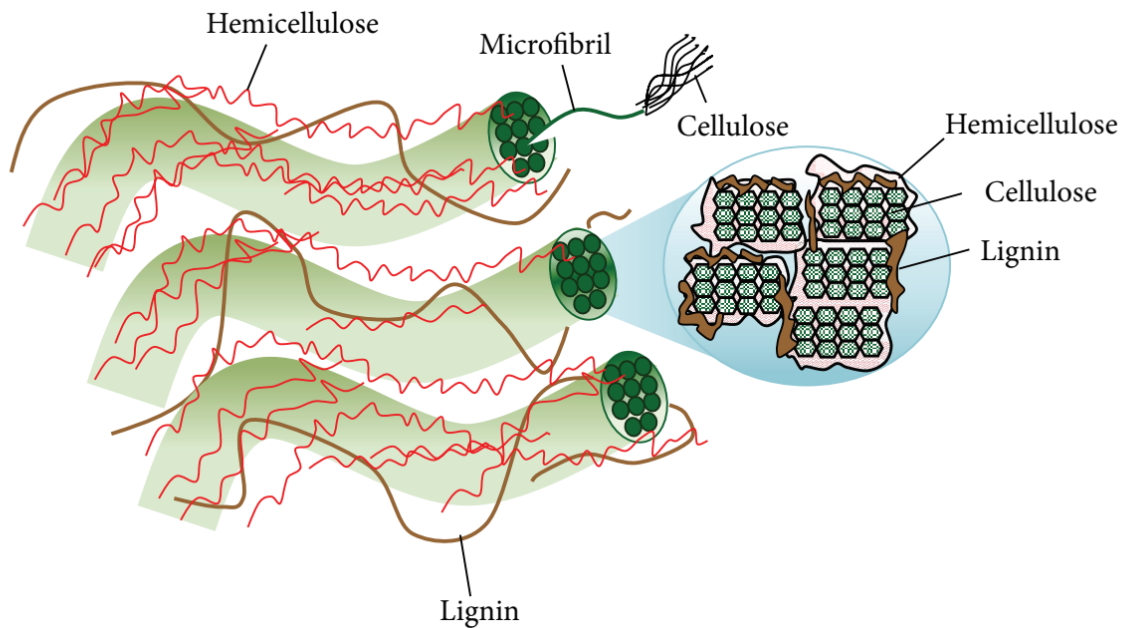
Figure 2. Plant cell wall structure [17]. This Open Access Article is licensed under a Creative Commons Attribution 3.0 Unported Licence.

There are various treatments to break lignocellulose biomass into cellulose, hemicellulose, and lignin such as acid hydrolysis, alkaline hydrolysis, oxidation agent, etc. but the most frequently used treatment is acid hydrolysis. During acid hydrolysis, hydronium ions break down and attack intermolecular and intramolecular bonds among cellulose, hemicellulose, and lignin. Different types of acids such as H_2SO_4, HCl, H_3PO_4, and HNO_3 are being used to hydrolyze lignocellulose [18,19]. These are effective agents for lignocellulose deconstruction and maximize the yield of monomeric sugars for biofuel production. Due to the toxicity and corrosive nature of these concentrated acids, extreme care is necessary to handle the process. Also, it is necessary to recover concentrated acids after the treatment to make the process economically and environmentally feasible. To maximize the yield of cellulose and lignin, it is imperative to properly optimize the type of acid, pH, reaction temperature, and reaction time.

For all these reasons, isolation of cellulose, hemicellulose, and lignin becomes cost-effective by using the diluted acid hydrolysis technique. Diluted acid such as low concentration H_2SO_4 < 4 wt.% [20,21] can be used to recover most of the hemicellulose as dissolved sugar at low temperature. After hemicellulose solubilization, the remaining fraction of lignin is removed from residue cellulose by the cellulose purification process. In the cellulose purification process, alkaline pre-treatment is utilized to separate lignin from cellulose. In the following subsections, we will discuss the properties of cellulose and lignin and their applications.

1.3.1. Cellulose

Cellulose, the principal component of the wood cell, makes up about half the biomass of photosynthetic organisms which makes it the most abundant molecule on earth. This cellulose along with components like hemicellulose and lignin makes up the cell wall that distinguishes animal and plant cells. The human body can't digest cellulose but some animals like ruminants can digest cellulose. A French chemist, Anselme Payen, was the first who identified the molecules and named them cellulose back in 1838. Willstatter and Zechmeister [22] were the first to propose the fundamental formula of the cellulose structure and later modified by Irvine and Hirst [23] saying cellulose is macromolecular which is the presently accepted concept. The primary structure of cellulose had been identified linear homopolymer of glucose residues with D configuration linked by β-(1 → 4) glycosidic linkages [24] as shown in Figure 3. On the glucan chain, cellulose forms intramolecular and intermolecular hydrogen bonding by hydroxyl groups that stiffen the chain and promote cellulose aggregations. Cellulose and protein mixture provide rigidity to plant cell wall and also allow cell growth and extension [25]. Cellulose has been excessively used in nanofibrils form by mechanical grinding or high-

pressure fluidization to remove the lignin content. These fibrils have a high aspect ratio with a diameter between 5-20 nm and length in the μm region. It forms a gel-like material when the concentration is low and can be used to produce biodegradable and environmentally safe films for various applications. Cellulose and plasticizers can be mixed to improve their physical properties such as grease proof-ness and high barrier against oxygen transmission at dry conditions and makes it suitable for commercial applications. It is the major constituent of paper and paperboard and can be converted into biofuel by a bacterium found is zebra waste. These celluloses are used to make water soluble adhesives and binders to be used in wallpaper paste and also a major component to produce hydrophilic and highly absorbent sponges.
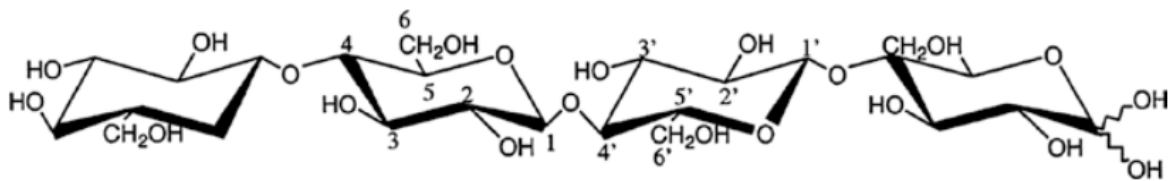
Figure 3. Molecular structure of cellulose. Reprinted with permission from [26,27]. Copyright Springer Nature, license number: 4996710032761.

1.3.2.   *Lignin*

Lignin is the most abundant aromatic polymer (Figure 4) in nature and the next more abundant polymer after cellulose. The word lignin comes from the Latin word lignum which means wood. It plays a similarly important role in plant structures like cellulose. Lignin is a heteropolymer and its structure is complex. These hydrophobic polymers provide strength and rigidity by acting as a matrix that binds the cellulose, hemicellulose, and other components of the cell and also responsible for the upright growth of the wood [28]. Around the cellulose

microfibrils, there are spaces, and lignin is formed within those spaces in woods, thus forming a lignocellulose matrix that provides strength to the plant [24]. Apart from the structure role, lignin also plays a significant role for the transport of water and nutrient within the plant and prevent degradation by preventing the penetration of destruction enzymes [29]. To date, the exact structure of lignin is unknown due to its complex structure and to the fact that it varies with source and extraction method though it is known that it contains methoxyl, phenolic hydroxyl, and a few thermal aldehyde groups. There are many commercial applications of lignin e.g. i) it is mixed with concrete to reduce the damage caused by moisture and acid rain, ii) it provides thermal protection to polypropylene and rubber, iii) it is used to increase the water solubility of asphalt, iv) it is used to fabricate carbon nanotubes, v) it is mixed with asphalt and water to control dust of a road surface upon spraying, vi) it is mixed with grease to improve corrosion protection properties, vii) it can be used as a dispersant for cleaning and/or laundry detergent compounds, viii) chemically modified lignin is used as a binder, dispersant agent in pesticide, ix) it is used for automotive brakes and epoxy resins for printed circuit boards etc.
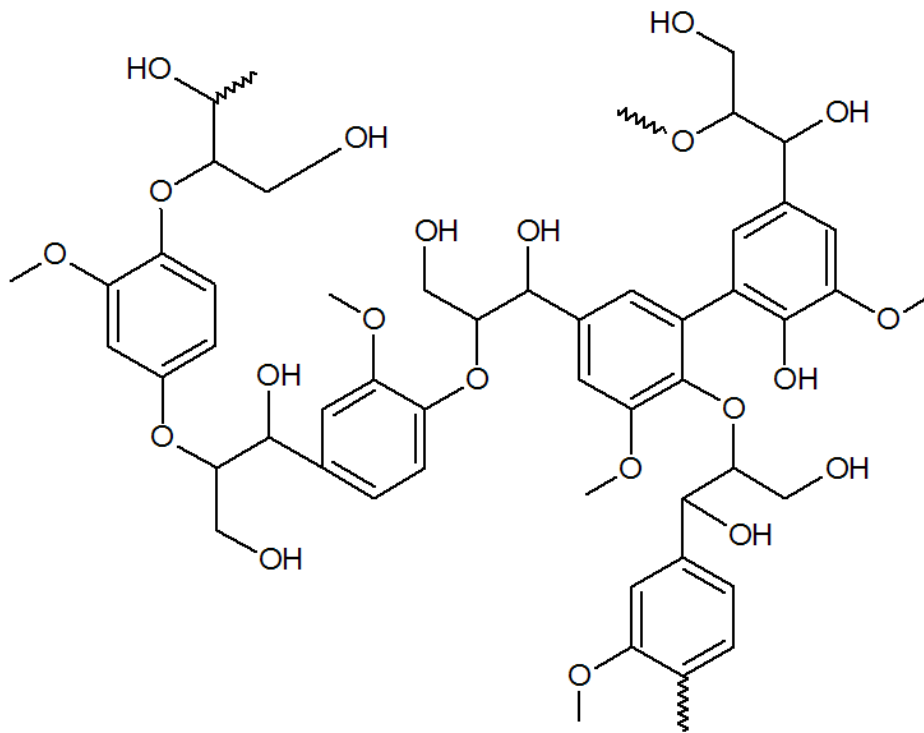
Figure 4. Molecular structure of lignin [30]. Copyright © 2021 polymerdatabase.com.

1.4. Thesis objectives

As described in earlier sections, the use of petroleum-based products is impacting the environment negatively since it takes a long time to degrade, harm the normal life cycles of many animals, and most importantly the adverse effect of petroleum has a strong influence on global warming. Plant-based biopolymers can play a pivotal role in addressing environmental issues by replacing petroleum-based products since they are easily degradable, sustainable, and abundantly available. Currently, a good number of petroleum-based polymers are available in the market and have found broad applications in photonics, and replacing petroleum-based polymers with plant-based biopolymers in some of these applications is highly desired.
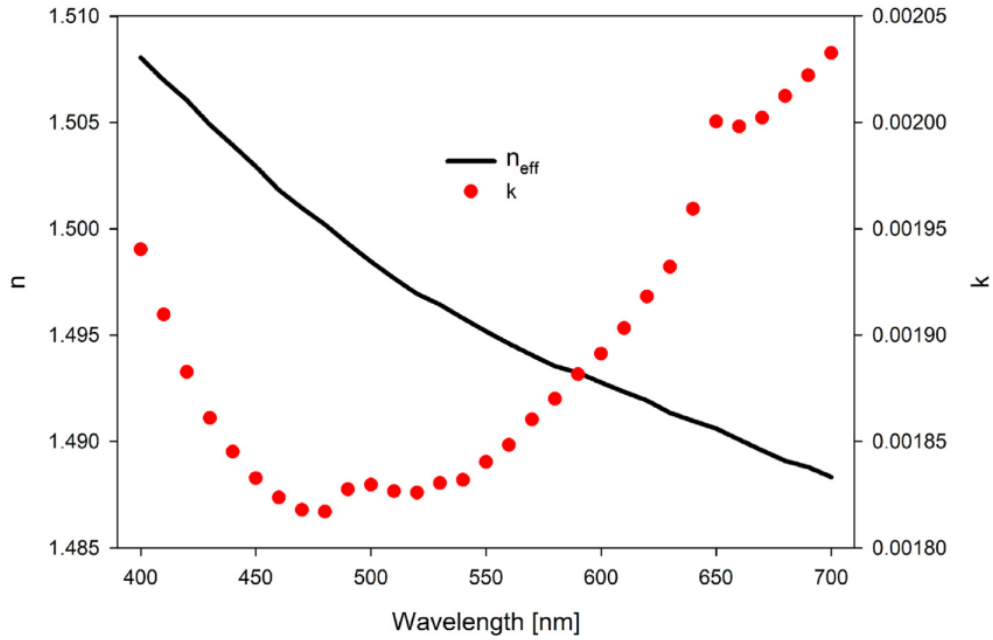
Figure 5. The Complex effective refractive index of cellulose nanocrystals as a function of wavelength [31]. Copyright Elsevier, license number: 5026600292033.
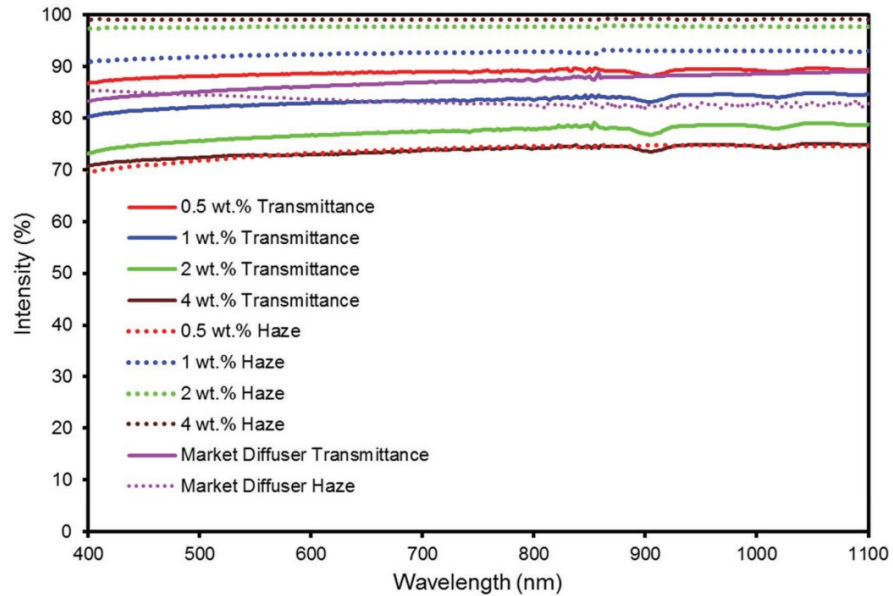
Figure 6. Transmittance and haze of CNP hybrid optical diffusers with different concentrations [32]. Copyright John Wiley and Sons, license number: 5026600474652.
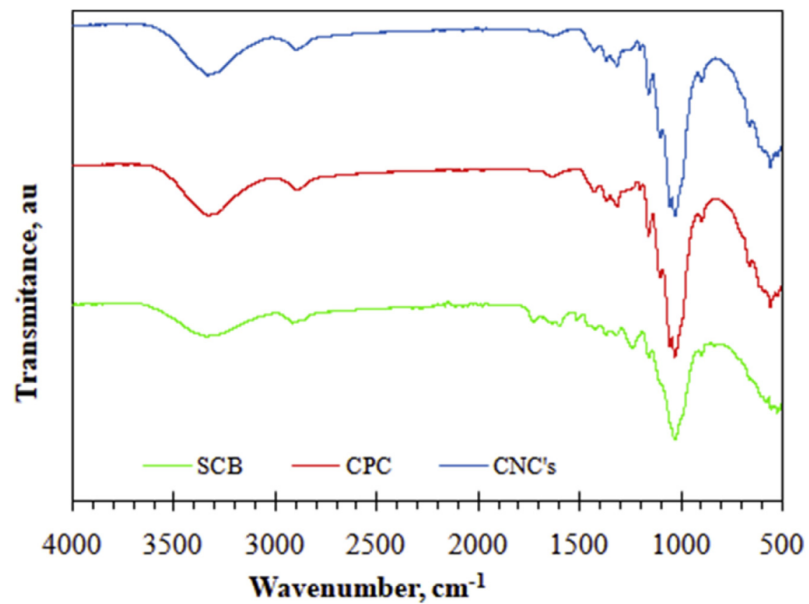
(a)
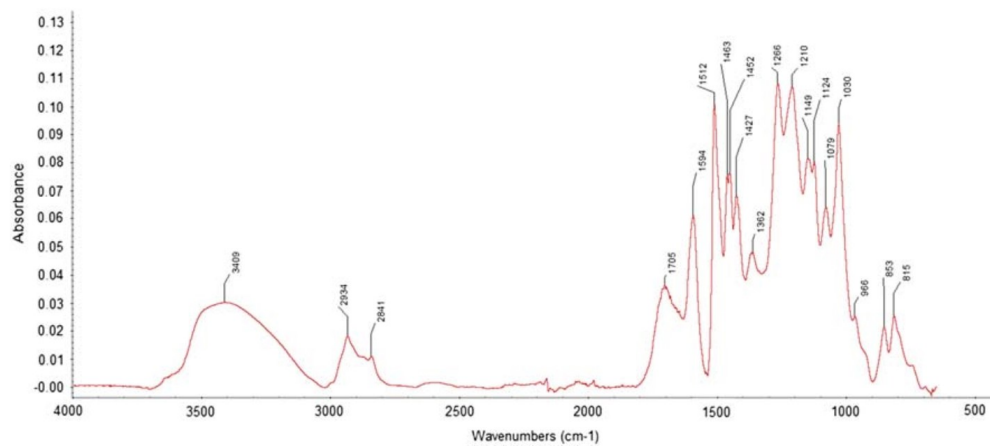
(b)

Figure 7. FTIR spectra of (a) CNCs [33], this Open Access Article is licensed under a Creative Commons Attribution 4.0 Unported Licence and (b) softwood kraft lignin derived from ponderosa pine [34], copyright Elsevier, license number: 5026600147137.

Wood-derived biopolymers like cellulose nanocrystal and lignin have some interesting optical properties. They are transparent or can be made transparent potentially in the visible spectrum. They also have strong absorption/emission in the "sky window" (between 8-13 μm wavelength). Furthermore, cellulose nanocrystals show strong scattering in the visible spectrum. Figure 5 and Figure 6 show complex refractive index and transmission property of cellulose nanocrystals. These data show that cellulose nanocrystal has a suitable refractive index, high transparency, and tuning its concentration could yield high scattering. On the other hand, Figure 7 shows the FTIR spectra of cellulose and lignin that shows that both these polymers have high absorption between 600-1200 cm^{-1} (8.3-16.7 μm). Therefore, wood-derived biopolymers may potentially replace petroleum-based polymers in some photonic applications for the above-mentioned optical properties.

In this thesis, the main objective is to show the prospect of cellulose nanocrystals and lignin in replacing petroleum-based polymers in various photonic applications such as luminescent solar concentrators, radiative cooling, photovoltaic devices, and light-emitting diodes by leveraging their optical properties. To accomplish this objective, different structures are developed by taking advantage of theories, simulation (where it fits), and experimental design. Preference is given to investigate the structures that are simple, cost-effective, and can be introduced without changing the current process steps which will increase the potential for commercialization.

1.5. Outline of the thesis

In chapter 2, the application of wood-derived cellulose nanocrystals as waveguide material for luminescent solar concentration is demonstrated. Generally, poly(methyl methacrylate), otherwise known as PMMA or acrylic polymer emulsion (APE), is used as a waveguide for

such application but due to its chemical composition, degradation of this material is problematic. Here we thoroughly investigate the feasibility of cellulose nanocrystals to be used as waveguide material and provide necessary recommendations for practical implementation.

In chapters 3 and 4, lignin-upgraded and cellulose-upgraded polymers for radiative cooling have been proposed, respectively. Passive radiative cooling can be an exciting prospect to reduce energy usage and lower carbon footprints. Different structures based on lignin and cellulose nanocrystals have been studied focusing on their application during the daytime. Leveraging the inherent property and innovative designs, radiative cooling temperature 3.7-3.97 °C are achieved for these materials with significant cooling power. While lignin provides adequate cooling power, its high solar absorption requires an additional modification to make it suitable for daytime application. For that reason, this study is extended to investigate cellulose since it has low solar absorption and can be a good prospect for practical implementation. Furthermore, as proof of concept, both radiative coolers are utilized to lower the operating temperature of solar cells.

In chapter 5, cellulose nanocrystals embedded structure has been investigated to improve the light quality of white light-emitting diodes (LEDs). The most common and easiest way to fabricate a white LED is by using phosphor with a blue LED chip. Cellulose nanocrystals can scatter light that could enhance blue light absorption and yellow light emission by the phosphor and improve overall light quality. In this chapter, this scattering property of cellulose nanocrystals has been thoroughly investigated to improve the correlated color temperature and luminous flux of white LEDs.

In chapter 6, a summary of the key findings of this thesis is presented alongside a brief description of some suggested future works that can further boost efforts to replace petroleum-based products with biopolymers.

Chapter 2: Cellulose nanocrystals for luminescent solar concentrator

2.1. Introduction

Harvesting solar energy efficiently via cost-effective approaches is critical for large-scale adoption of solar energy as an energy resource in human society. Concentrating solar radiation has a great potential to increase solar energy conversion efficiency and researchers started to begin to find inexpensive ways to concentrate light. Studies had begun as early as 1949 to trap fluorescence inside a body by total internal reflection (TIR) and experimentation begun on luminescent solar concentrators (LSCs) in the late 1970s [35]. During that time, the TIR effect was studied in terms of implementing solar components to reduce PV surface and minimize the associated cost [36,37]. Table 2 shows the history of LSCs since their discovery.

Table 2. History of LSCs [38].

Year	
1949–1970	Invention
1970–1980	First experiments and publication
1980–1990	Limitations of fluorescent organic dyes hindered further development
1990–2000	Application of new luminescent materials semiconductor quantum dots (QDs)
2000–2010	Discovering materials such as photonic layers, liquid crystals have also been utilized to reduce losses within the devices
2010–2015	New material and developments in ray-trace, thermodynamic modeling software

Because of the performance of the luminescent dyes, LSCs development was limited initially but because of the realization of lack of fossil fuels and unstable price, meaningful enhancement was made during the last decade.

2.2. Working principle of luminescent solar concentrator

In LSCs, light is absorbed by luminescent molecules e.g. organic dyes, quantum dots, and then re-emitted at longer wavelengths. A portion of this re-emitted light gets trapped in the waveguide by TIR and becomes concentrated along the plate edges. PV cells are attached along the perimeter of the waveguides which convert this re-emitted light into electricity [35]. Figure 8 illustrates a LSCs where the incident sunlight is absorbed by the organic dyes which emit fluorescence that gets transported to the edge by TIR. Photovoltaic cells are installed along the perimeter of the waveguide which can absorb the fluorescence and convert it to electricity. As the surface area of the slab is much larger than the area of its edges, there will be an increase in photon concentration ratio, which is the ratio of photon flux escaping from the edge to the photon flux incident on the top of the surface [36],[39]. If the slab design is optimized (high ratio of top surface area over side edge area), there will be a high concentration of flux coming out of the edges which might boost the open-circuit voltage of the solar cell, similar to concentrated photovoltaics (CPV). Therefore, the idealized LSC would produce more efficiency compared to the cell exposed to AM1.5G [39].

Several loss mechanisms reduce the amount of fluorescence reaching the solar cells as pictured in Figure 9. Some of the incoming light will be reflected by the waveguide and some light will just pass through the waveguide without getting absorbed by luminescent molecules. Some light will just be refracted out of the waveguide rather instead of reflecting internally. Some

luminescent molecules have overlapping absorption and emission spectra which causes the reabsorption of emitted photons and reduce the amount of light reaching the edge of the waveguide. Luminescent molecules have a quantum yield of less than 1 which would further reduce the light reaching the solar cells on the sides. Some waveguides may have parasitic absorption of near-infrared light and can also have bulk imperfection which would scatter the light out the waveguide, further reducing the efficiency.
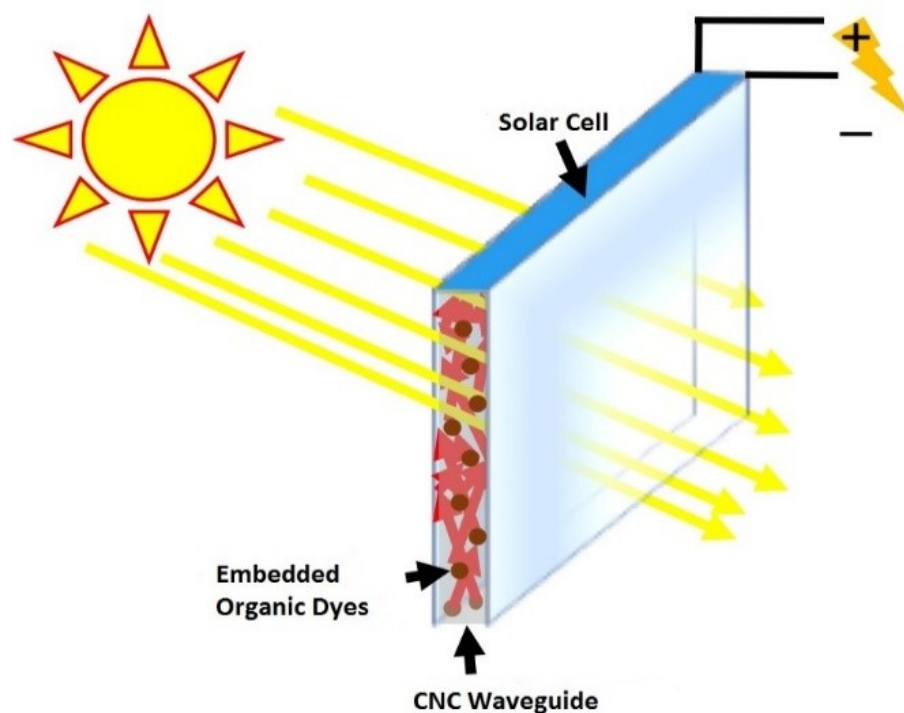
Figure 8. Schematic representation of fluorescence material-based LSC where the solar cell installed at the edge can absorb fluorescence to produce electricity.

Many types of luminescent fluorophores have been studied for LSC application such as organic dyes, inorganic phosphors [40–44], quantum dots (QDs) [45–51], etc. Recently different designs for LSC have also been tried such as variation in device geometry [52], multiple dyes

based LSC [53,54], multiple layers based LSC [55], use of metal to enhance photoluminescence [56], etc. The main motivation to go towards LSC is to replace those costly solar cells required in flat photovoltaic (PV) panels, with an inexpensive luminescent collector which would reduce the cost of solar power. A key advantage this LSC technology has over other concentration systems is that it can successfully convert both direct and diffused light into electricity. This will reduce the cost further as no sun tracking is required and will make it an excellent candidate for building-integrated photovoltaics (BIPV) and regions with cloudier climates [42].
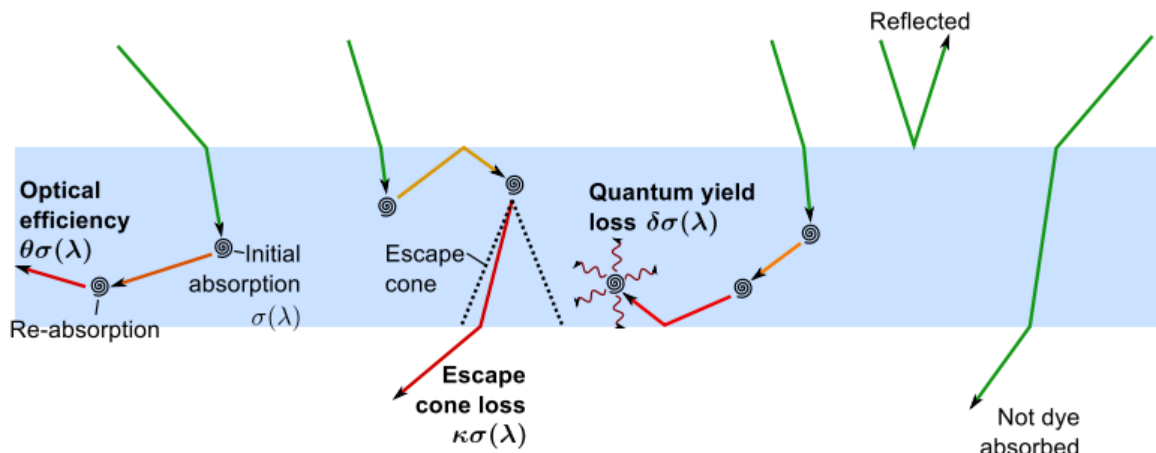
Figure 9. Loss mechanism in LSCs [57]. This Open Access Article is licensed under a Creative Commons Attribution 3.0 Unported Licence.

Apart from studies on improving the efficiency of LSCs, identifying the optimum host material for the overall LSC system is also important. The material used as matrix material that would contain the dyes/QDs can have a significant effect on the LQY and stability of the dyes/QDs. The host matrix should have maximum transparency over a broad wavelength range with minimal scattering. Though acrylic polymer emulsion (APE) is one of the most commonly

used matrix materials, other materials have also been investigated as a host matrix for improved stability of dyes [58–60]. Nature-based nanomaterials, which offer ecological advantages, are also attracting a lot of interest for such applications [61,62]. As mentioned earlier, cellulose is a widely found biopolymer that has been used as energy resources, building material, and a component of clothing for a long time. Different techniques and sources are present to produce this nanocellulose which are summarized in earlier reviews that focus on the production, chemistry, and application of cellulose nanocrystals (CNCs) [63–68]. Mass production of these CNCs is also possible at a low cost using the acid hydrolysis method. CNC has already been approved for unrestricted use in Canada and was the first nanomaterials to be included in Canada's Domestic Substances List (DSL) [69].

In this chapter, we investigate the suitability of CNCs material as a host matrix for LSC application. The performance of CNC material is compared with APE material, which is used most commonly as host matrix in LSC. Moreover, we have studied the possibility of recyclability of CNC material which will help to reduce the material requirement and cost during the large-scale implementation of this material for LSC application.

2.3. Experiment

2.3.1. Materials

Cellulose nanocrystals (CNCs) were mass-produced in the CNC pilot plant at Alberta Innovates Technology Futures (AITF, Edmonton, Alberta, Canada). APE was purchased from Golden Artist Colors Inc. [70]. Glycerol, Methanol, and glass samples were purchased from Fisher Scientific. Rhodamine 6G which was used as the luminescent dye was purchased from Sigma-Aldrich.

2.3.2. Organic dye solution

0.1 g of Rhodamine 6G was mixed with 10 mL of methanol solution in a test tube. To dilute, 1 mL of this solution is taken from the test tube and mixed with 9 mL of methanol in another test tube which acted as our reference dye solution.

2.3.3. CNC synthesis

The acid hydrolysis process was used to synthesis CNC. Sulfuric acid hydrolysis with an acid concentration of 64% at 45°C was performed at first using two Pfaudler 50-gallon (189 liters) acid-resistant glass-lined reactors with a steam-heated jacket. Later on, a centrifuge step was performed using a GEA Westfalia SC-35 Separator. The last stage involved drying of CNC powder in an SPX-Anhydro Model 400 Spray Dryer Plant at the conditions of a 220°C inlet temperature and an 85°C outlet temperature.

2.3.4. CNC and APE films deposition

CNC films with organic dyes were prepared by the following steps. First, 2 g of CNC powder and 40 mL of deionized (DI) water were mixed to form a CNC solution. 0.8 mL glycerol was later added to this solution to avoid crack formation in the films during drying. Three different samples were fabricated where with the above solution 1 mL, 0.5 mL, and 0.25 mL reference dye solutions were added and named as 20x CNC, 5x CNC, and 1x CNC respectively. After that, the solutions were stirred at 75 °C for 90 mins. Finally, these mixtures were poured into plastic Petri dishes where we already placed our glass samples and let the solution dry for 72 hours. After that, glass samples with CNC films were taken out of Petri dishes. For comparison

APE samples with similar dye concentrations were fabricated. This APE, which was purchased from Golden Artist Colors, Inc, [70] was in gel form and soluble in water. 5 mL of APE and 40 mL deionized water were initially mixed to form an APE solution. After that 1 mL, 0.5 mL, and 0.25 mL reference dye solutions were added with the above solution and named 20x APE, 5x APE, and 1x APE, respectively. Later these solutions were stirred at 75°C for 90 mins. In the end, these mixtures were poured into plastic Petri dishes with glass samples already placed inside and dried for 72 hours at room temperature. After that, glass samples with APE films were taken out of Petri dishes. The thicknesses of all the CNC and APE samples were measured and found to be similar. Average thicknesses of CNC film and APE film deposited on glass were 0.327±10% mm and 0.307±10% mm, respectively. Dye concentrations of 20x, 5x, and 1x samples (both CNC and APE) were found to be 2.09 μM, 0.52 μM, and 0.104 μM respectively. The process flow of the fabrication is shown in Figure 10 (a) and a fabricated sample is shown in Figure 10 (b) [71].
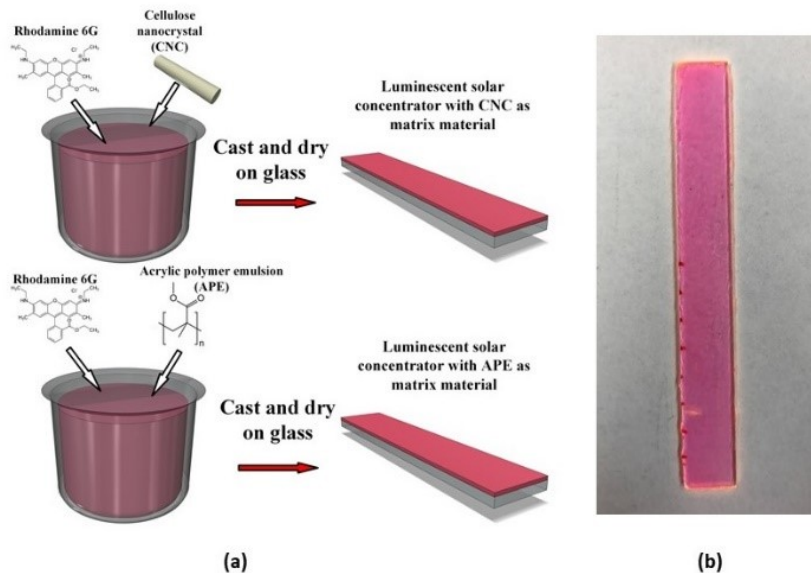
Figure 10. (a) Process flow of the fabrication (b) Top view of a fabricated sample.

2.4. Results and discussion

Photoluminescence (PL) spectra of the samples were measured at room temperature and at an excitation wavelength of 520 nm (Sciencetech Inc.) with an integrating sphere and a modular spectrometer (Ocean optics) and absorption spectra were measured using Perkin Elmer Lamda 1050 UV-Vis–NIR Spectrophotometer. Figure 11 is showing a schematic of the characterization setup which was used to measure the photoluminescence of the samples.
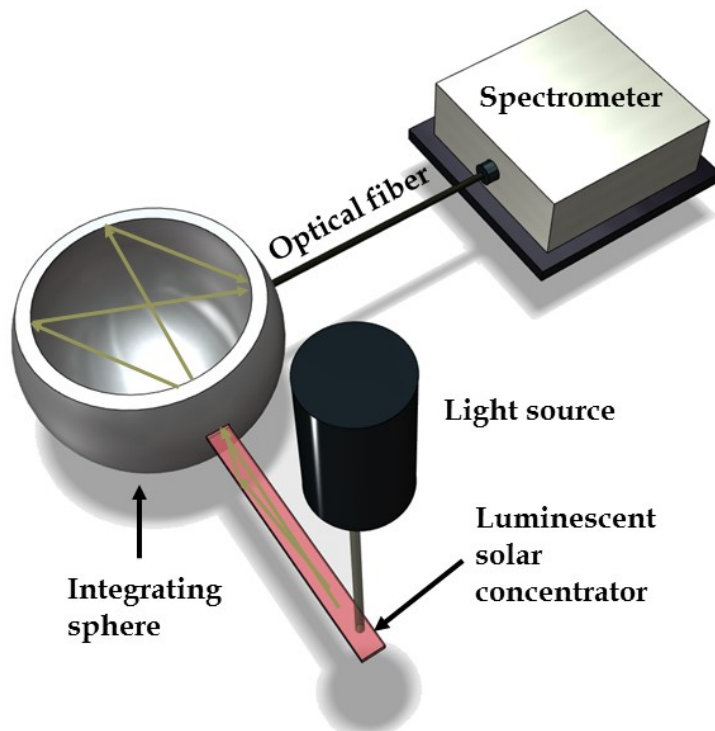
Figure 11. Schematic of the characterization setup for photoluminescence measurement.

Figure 12 and Figure 13 show the absorption and emission spectra of CNC and APE samples at three different dye concentrations. These figures show that 20x CNC and 20x APE samples have the highest light absorption and emission and 1x CNC and 1x APE samples have the lowest, which is consistent with their dye concentrations. It is also visible that CNC samples have higher light absorption and light emission compared to APE samples for comparable concentrations. From these two figures, it is also visible that with increasing dye concentration, there is a relative drop in peak emission compared to peak absorption for both CNC and APE samples which is due to the reabsorption losses when more dyes are present in the matrix. These losses are also the reason for the slight red shift in emission peaks.
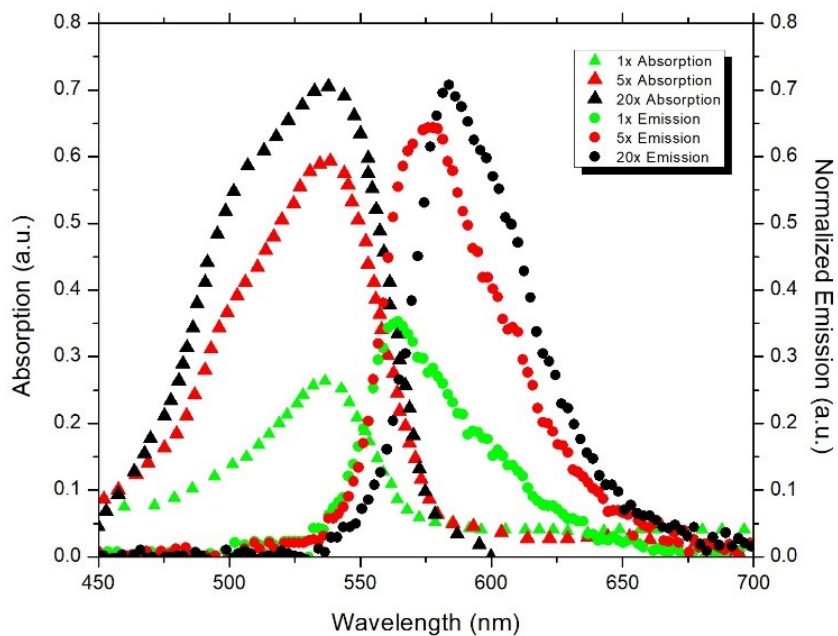
Figure 12. Absorption and Emission spectrum of CNC samples with various concentrations of dyes.
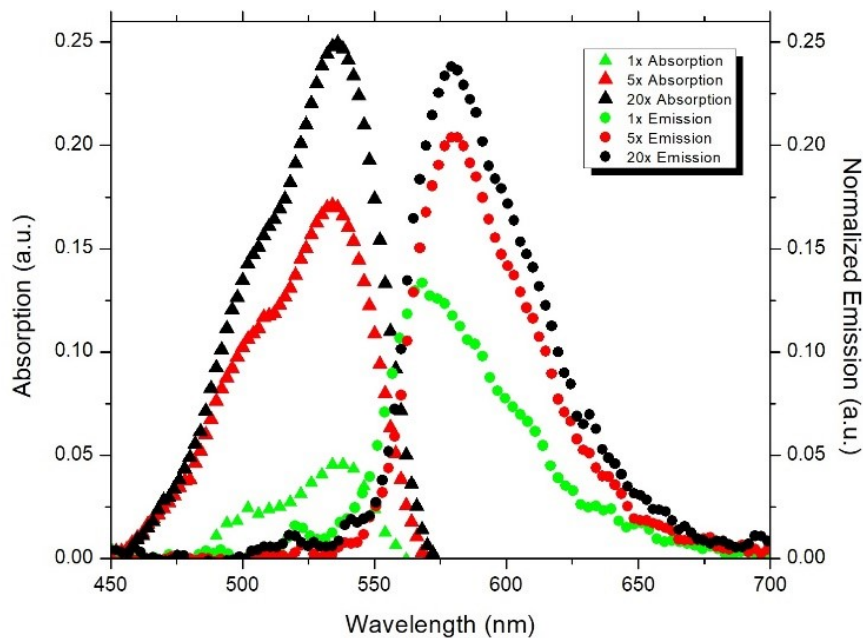
Figure 13. Absorption and Emission spectrum of APE samples with various concentrations of dyes.

In Figure 15, Figure 16, and Figure 17, optical efficiencies at different edge distances of CNC and APE samples have been compared. Here optical efficiency is defined as the ratio of collected photons at the edge to incident photons on the sample and, edge distance is the distance between the source incident point on the sample and edge from where emitted photons are being collected. In the experiment, we extracted the photons from only one edge of the sample and calculation shows that when the incoming beam hits the sample, only one-fourth of light gets the chance to escape through that side of the sample's edge. Hence the optical efficiency values at 0.5 cm were multiplied by 4 and to maintain consistency, the rest of the values were also multiplied by 4 which we deem as the maximum optical efficiency that can be achieved by extracting photons from four side edges of the sample.

These figures show that optical efficiencies at 0.5 cm for 1x APE, 5x APE, and 20x APE are 6.0%, 10.0%, and 10.7% respectively, suggesting a performance drop due to reabsorption of photons [72,73] by the dyes when dye concentration is increased. CNC samples also show a similar trend with 10.9%, 15.1%, and 21.0% optical efficiencies for 1x CNC, 5x CNC, and 20x CNC respectively.

These results also show that optical efficiencies of CNC samples are higher at shorter edge distances compared to APE samples. Transmission and reflection data of CNC and APE materials (see Figure 14) show that CNC material may absorb a small amount (less than 10%) of light while APE material is almost transparent. However, this small absorption (unity minus transmission and reflection) might come from the scattered light that is not captured in the measured set-up. We believe this characteristic of CNC material influence the overall absorption of the LSC providing higher absorption and emission. When the edge distance is increased, CNC samples experience a larger performance drop than APE samples. For 1x CNC,

5x CNC and 20x CNC, drops in optical efficiencies when edge distance is increased from 0.5 cm to 4 cm are 93.6%, 88.1% and 85.7% respectively whereas for 1x APE, 5x APE and 20x APE, these values are 48.3%, 43.0% and 26.2% respectively. These results indicate that CNC material as a host matrix has superior quality to APE material, which increases absorption and emission of light. But APE material, as a waveguide, supports light propagation better when the distance being traveled is increased compared to CNC material. The reason for this is that light scattering is prominent in CNC material which reduces its optical efficiency significantly when the edge distance is increased and further optimization during CNC synthesis is required to improve this.
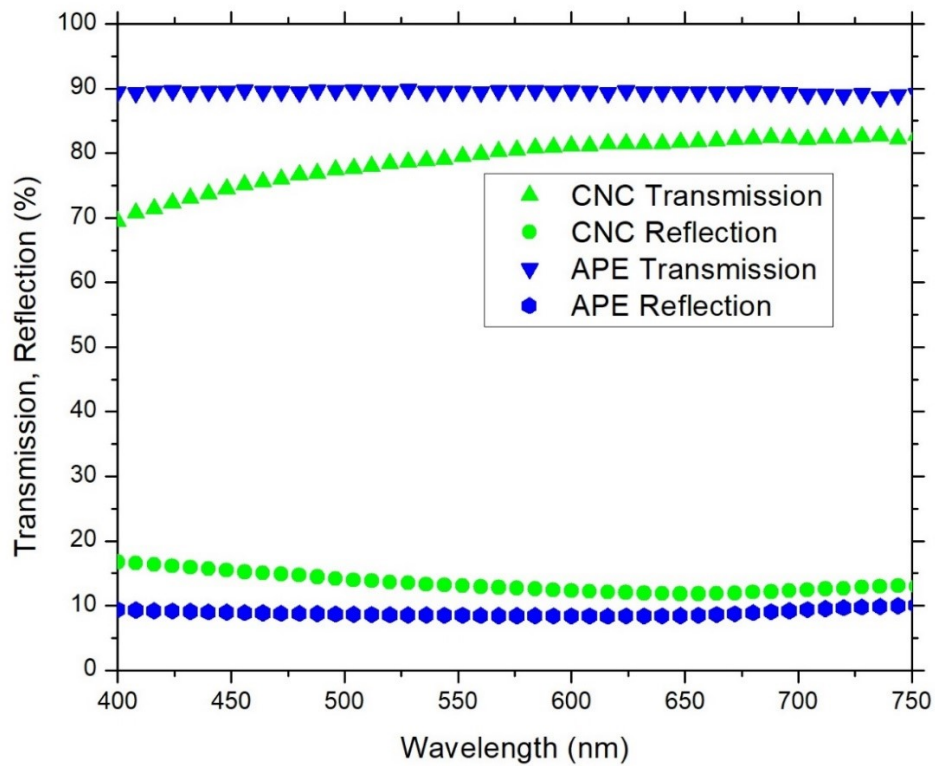
Figure 14. Transmission and reflection data of un-doped CNC and APE samples.
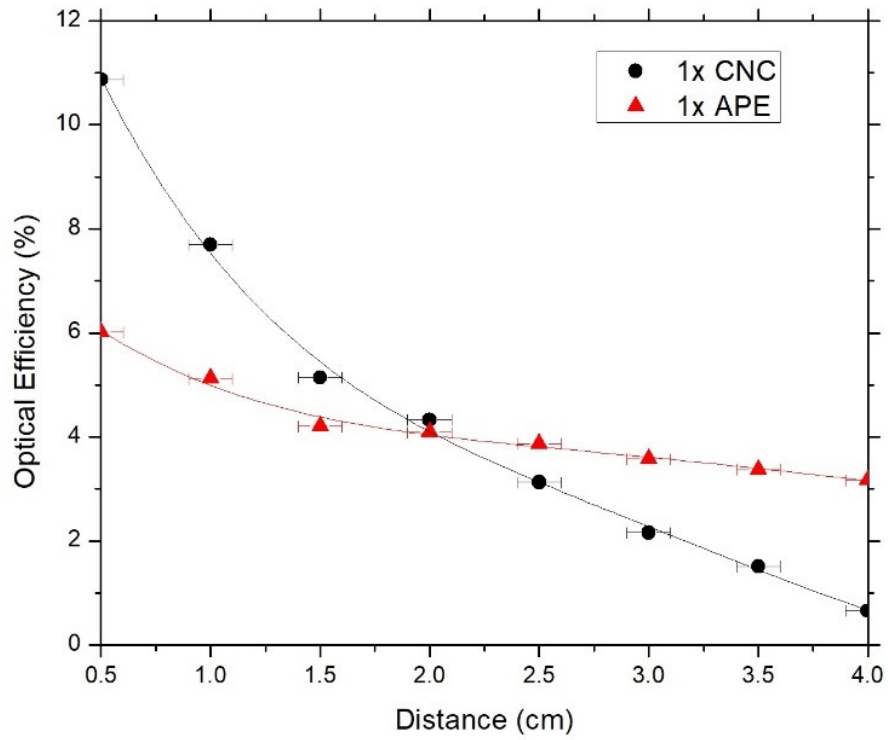
Figure 15. Optical efficiency (%) of 1x CNC and 1x APE samples.
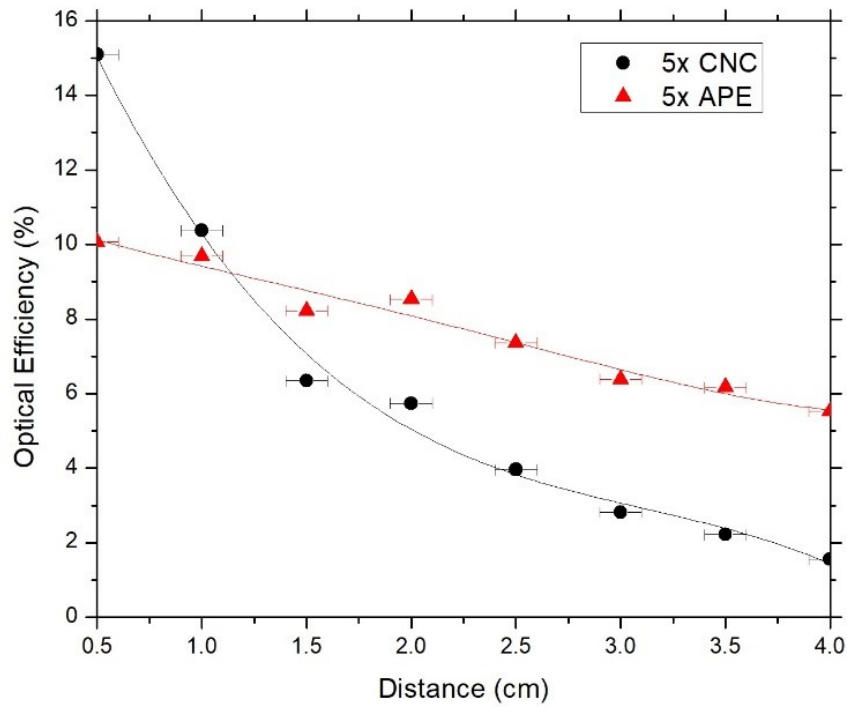
Figure 16. Optical efficiency (%) of 5x CNC and 5x APE samples.
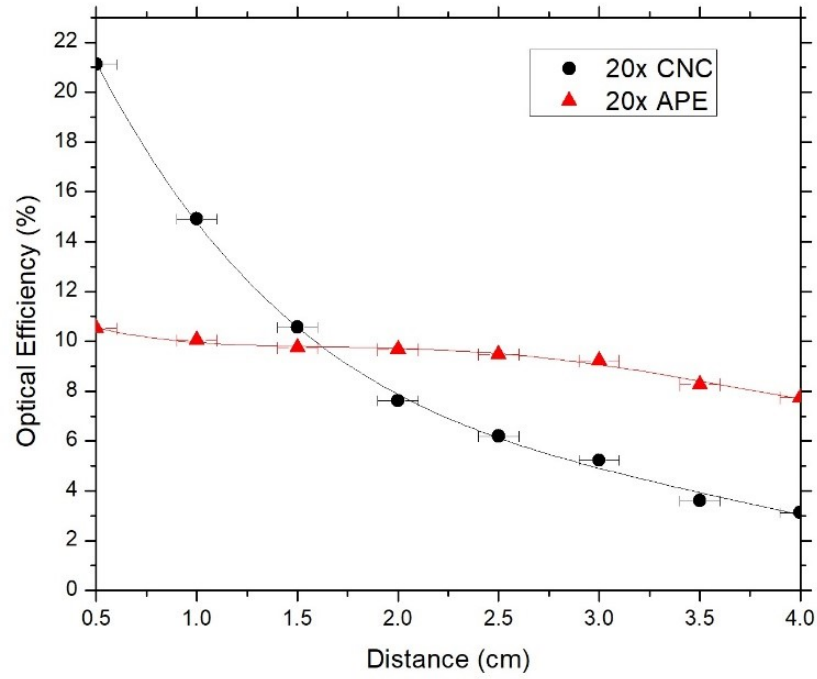
Figure 17. Optical efficiency (%) of 20x CNC and 20x APE samples.
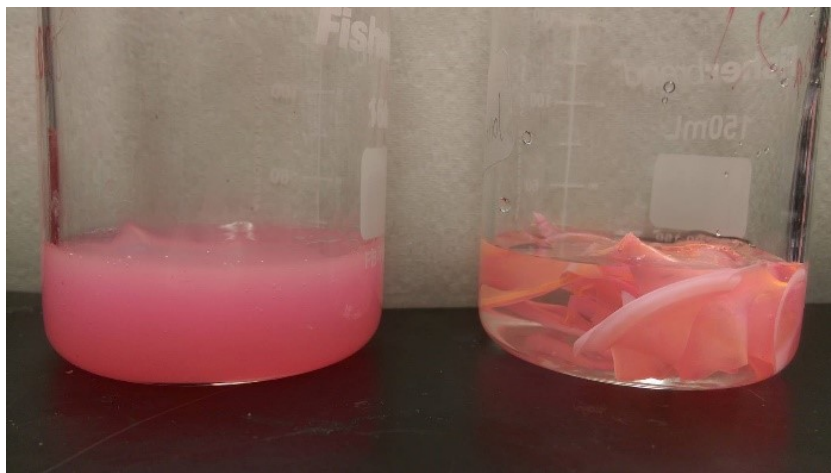
Figure 18. Solution of recycled CNC and APE samples.
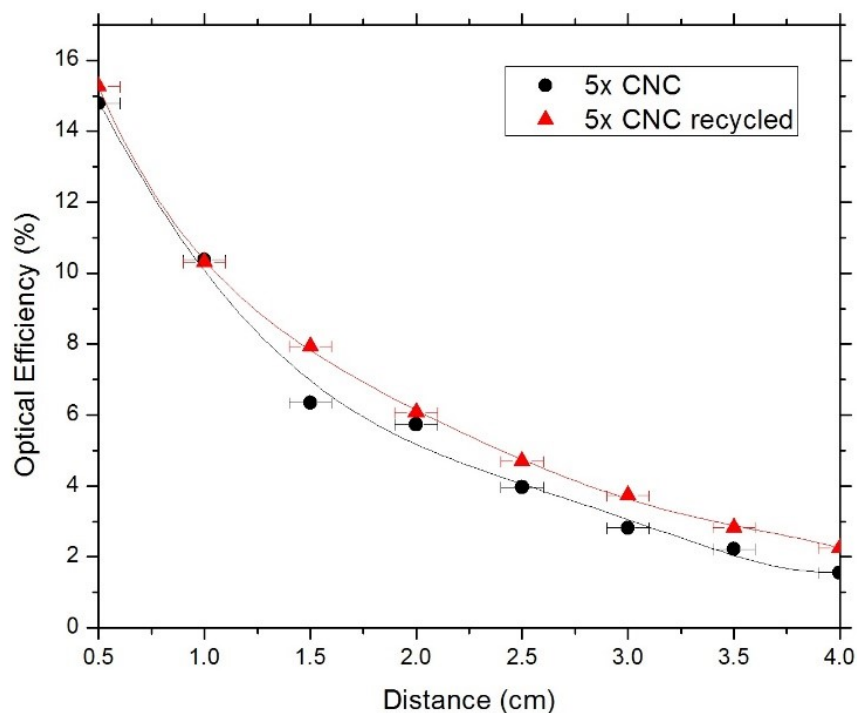
Figure 19. Optical efficiency (%) of a 5x CNC sample before and after the recycling process.

Next, we studied the recyclability of CNC and APE materials as host matrices. For this purpose, 5x CNC and 5x APE samples were taken into consideration. The host materials were stripped off the glass samples and from the Petri dishes and, were placed inside beakers. Adequate DI water was added, and the solutions were stirred at 75°C for 90 mins. It was found that solid CNC material reabsorbed water and formed a diluted solution, like the one formed initially. APE material, on the other hand, did not absorb any water and remained solid once the experiment is finished. Figure 18 shows the condition of CNC and APE materials after the stirring step, verifying the above statement. Later the recycled solution was used to fabricate a sample, named 5x CNC recycled, using the steps mentioned earlier and compared its performance with the previous result. Figure 19 is showing the optical efficiencies of 5x CNC and 5x CNC recycled samples. This figure shows that the quality of the sample does not drop

even after performing the recycling step. Though this feature of CNC material is exciting, it also opens the door to other challenges as well. For the large-scale implementation of such material and in an environment where rain and snow are regular encounters, such solubility of CNC in water can be tackled with a special coating layer that would not deteriorate the performance and at the same time will keep the LSC unaffected.

2.5. Conclusion

In this chapter, the CNC film as the host matrix and waveguide for LSC applications has been presented, and the CNC-based LSC has been compared to that is made of APE. Optical efficiencies of the CNC samples showed that with increasing distance, the values dropped between 85%-94% whereas, for APE samples, the drop is between 26%-48%, depending on dye concentrations. These decreases in optical efficiencies with increasing distance for both APE and CNC samples are mainly due to reabsorption losses, but CNC samples experience a larger performance drop which is due to the additional scattering of light taking place in CNC material. Also, with increasing concentration of dyes, the relative peak emission intensities are found to decrease for both CNC and APE samples which is also due to the reabsorption losses. At shorter edges distance, optical efficiencies of CNC samples were higher than APE samples which suggest that as a host matrix CNC material is better than APE material although further optimization of CNC material is required to make it effective as a waveguide. Moreover, APE material is not recyclable, but CNC material can be reused and the fabricated sample with recycled CNC material showed little or no loss in optical efficiency. Though further optimization is required during CNC film processing to reduce light scattering and increase its optical efficiency with increasing device area, biocompatibility, and recyclability of CNC

material makes it a promising candidate for large-scale implementation for LSC application at

a reduced cost.

Chapter 3: Lignin-upgraded polymer as radiative cooler

3.1. Introduction

There is an increase in demand worldwide for cooling and air conditioning due to an increase in population, global warming, and improvements in living standards in developing countries with hot climates [74]. There is a concern regarding the vapor-compressor-based cooling system, first due to the massive energy consumption by the system and second due to the refrigerants e.g., hydrofluorocarbons (HFCs) used in this system that causes global warming [75]. In addition to power these systems, non-renewable fossil resources are being used which makes the earth hotter [76]. This has led to a search for an alternative solution and passive radiative cooling is an exciting option as it can dissipate heat without consuming electricity [77–80]. The earth has a surface temperature of 300 K and the universe has a temperature of 2.7 K [81], which allows the universe to act as an ultimate heat sink. Because of this temperature difference, the earth's surface can cool down by emitting thermal infrared radiation through the atmosphere. Traditional cooling systems dump all the heat into the surroundings whereas by radiative cooling excessive heat is sent to outer space with no external energy which makes this technology appealing. Over mid-infrared wavelength between 8-13 μm, the Earth's atmosphere is remarkably transparent [82] to radiation and this wavelength range also coincides with the peak wavelength of thermal radiation from a structure at typical ambient temperature. Thus, a structure at ambient temperature can transfer energy to the universe.

A lot of work has been done on radiative cooling in the last few decades and practical implementations for nighttime cooling were demonstrated [79,82–88]. For nighttime

application, early works were focused on thin films and bulk materials with emission peaks in the Earth's transparent "sky window" [89]. In a study, focused on the intrinsic property of materials, polyethylene film with SiC and SiO_2 nanoparticles was found to have strong emission in the "sky window" with theoretical cooling temperature 25 °C below the ambient temperature of 17 °C and with a non-radiative heat transfer coefficient, $h_c = 2$ W/m^2-K [77]. Metamaterials can also be used to tune emission properties as shown by Hossain et al. where metal-dielectric conical pillars were used with an emission peak between 8-13 μm wavelength [90]. This structure showed a potential cooling of 58 °C below ambient temperature, neglecting non-radiative heat transfers.

On the other hand, daytime radiative cooling is challenging because even a small percentage of solar absorption (solar intensity ~ 1000 W/m^2) [91] during the day could balance out the outgoing cooling power (100-150 W/m^2) of the structure. For daytime radiative cooling, a material should possess low absorptivity in the solar spectrum (0.3-2.5 μm) region and high emissivity in the "sky window". A photonic structure with alternating layers of hafnium dioxide (HfO_2) and silicon dioxide (SiO_2) was reported to reach a cooling temperature 5 °C below ambient temperature [92]. Recently a radiative cooling structure made of wood has been reported with an average cooling power of 53 W/m^2 over 24 hours [93]. This particular structure is exciting because unlike previously reported structures where vacuum deposition and nanofabrication instruments were necessary, this one is practical for mass production. Attaching this wood to a surface will allow that surface to cool down by 10 °C and could reduce air conditioning costs by 60% in warm climates [94]. It is also interesting that most of these structures didn't make any use of incoming solar radiation as it was reflected. Combining this technology with other applications where incident sunlight is utilized would reduce designing

demands/cost for the radiative cooler for daytime application. A solar cell can convert 6-20% of the incident sunlight into electricity depending on the climate and absorber material. The remaining sunlight is converted into heat which significantly increases the temperature of the solar cell. The higher operating temperature of the cell would increase internal carrier recombination and decrease the performance of the solar cell [95]. For crystalline silicon solar cells, every 1 °C increase of solar cell operating temperature would lead to a relative efficiency decrease of 0.45% [96]. Combining radiative cooler and solar cell technologies, without affecting incoming solar spectrum, could ensure lower operating temperature for solar cells providing higher output power.

Lignin is a complex polymer that is found in plant cell walls and a by-product of the paper industry, with around 50 million tons produced every year [97]. It could play a pivotal role in the development of environmentally friendly polymer composite. Due to its huge chemical structure, lignin can be used as filler, reinforcing agent, stabilizer, etc.

In this chapter, we present a study on a lignin-upgraded polymer structure for the radiative cooling application. The reflectivity and emissivity of the sample were measured, and the cooling power and temperature of the sample were studied both theoretically and experimentally. We also showed that placing this polymer under a polycrystalline silicon solar cell would reduce the operating temperature of the solar cell and increase efficiency.
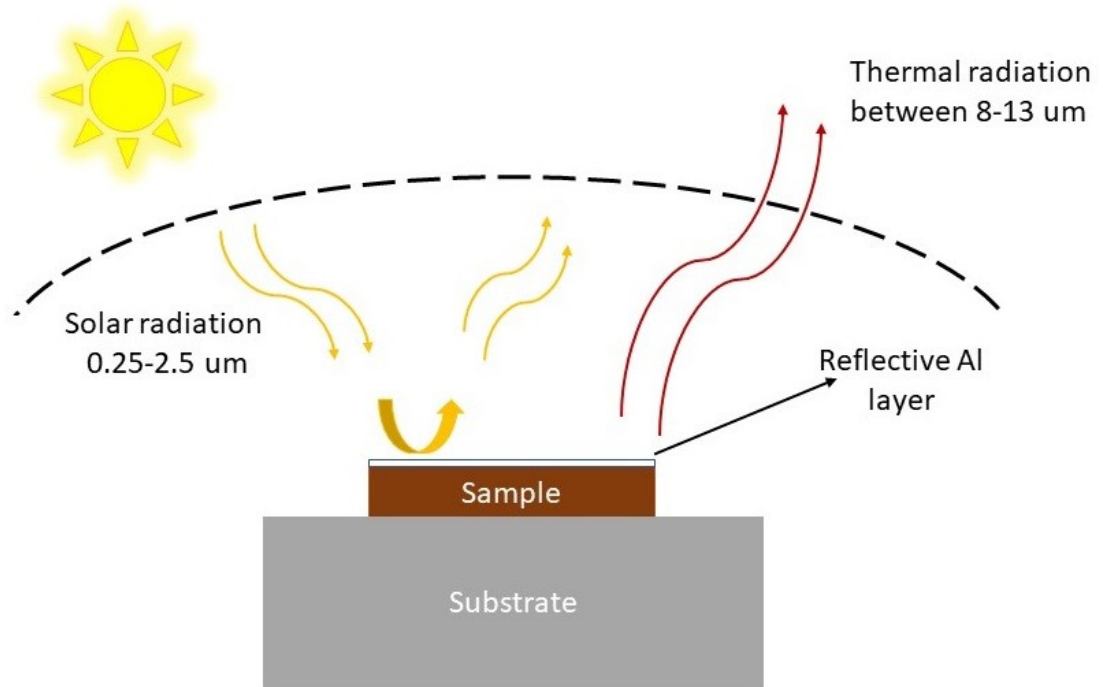
Figure 20. A schematic of the proposed structure for daytime radiative cooling.

3.2. Working principle of radiative cooling

Radiation from the environment, also known as environmental radiation, comprises solar irradiation and infrared radiation emitted from the earth's surface. The temperature of the earth's surface is determined by the interaction between environmental radiation and the earth's atmosphere and this interaction maintains the energy balance (see Figure 21 (a)). Solar radiation, which is between 0.3-2.5 μm, can be absorbed, reflected, or scattered by air molecules and clouds of our atmosphere. This atmosphere is also receiving the radiation generated by the earth's surface which is the terrestrial emission. The wavelength of this
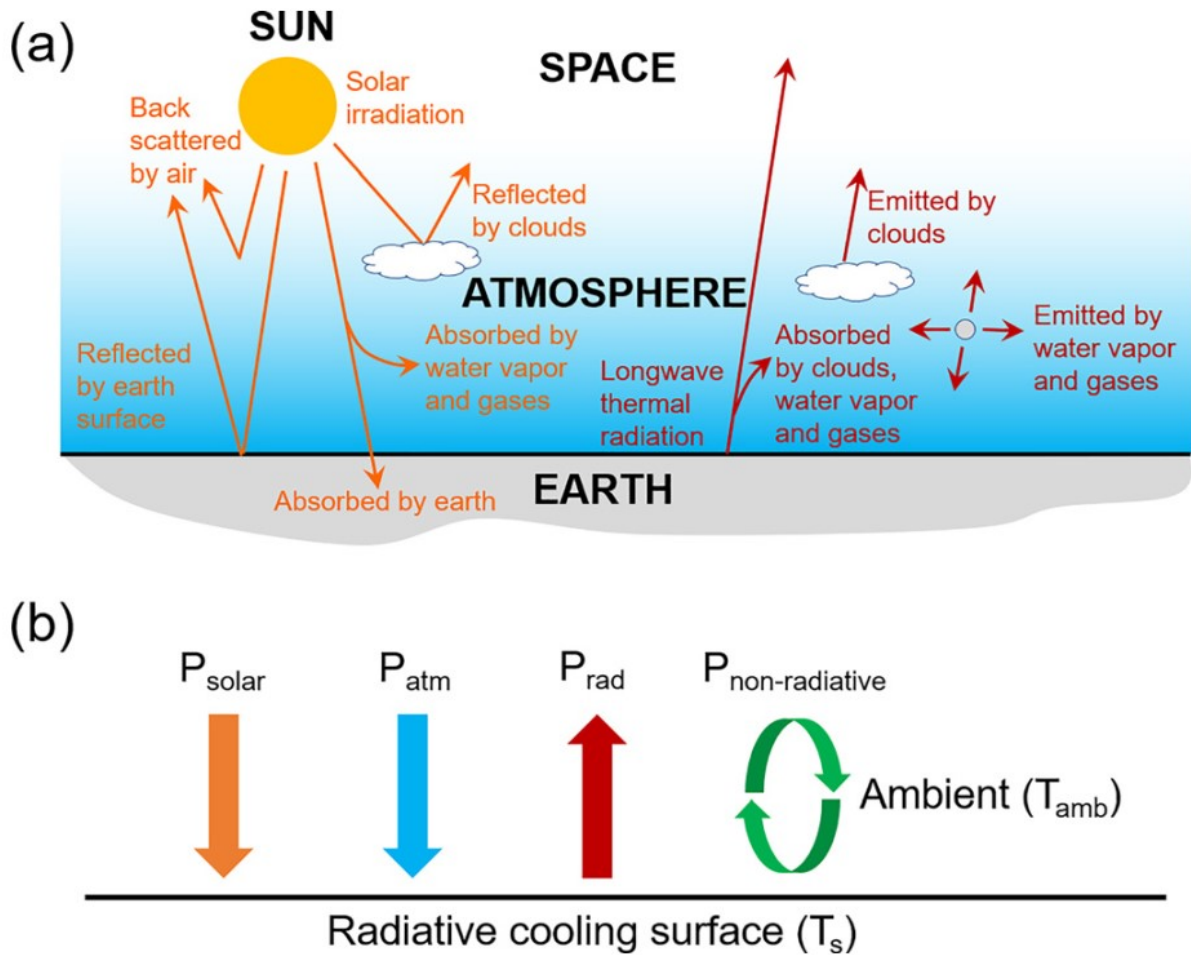
Figure 21. Fundamentals of radiative sky cooling. (a) On a global scale, the earth gains energy from the sun and radiates the same amount of thermal energy to the universe to maintain its energy balance. (b) Heat transfer processes on a radiative cooling surface. Reprinted with permission from [98]. Copyright AIP publishing, license number: 4992631434345.

radiation can be determined by Planck's law and for a surface temperature of 300 K, this upward radiation falls between 2.5-50 μm range. Like downward solar radiation, this upward terrestrial radiation while propagating through the atmosphere also experiences absorption and

scattering. Figure 21 (b) is showing a simplified version of the energy flows at the earth's surface. For a structure on the ground that is exposed to the atmosphere, net radiation is determined by considering solar irradiation (during the day) and terrestrial radiation. The net radiative cooling power (P_{net}) at temperature T can be calculated by [92,99]:

$$P_{net}\ (T) = P_{rad}(T) - P_{atm}(T_{atm}) - P_{sun} - P_{nonrad} \tag{1}$$

Here P_{rad} is the thermal radiation from the structure, P_{atm} is the incoming atmospheric radiation absorbed by the structure, P_{sun} is the absorbed solar irradiation and P_{nonrad} denotes nonradiative heat transfer between the structure and ambient.

Now the power radiated by the structure is [92,99]:

$$P_{rad}(T) = \int_0^\infty \varepsilon\,(\lambda)\ E_b(\lambda, T)\ d\lambda \tag{2}$$

where $E_b\ (\lambda,\ T)$ is the blackbody radiance of the structure at temperature T and $\varepsilon\ (\lambda)$ is the spectral emissivity of the structure. Now due to incoming atmospheric thermal radiation, absorbed power by the structure is [92,99]:

$$P_{atm}(T_{atm}) = 2\pi \int_0^{\frac{\pi}{2}} \int_0^\infty \varepsilon(\lambda)\ \varepsilon_{atm}(\lambda, \theta)\ E_b(\lambda, T_{atm})\ d\lambda\ cos\theta\ d\theta \tag{3}$$

where $E_b\ (\lambda,\ T_{atm})$ is the blackbody radiance of the atmosphere at temperature T_{amb} and $\varepsilon_{atm}(\lambda, \theta)$ is spectral directional emissivity of the atmosphere which is equal to $1 - t\ (\lambda,\ 0)^{1/cos\theta}$ where $t\ (\lambda,\ 0)$ is the atmosphere transmittance in the zenith direction. Now power absorbed due to incoming solar radiation is [92,99]:

$$P_{sun} = \int_0^\infty \varepsilon(\lambda)\ E_{AM1.5}(\lambda)\ d\lambda \tag{4}$$

where $E_{AM1.5}$ is solar irradiation and integration of this between 0.25–3 μm is around 1000 W/m^2. The structure will lose some power due to conduction and convection which is [92,99]:

$$P_{nonrad} = h_c\ (T_{amb} - T) \tag{5}$$

where T_{amb} is the ambient temperature, T is the structure temperature and h_c is the non-radiative heat transfer coefficient due to convection and conduction. Now a positive cooling power from the structure will only be possible if the radiation from the structure is greater than the combined effect of atmospheric radiation, solar irradiation, and non-radiative heat loss.

3.3. Experiment

Figure 20 shows a schematic of the proposed structure. The sample which has high emissivity within the "sky window" is covered with Al foil to reflect all incoming solar radiation. Lignin was acquired from the West Fraser pilot plant with a pH value of 10.4. This lignin tends to be hydrophilic and hence water-soluble. This material is around 60% dry solids. Solubility increases when diluted caustic soda is added. Lignin with different weight percentages was taken into a petri dish and 200-500 μL of water was added to improve its solubility and homogeneity. After that, 2 mL of PDMS was added with its curing agent and the mixture was stirred vigorously. The sample was then heated at 60 °C for 10 minutes and then degassed in a vacuum chamber for 15 minutes to remove the air bubble from the film. The sample was cured afterward at 90 °C for 30 minutes to obtain a solid, flexible film which was taken out of the petri dish. PDMS sample was prepared following the same recipe without adding any lignin material. The thickness of the samples is 1.4 ± 0.5 mm. Figure 22 is showing the fabricated samples.
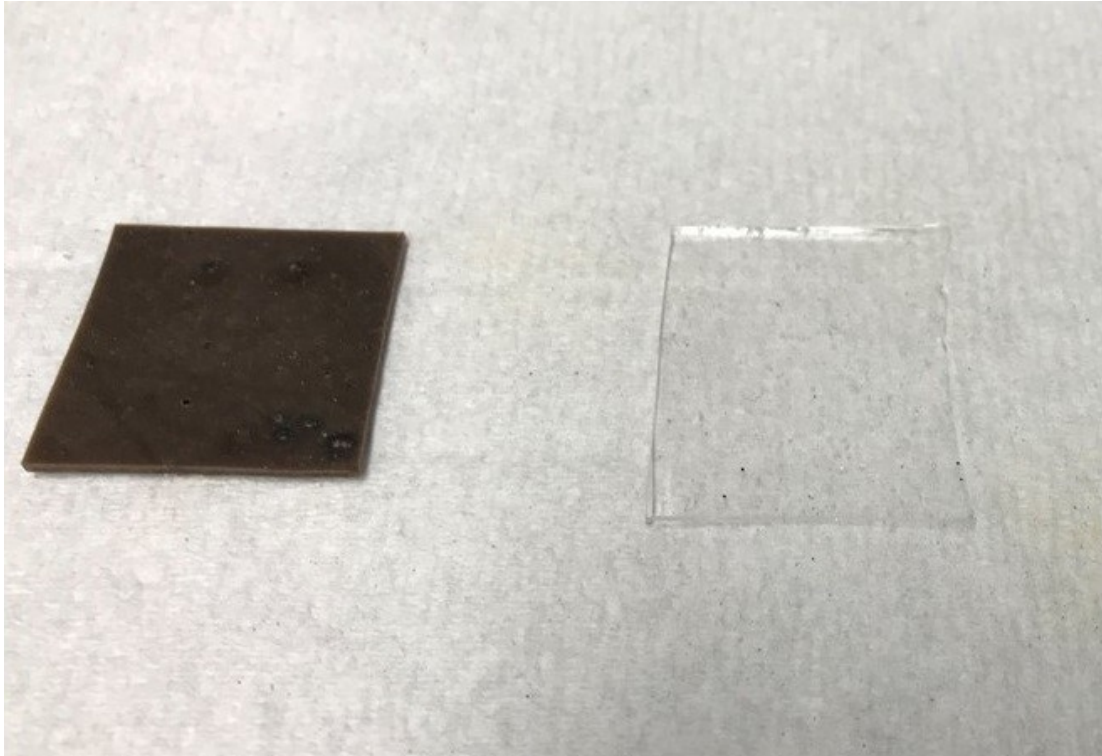
Figure 22. Fabricated samples for radiative cooling application where the left one contains lignin and PDMS and the right one is pure PDMS.

Polycrystalline silicon solar cells of size 15.6 x 15.6 cm and thickness between 180-200 μm were purchased [100]. These cells had silicon nitride as an antireflecting coating and, Al front and back contacts. These cells were later cut to pieces with the size of 3 x 3 cm using a dicing saw. A radiative cooler was placed below these solar cells and characterized under AM1.5G solar spectrum.

3.4. Results and discussion

3.4.1.   Spectral emittance

The spectral hemispherical reflectance (R) of the sample between 4000-600 cm^{-1} (2.5-16.66 μm) was measured by a Fourier-transform infrared spectrometer using the attenuated total reflection sampling technique. The measured absorption (A) of the sample was calculated using the formula: $A = 1-R$ and this absorption equal to the absorptivity and emissivity of the sample [101]. The absorptivity of the Al foil was also measured and found to be negligible in our window of interest.
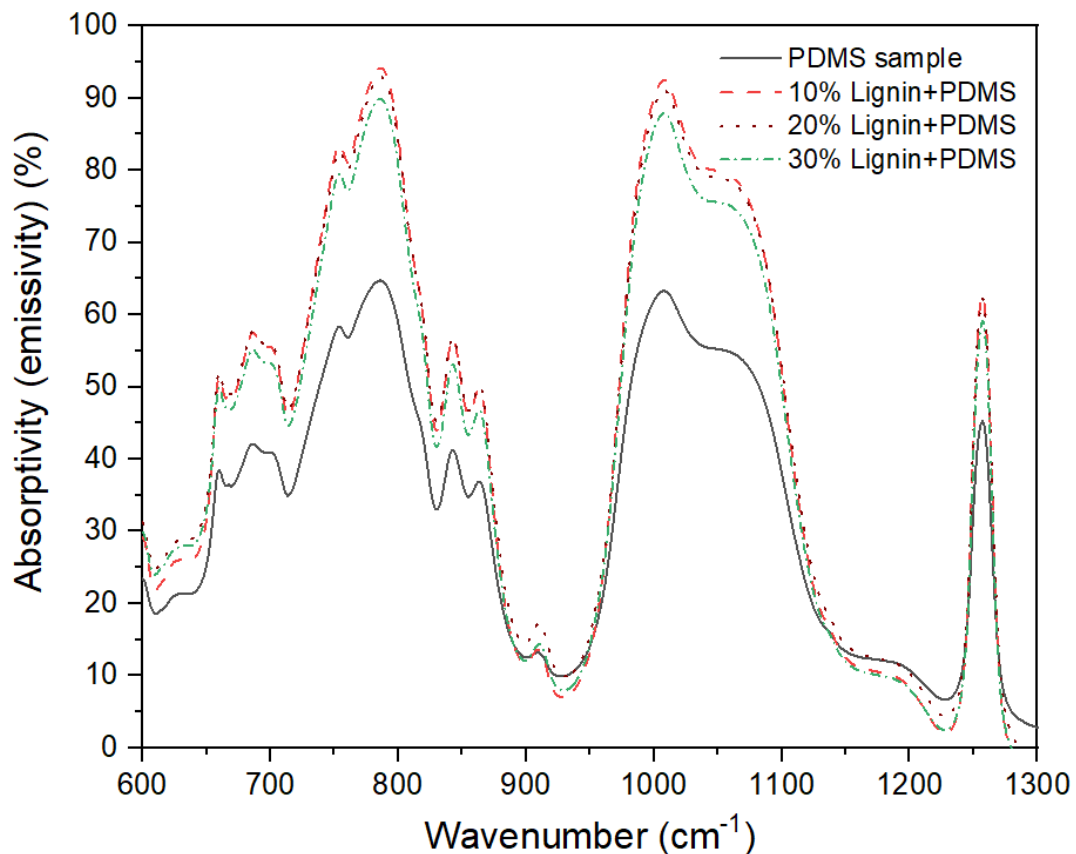
Figure 23. Spectral absorptivity (emissivity) of pure PDMS, 10 wt.%, 20 wt.%, and 30 wt.% lignin samples.

Figure 23 shows the absorptivity (emissivity) of the PDMS sample and samples with 10 wt.%, 20 wt.%, and 30 wt.% lignin mixed with PDMS. The absorption of these samples between 1300-4000 cm^{-1} (wavelength of 2.5-7.7 μm) can be found in Appendix, Figure 49. Absorption bands at 1265 cm^{-1} and 780 cm^{-1} are related to the deformations of the C–H bond of Si(CH$_3$)$_2$ groups [102,103]. Absorption between 1000-1110 cm^{-1} is related to the asymmetric stretching of Si–O–Si [102,103]. From the figure, it is clear that adding lignin has significantly increased the emission of the samples. Previously it was found that lignin has various absorption bands e.g., at 1125 cm^{-1} due to deformation vibration of C–H bonds in syringyl rings, at 1085 cm^{-1} due to deformation vibration of C–O bonds in secondary alcohols and aliphatic ethers, at 870 cm^{-1} and 780 cm^{-1} due to deformation vibrations of C–H bonds in associated aromatic rings [104]. Adding lignin with PDMS does improve the overall absorptivity of the sample and interestingly, lignin-upgraded samples showed similar type of absorption peaks like pure PDMS but at a higher intensity which may be because the weight percentage of PDMS is significantly more than lignin in our matrix material and peaks related to lignin got covered by the absorption bands related to deformations of the C–H bond of the Si(CH$_3$)$_2$ groups and asymmetric stretching of Si–O–Si of the PDMS base. Figure 23 suggests 10 wt.% and 20 wt.% will give almost similar emission and it will decrease slightly for 30 wt.% sample which still had higher emission compared to PDMS sample. The results shown in the following sections are for a 10 wt.% lignin sample.

3.4.2. Theoretical cooling performance
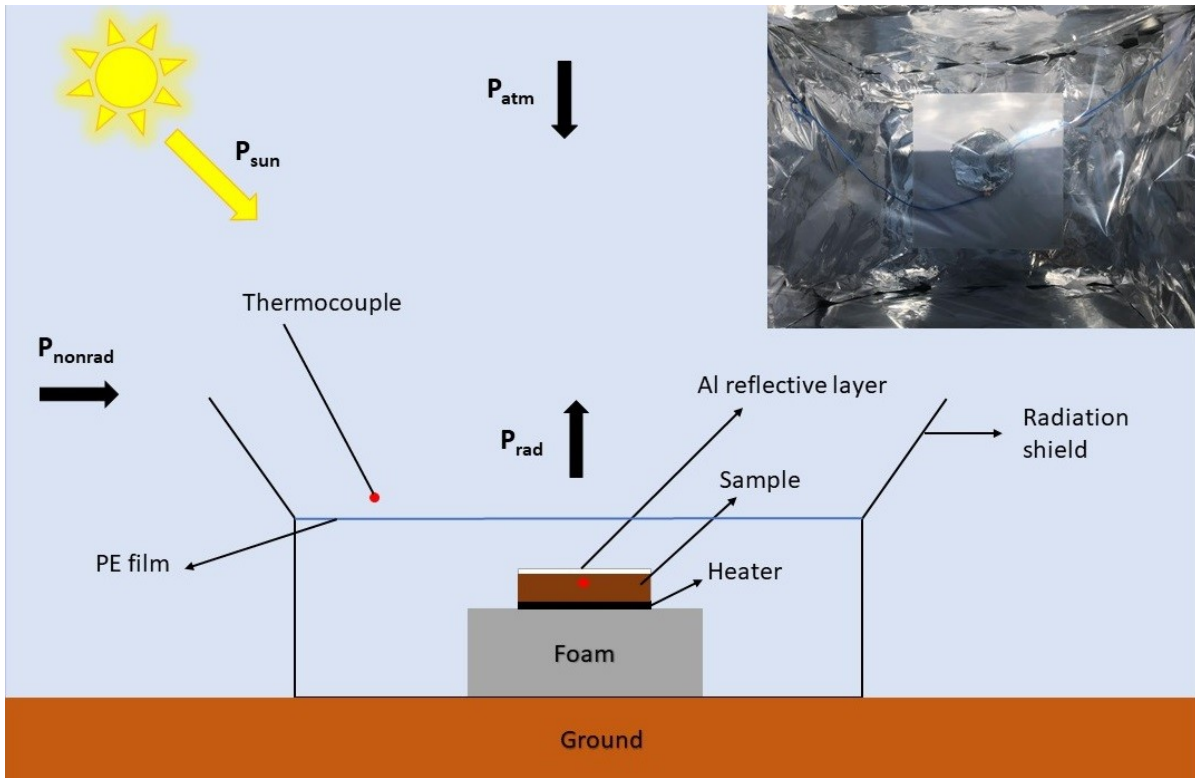
Figure 24. Schematic of the outdoor setup for testing the radiative cooling performance of the sample under sunlight showing different incoming and outgoing radiations that determine the cooling ability (P_{net}) of the sample.
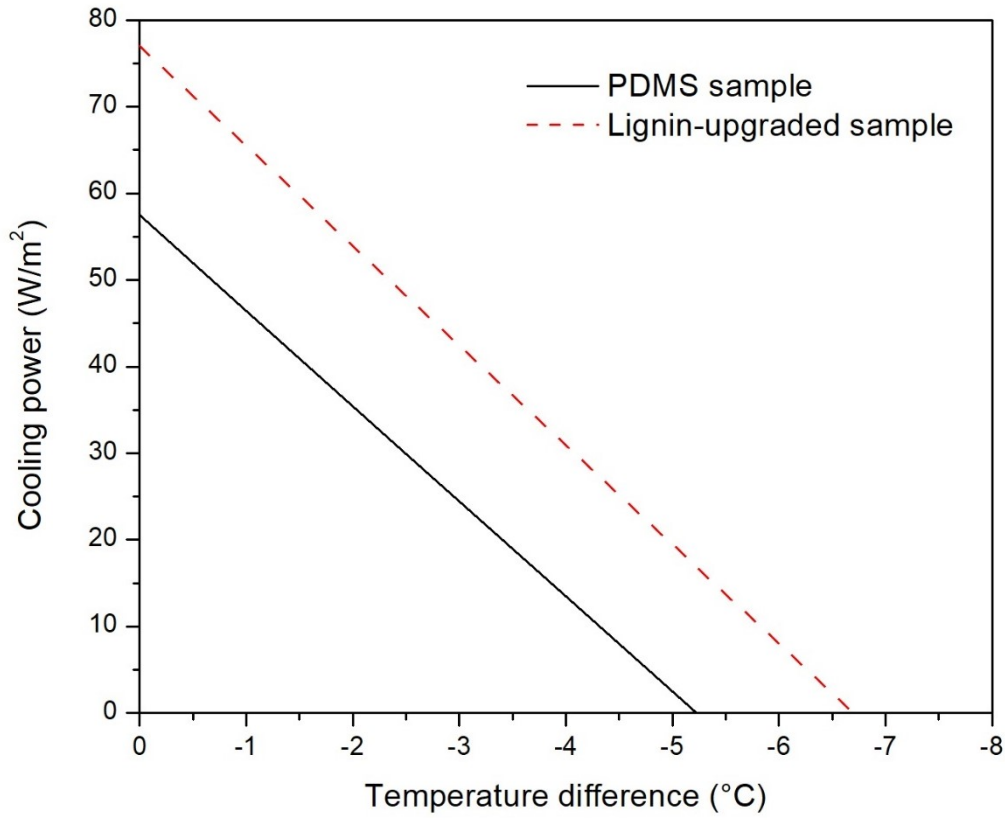
Figure 25. The theoretical cooling power of the PDMS and lignin-upgraded samples.

Using the equations mentioned in section 3.2, the cooling powers of the samples were calculated as a function of the temperature difference and several assumptions were made for calculating theoretical cooling powers such as the temperature of the ambient, T_{amb}, was assumed to be 25 °C, non-radiative heat transfer coefficient, h_c, was assumed to be 8.9 W/m²-K during our calculation due to high humidity of the surroundings which is within the range specified elsewhere [105,106]. The atmospheric transmittance data were collected from previously published data [82]. The value for AM1.5G was taken from data published by NREL [107].

Figure 24 is showing a schematic of the experimental setup with different types of radiations that determine the net outgoing radiation (P_{net}). Figure 25 shows the theoretical cooling powers of the PDMS and lignin-upgraded samples vs. temperature difference ($T_{sample} - T_{ambient}$). Stagnation temperature is the temperature at which cooling power goes to zero and for PDMS and lignin upgraded samples, stagnation temperatures were 5.2 °C and 6.65 °C below ambient temperature, respectively. Power required to equal sample and ambient temperatures, which in this case means zero temperature difference, is known as cooling power. For the PDMS sample, it was found to be 57 W/m^2 and for the lignin-upgraded sample, it was 77 W/m^2. These results show that adding lignin would significantly improve the cooling ability of the sample.

3.4.3.   *Experimental cooling performance*

The on-site cooling experiment was carried out to investigate the performance of lignin-upgraded samples during the daytime. The sample had a diameter of 52.5 mm and a thickness of 1.4 ± 0.5 mm. Al foil paper is placed on top of the sample to reflect solar radiation. Previously different methods have been used to reduce absorption in solar spectrum e.g., using Al substrate [106], silver substrate or depositing Ag film on the back [101,108], using nanoparticles [109], etc. Most of these techniques require additional tool or material that increases associated cost. It was found that lignin can absorb a significant amount of solar radiation which would reduce its cooling capability and since the sample was opaque, placing a substrate beneath would not work. A simple and cost-effective solution was introduced by using Al foil as a top cover since it has high reflectivity in the solar spectrum which reduces solar absorption by the sample. More information about the effect of Al foil can be found in Appendix, Figure 50.

Figure 24 shows the setup where the sample was placed inside a thermal box and, the side and bottom walls were covered with Al foil. The sample was placed on top of the foam and the top side of the box was covered by polyethylene (PE) film. This box helped to suppress non-radiative heat exchange with the surroundings. Two k-type thermocouples were used to measure the temperature of the sample and the surrounding temperature.
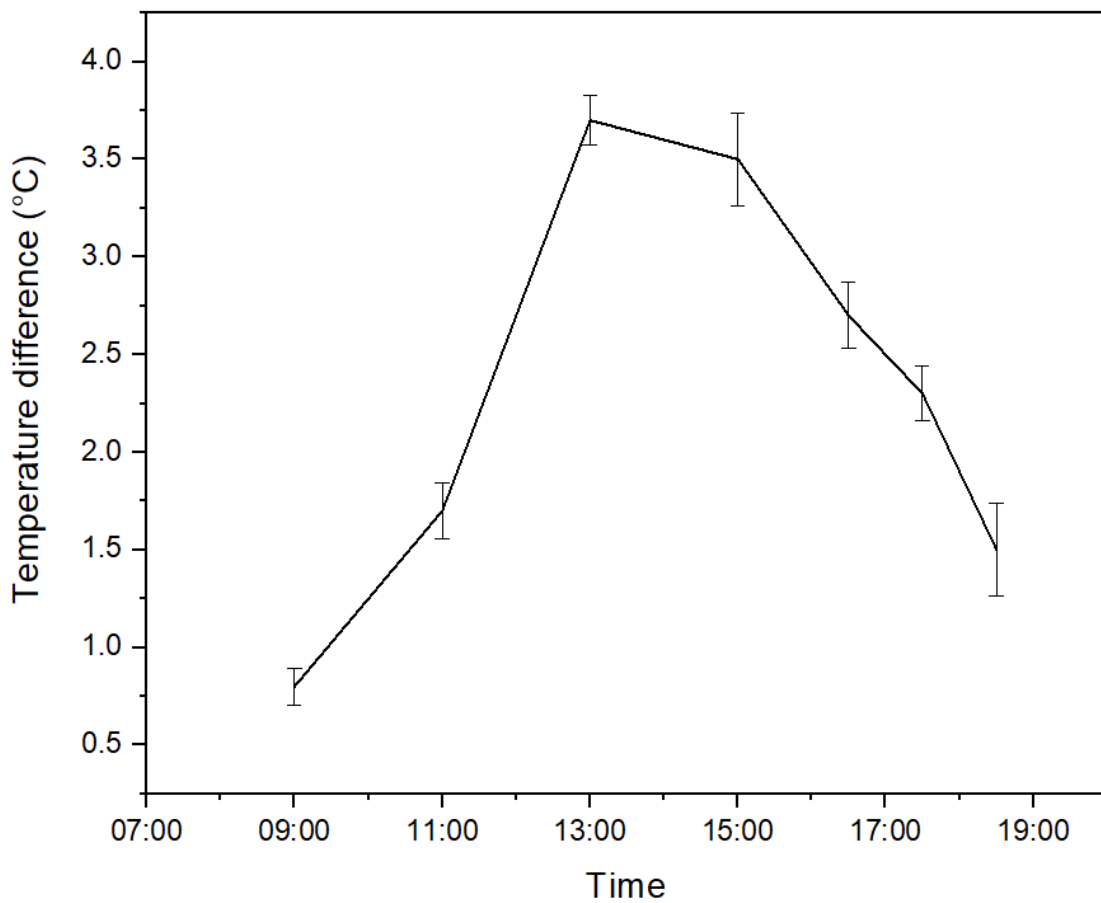
Figure 26. Outdoor measurement of the radiative cooler placed under direct sunlight.
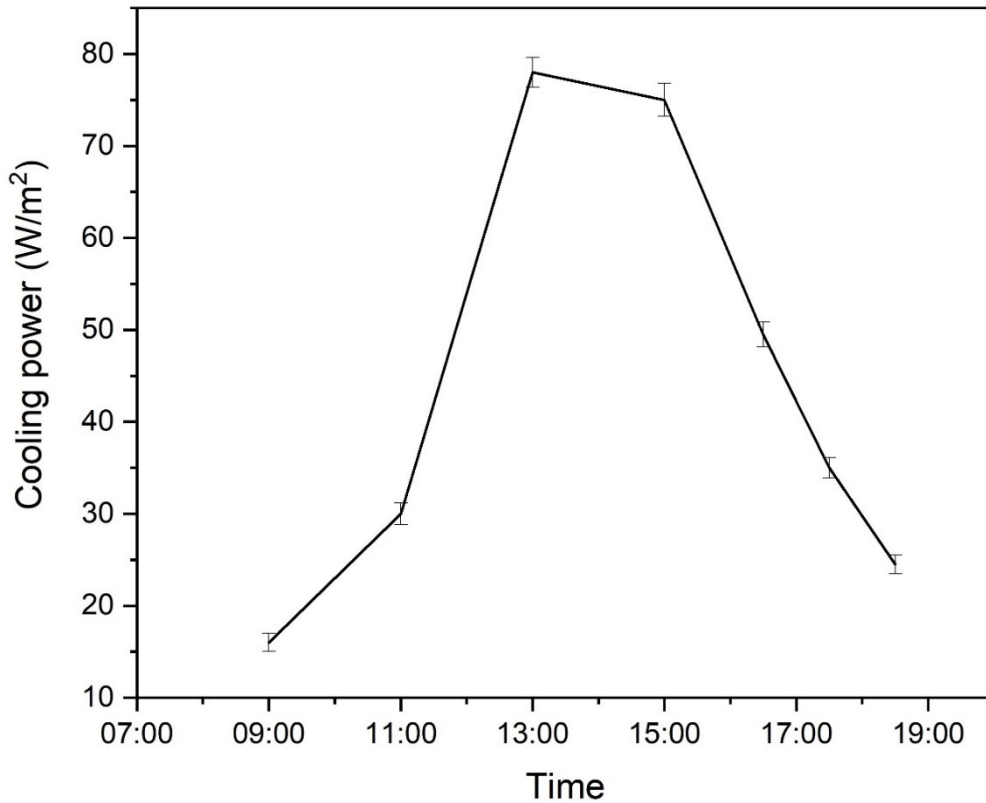
Figure 27. The experimental cooling power of the lignin-upgraded sample.

The measurement was performed in an open field at the University of Alberta at ~70% humidity. The temperature variation ($T_{ambient}$ - T_{sample}) between the sample and the surrounding was monitored during the day and plotted in Figure 26. More information regarding experimental conditions can be found in Appendix, Figure 51, and Figure 52. It shows the maximum cooling temperature sample reached which was 3.7 °C below the surrounding temperature. A resistive heater was placed below the sample to provide heat to keep the sample and ambient temperatures the same, and the power provided to the heater to match these temperatures is the cooling power. is showing the cooling powers achievable from the sample (cooling power of the PDMS sample is shown in Appendix, Figure 53). It shows that the

maximum cooling power provided by the sample would be 78 W/m^2. On the other hand, the stagnation temperature achieved during the experiment was 3.7 °C, which is lower than the theoretical prediction of 6.65 °C. This is mainly due to higher non-radiative heat losses than predicted. We believe an improved experimental setup to lower non-radiative heat loss would have provided better results.

3.4.4.   *Application of lignin-upgraded polymer in solar cell*

As a proof of concept, the effect of the lignin-upgraded sample was studied on a solar cell and for that purpose, it was placed on the backside of silicon solar cells. Under AM1.5G illumination, a reduction in operating temperature by 3 °C was observed. More information about the setup and sample temperature can be found in Appendix, Figure 54, and Figure 55. Figure 28 shows the current-voltage characteristics of the solar cells and it shows that with radiative cooler, short circuit current decreases but open-circuit voltage increases. Higher temperature induces thermal carrier excitation which increases the short circuit current. At the same time, higher operating temperature increases the energy of electrons in the material and decreases the bandgap which reduces the open-circuit voltage and fill factor. Though lower operating temperature would reduce short circuit current slightly, it would also reduce the energy of electrons and ensure higher open-circuit voltage and fill factor, providing higher output power. Table 3 summarizes the performance of the solar cells with and without lignin-upgraded samples.
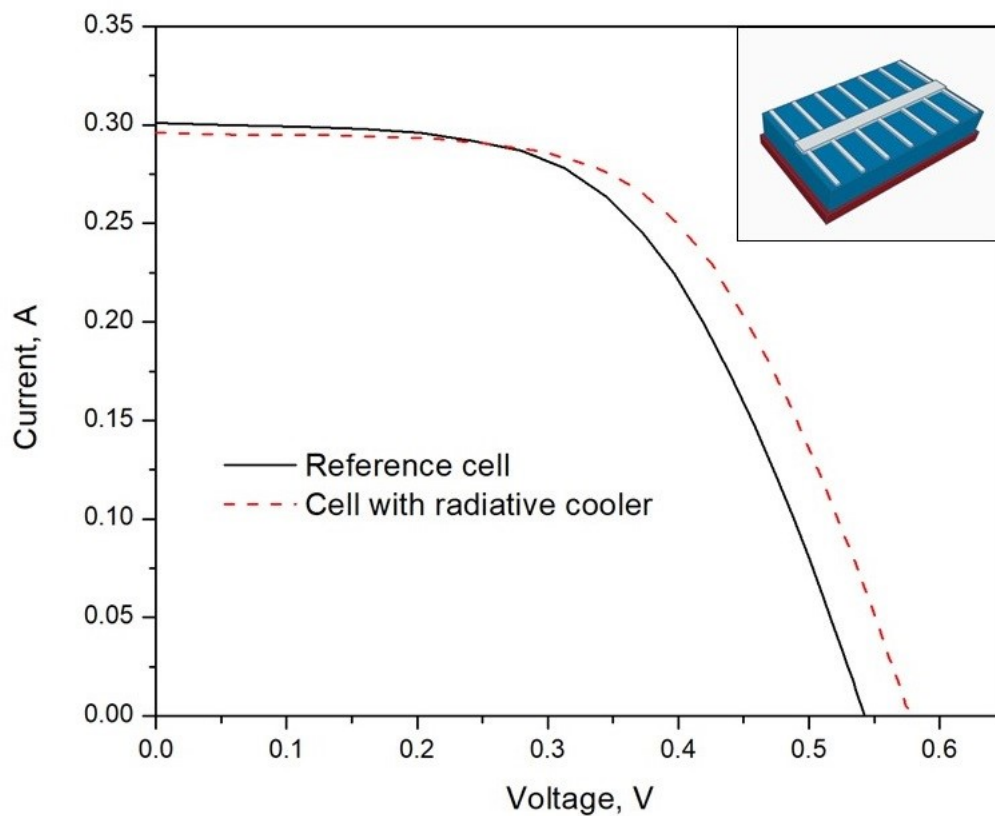
Figure 28. Current-voltage characterization of the solar cell under AM1.5G solar spectrum. Inset shows a schematic of the solar cell with a radiative cooler placed underneath.

Table 3. Summary of results.

	Reference cell	Solar cell with lignin-upgraded sample
V_{oc} (V)	0.544±0.001	0.571±0.008
I_{sc} (A)	0.298±0.002	0.286±0.01
Fill Factor (%)	56.3±0.1	58.3±0.7
Efficiency (%)	10.14±0.03	10.59±0.03

3.5. Conclusion

In this chapter, we have presented a novel application of wood-derived lignin biopolymer for radiative cooling by mixing it with another eco-friendly material PDMS. In this work, the lignin-upgraded polymer was found to have higher thermal emission compared to bare PDMS material. In the region between 8-13 μm, lignin-upgraded polymer showed emission peaks over 90%. Due to the dark color of lignin, which suggests high absorption of solar radiation, an Al reflector was used that enables this structure to be used during daytime. Further modification of the lignin structure can be made to produce light-colored lignin and people have already started focusing on that aspect [110,111]. This will help to remove the application of reflectors from the top of the structure and might produce better radiative cooling performance. Our current lignin sample would be more suitable for nighttime radiative cooling, but the possibility of daytime radiative cooling is explored in this work since it has gained a lot of attention in the past few years. We have also shown a possible application of lignin-upgraded polymer in solar cells by placing the polymer on the backside of the cell. Due to the dark color of the sample, it was not possible to place it on the front side of the cell which might have provided a higher performance boost. Even though further investigation with light-colored lignin is required and the long-term prospect of placing such radiative cooler with solar cell needs to be investigated, this study still provides an excellent platform for future efforts to investigate new materials for radiative cooling and explore potential applications.

Chapter 4: Cellulose-upgraded polymer films for radiative sky cooling

4.1. Introduction

Cellulose, which as mentioned earlier, is a polymer that is found in plant cell walls and one of the most abundant natural polymers on the planet. The primary structure of cellulose had been identified as a linear homopolymer of glucose residues with D configuration linked by β-(1 $\rightarrow$ 4) glycosidic linkages [24]. Several works have studied cellulose material for the radiative cooling application. For example, the Al_2O_3-cellulose acetate structure was reported [112] and was used as a textile material. In this work, Al_2O_3 was dispersed in a solution and cellulose acetate was mixed later. This solution was then painted and dip-coated on textile material and found to decrease the temp of the textile by 1.9-3.3 °C and human skin by 0.6-1 °C. In another work, SiO_2 powder and wood fiber suspensions were mixed to prepare cooling lignocellulosic bulk by hot-pressing [113]. This bulk material was able to achieve cooling with an average temperature difference of 6 °C and 8 °C during day and night, respectively. This material also showed superior strength and flame retardancy. Another study reported a cooling paper by mixing cellulose nanofibrils (CNF) and silicon dioxide (SiO_2) microparticles that reached a cooling temperature 3 °C below ambient temperature [114]. Interestingly, SiO_2 [115] and Al_2O_3 [106] materials were previously investigated and found to have excellent radiative cooling ability. Hence, adding these materials with cellulose would further improve the overall performance of the radiative cooling structure. In this study, we focused solely on cellulose and mixed it with PDMS material, which is an eco-friendly material with no ecological threat [116–118], and studied its potential for radiative cooling. This structure provided better

strength compared to the structure developed earlier [119] due to the addition of PDMS. The reflectivity and emissivity of these cellulose-upgraded samples were measured, and the cooling power and temperature of the samples were studied both theoretically and experimentally. We also showed a potential application of this polymer in conjunction with a silicon solar cell that would reduce the operating temperature of the cell and increase efficiency.
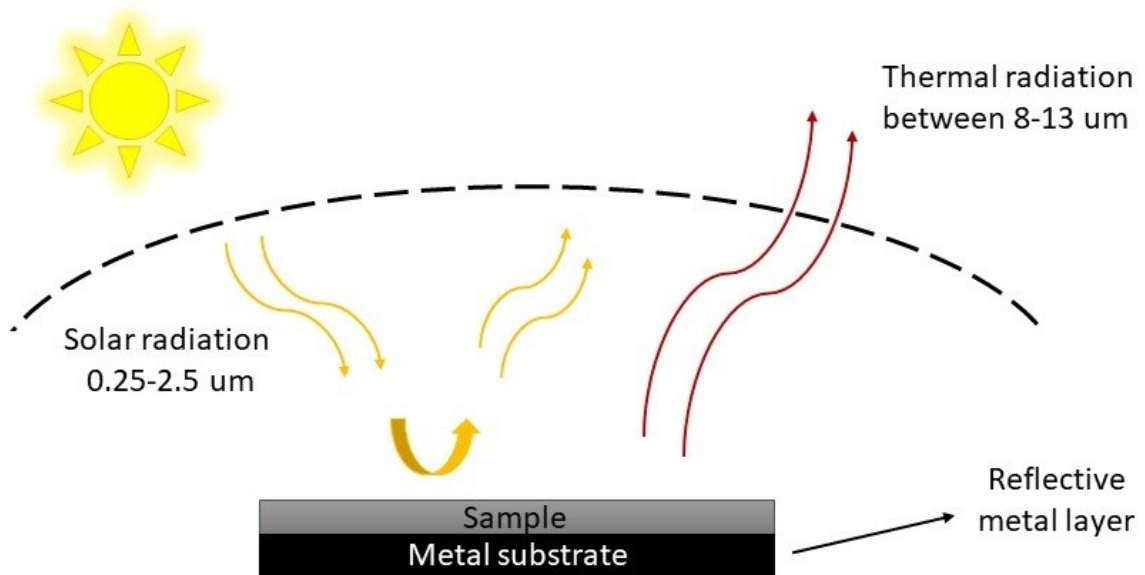
Figure 29. A schematic of the proposed structure for daytime radiative cooling.

4.2. Experiment

Figure 29 shows a schematic of the proposed structure. The sample has high emissivity within the IR-transparent window of the atmosphere and has a metal substrate to reflect all incoming solar radiation.

Cellulose nanocrystals (CNCs) were synthesized by the acid hydrolysis process. Sulfuric acid with a concentration of 64% and at 45 °C was used during the hydrolysis which was performed

at first using two Pfaudler 50-gallon (189 liters) acid-resistant glass-lined reactors with a steam-heated jacket. A GEA Westfalia SC-35 separator was used to centrifuge and at the end, CNCs powder was dried in an SPX-Anhydro Model 400 Spray Dryer Plant at the conditions of a 220°C inlet temperature and an 85 °C outlet temperature. Polydimethylsiloxane (PDMS) was outsourced from Sigma-Aldrich [120].

CNCs with different weight percentages were taken into a petri dish and 2 mL of PDMS was added with its curing agent and the mixture was stirred vigorously. The sample was then heated at 60 °C for 10 minutes and then degassed in a vacuum chamber for 15 minutes to remove the air bubble from the film. The sample was cured afterward at 90 °C for 30 minutes to obtain a solid, flexible film which was taken out of the petri dish. PDMS sample was prepared following the same recipe without adding any CNCs material. The thickness of the samples is 1.45 ± 0.5 mm. Figure 30 is showing some of the fabricated samples.
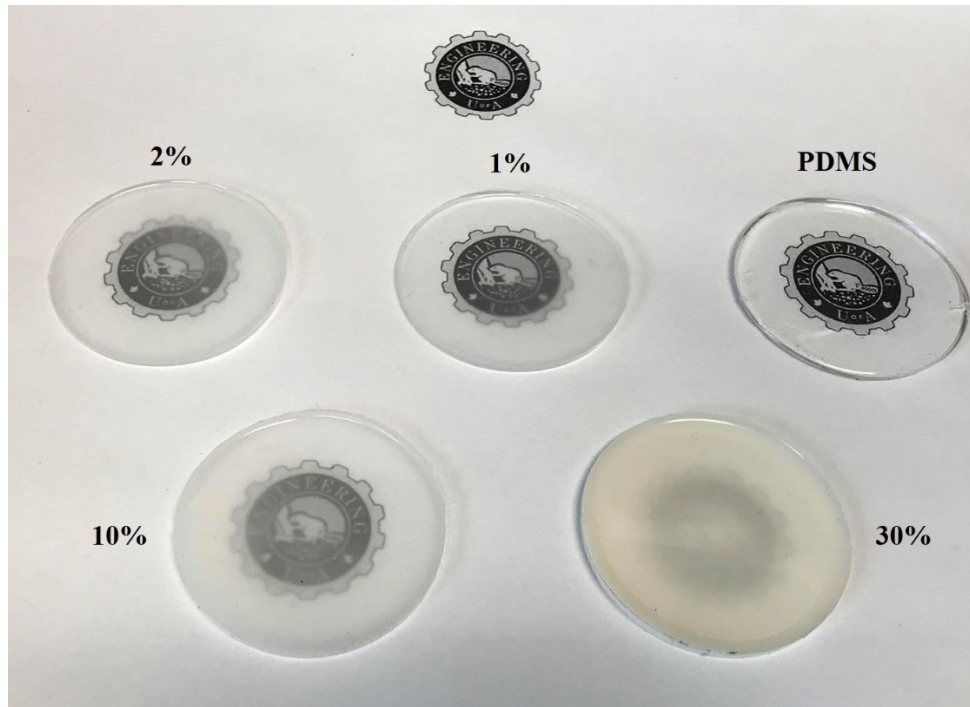
Figure 30. Fabricated samples for radiative cooling application with various CNCs concentrations.

Polycrystalline silicon solar cells of size 15.6 x 15.6 cm and thickness between 180-200 μm were purchased [100]. These cells had silicon nitride as an antireflecting coating and, Al front and back contacts. These cells were later cut to pieces with the size of 3 x 3 cm using a dicing saw. A radiative cooler was placed in direct contact with the solar cells and thorough characterization was performed to study its effect.

4.3. Results and discussion

4.3.1.   Spectral emittance

The spectral hemispherical reflectance (R) of the sample between 4000-600 cm^{-1} (2.5-16.66 μm) was measured by a Fourier-transform infrared spectrometer using the attenuated total reflection sampling technique. This equipment has a spectral resolution of 0.125 cm^{-1} and the minimum energy step is 0.482 cm^{-1}. The measured absorption (A) of the sample was calculated using the formula: $A = 1-R$, and this absorption equals the absorptivity and emissivity of the sample [101].
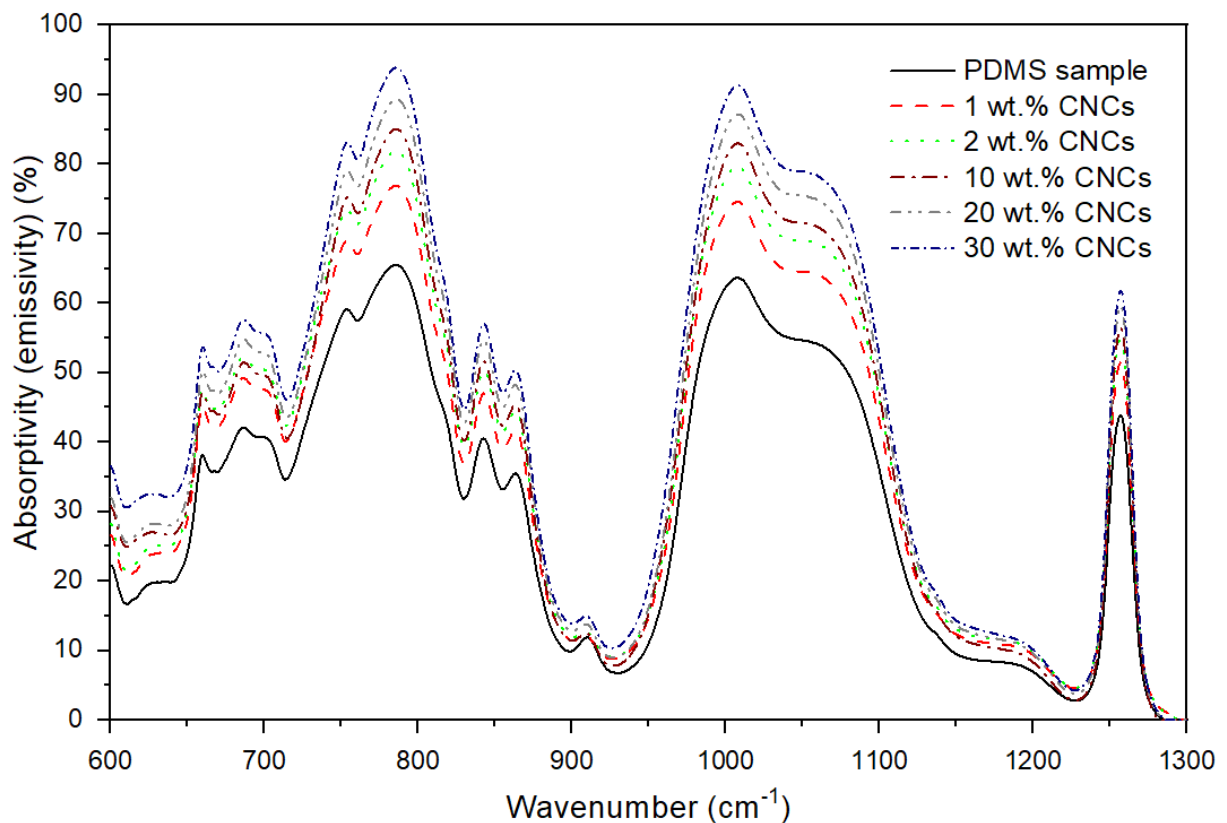
Figure 31. Spectral absorptivity (emissivity) of pure PDMS, 1 wt.%, 2 wt.%, 10 wt.%, 20 wt.% and 30 wt.% CNCs samples.

Figure 31 shows the absorptivity (emissivity) of PDMS sample and samples with 1 wt.%, 2 wt.%, 10 wt.%, 20 wt.%, and 30 wt.% CNCs mixed with PDMS. The absorption of these samples between 1300-4000 cm^{-1} (wavelength of 2.5-7.7 µm) can be found in Appendix, Figure 56. Absorption bands at 1265 cm^{-1} and 780 cm^{-1} are related to the deformations of the C–H bond of Si(CH$_3$)$_2$ groups [102,103]. Absorption between 1000-1110 cm^{-1} is related to the asymmetric stretching of Si–O–Si [102,103]. Figure shows adding CNCs have significantly increased the emission of the samples. Previously it was found that CNCs have various absorption bands e.g., at 3451 cm^{-1} due to O-H stretching vibration, around 2899 cm^{-1} due to C-H stretching vibrations and at 1644 cm^{-1} due to O-H vibration of absorbed water. At around 1382 cm^{-1}, there is a peak for C-H and C-O vibrations contained in the polysaccharide rings of cellulose. The vibration of C-O-C in the pyranose ring is indicated by the absorption peak at 1060 cm^{-1} [121,122]. Peaks between 1050-1056 cm^{-1} and 750-780 cm^{-1} are typically attributed to C-H and C-O deformation, stretching, and bending vibrations in various carbohydrate functional groups. Another peak located between 668-670 cm^{-1} corresponds to OH bending of absorbed water and C-OH out of phase bending of cellulose.

Adding CNCs in PDMS does improve the overall absorptivity of the sample and interestingly, cellulose-upgraded samples showed similar type of absorption peaks like pure PDMS but at a higher intensity which may be because the weight percentage of PDMS is significantly more than CNCs in our matrix material and peaks related to CNCs is covered by the absorption bands related to deformations of the C–H bond of the Si(CH$_3$)$_2$ groups and asymmetric stretching of Si–O–Si of the PDMS base. Figure 31 suggests an enhancement in absorption with increasing concentration of CNCs and maximum absorption is achieved by 30 wt.% sample.

4.3.2. Theoretical cooling performance
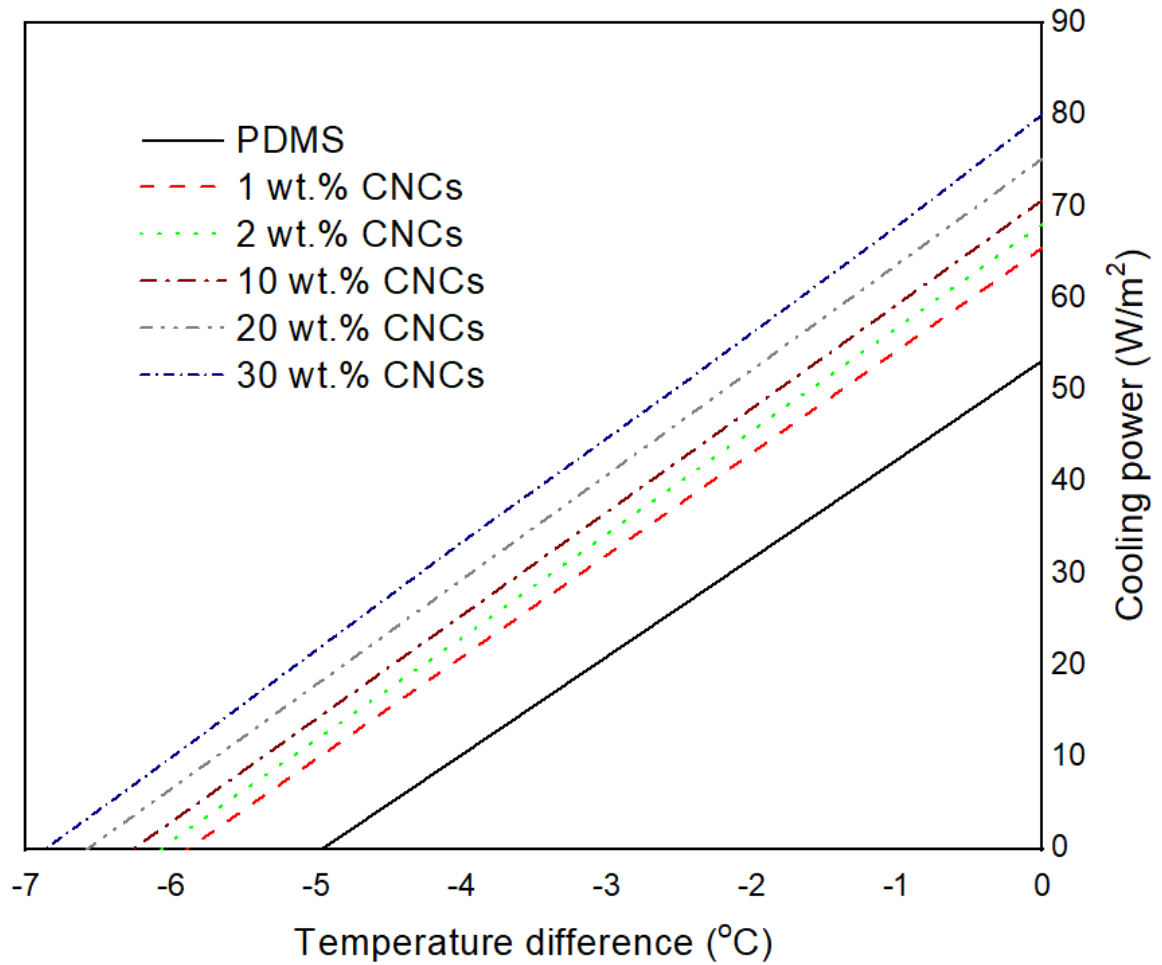
Figure 32. The theoretical cooling power of the PDMS and cellulose-upgraded samples.

Using the equations mentioned in section 3.2, the cooling powers of the samples were calculated as a function of temperature difference (T- T_{amb}) and for this calculation, several assumptions were made. The temperature of the ambient, T_{amb}, was assumed to be 25 °C. The non-radiative heat transfer coefficient, h_c, was assumed to be 8.9 W/m²-K during our calculation due to the high humidity of the surroundings which is within the range specified

elsewhere [105,106]. Atmospheric transmittance data was collected from another work [82] and data for AM1.5G was taken from NREL [107].

Figure 32 shows the theoretical cooling powers of the PDMS and cellulose-upgraded samples of various concentrations vs. temperature difference ($T_{sample} - T_{ambient}$). The temperature at which cooling power is zero is known as stagnation temperature and for the PDMS sample it is 4.95 °C below ambient temperature and for cellulose-upgraded samples, the temperatures are 5.85 °C, 6.05 °C, 6.25 °C, 6.58 °C, and 6.82 °C below ambient temperature for 1 wt.% CNC, 2 wt.% CNC, 10 wt.% CNC, 20 wt.% CNC and 30 wt.% CNC samples, respectively. The power required to equal sample temperature and ambient temperature is known as cooling power and for the PDMS sample it is 53.5 W/m^2 and for cellulose-upgraded samples, cooling powers are 65.8 W/m^2, 68 W/m^2, 70.05 W/m^2, 75.2 W/m^{2,} and 80 W/m^2 for 1 wt.% CNC, 2 wt.% CNC, 10 wt.% CNC, 20 wt.% CNC and 30 wt.% CNC samples, respectively. These results show that adding CNCs would significantly improve the cooling ability of the sample.
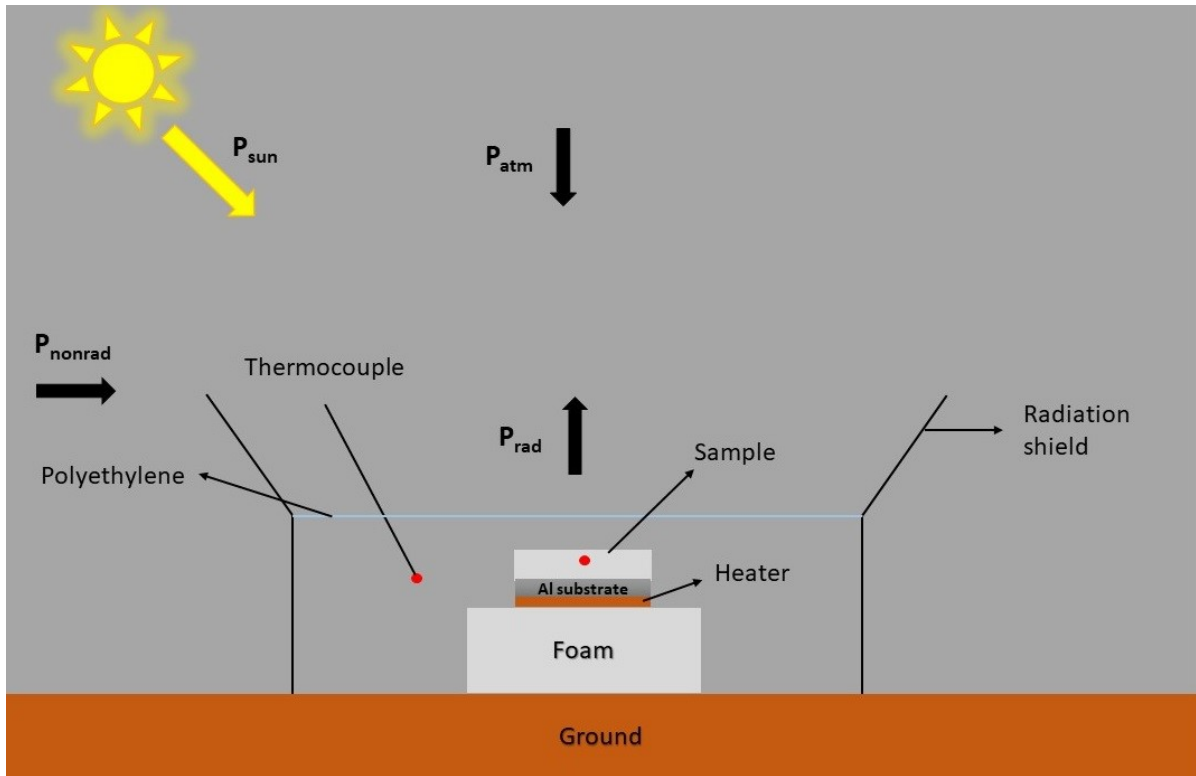
Figure 33. Schematic of the outdoor setup for testing the radiative cooling performance of the sample under sunlight showing different incoming and outgoing radiations that determine the cooling ability (P_{net}) of the sample.

4.3.3.   *Experimental cooling performance*

An on-site cooling experiment was carried out to investigate the performance of cellulose-upgraded sample during the daytime. For this experiment, 30 wt.% CNCs sample was chosen since it showed the highest emissivity. This sample had a diameter of 52.5 mm and a thickness of 1.45 ± 0.5 mm. The aluminum substrate was placed below the sample to reflect solar radiation which did not significantly change the emission of the overall structure but increased solar reflection (more information regarding experimental conditions can be found in Appendix, Figure 57 and Figure 58). Figure 33 shows the setup where the sample was placed

inside a thermal box and its side and bottom walls were covered with Al foil. The sample was

placed on top of the foam and the top side of the box was covered by 50 μm thick polyethylene

(PE) film. This box helped to suppress non-radiative heat exchange with the surroundings. Two

k-type thermocouples were used to measure the temperature of the sample and surroundings.
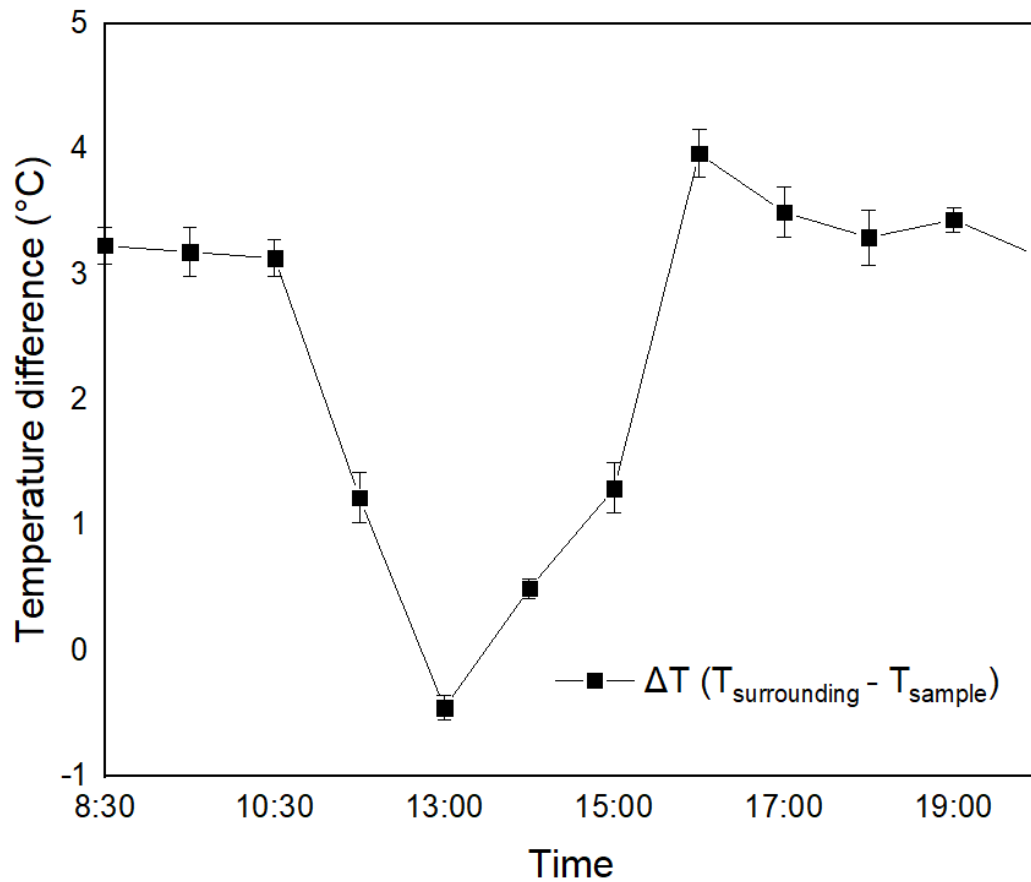
Figure 34. Outdoor measurement of the radiative cooler placed under direct sunlight.

The measurement was performed in Edmonton at ~70% humidity. The temperature variation

($T_{surrounding}$ - T_{sample}) between the sample and the surrounding was monitored during the day and

plotted in Figure 34. More information regarding experimental conditions can be found in

Appendix, Figure 59 and Figure 60 [123]. It shows that the maximum cooling temperature this sample reached was 3.97 °C below the surrounding temperature at 16:00. . This difference became -0.45 °C at 13:00 which suggests the cooling ability of the sample has been reduced due to a significant increase in solar radiation (P_{sun}). A resistive heater was placed below the sample to provide heat to keep the sample and ambient temperatures the same. The powers provided to the heater to match these two temperatures were monitored, which is also known as cooling power, and shown in Figure 35.
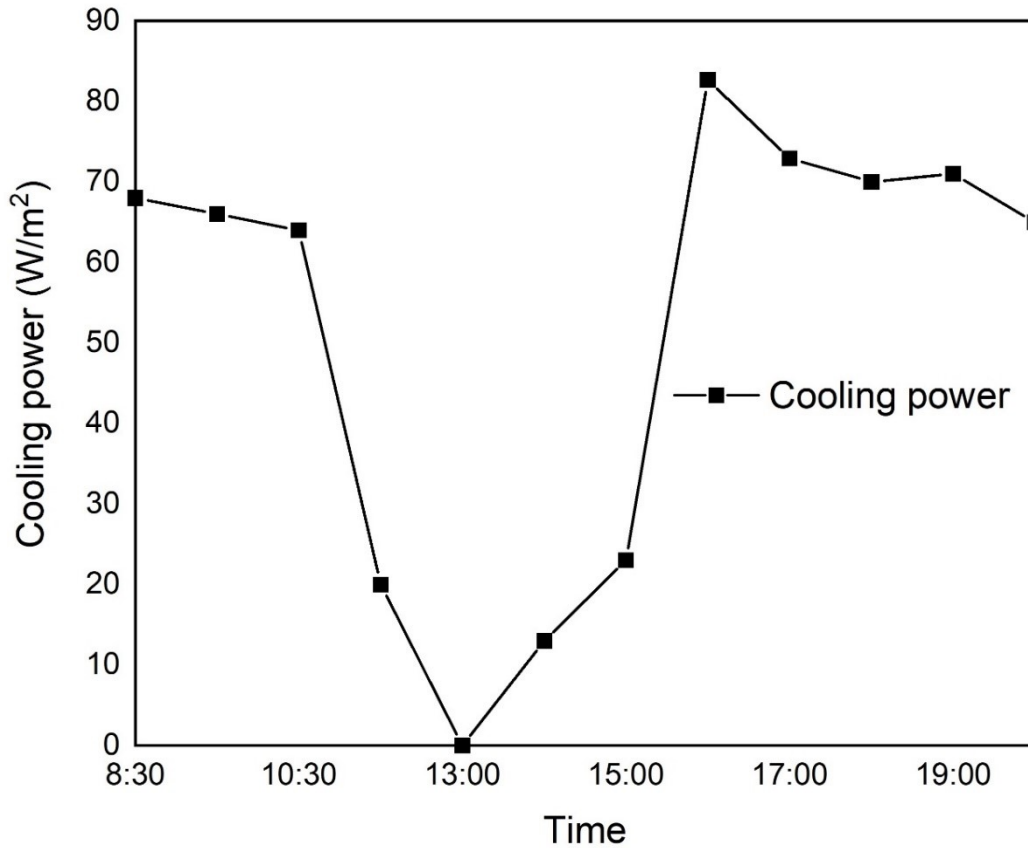
Figure 35. The experimental cooling power of the cellulose-upgraded sample.

This figure shows that the maximum cooling power provided by the sample was 82.66 W/m^2 at 16:00. On the other hand, the stagnation temperature achieved during the experiment for this sample was 3.97 °C, which is lower than the theoretical prediction of 6.82 °C. This is mainly due to higher non-radiative heat losses than predicted. We believe an improved experimental setup to lower non-radiative heat loss would have provided better results.

4.3.4.   *Application of cellulose-upgraded polymer in solar cell*

In this section, the effect of cellulose-upgraded polymer on the solar cell is presented. It is expected that the radiative cooling of solar cells can be achieved by attaching the cellulose-upgraded polymer film with the solar cell. Importantly, placing the cellulose-upgraded polymer film on top of the solar cell would also impact the amount of solar spectrum reaching the solar cells and hence influence its performance. It was found previously that when CNCs are mixed with PDMS, they can act as diffusers due to a combination of Rayleigh and Mie scatterings, with the length of CNCs varying between 100-200 nm and diameter varying between 10-20 nm [32]. Figure 36 shows the transmittance and haze (the percentage of total transmitted light that is diffusively scattered) of 1 wt.% and 2 wt.% CNCs samples. This figure shows the ability of CNCs to efficiently scatter light in the forward direction which increases with the increasing concentration of CNCs. More information about the diffusing properties of CNCs can be found elsewhere [124].
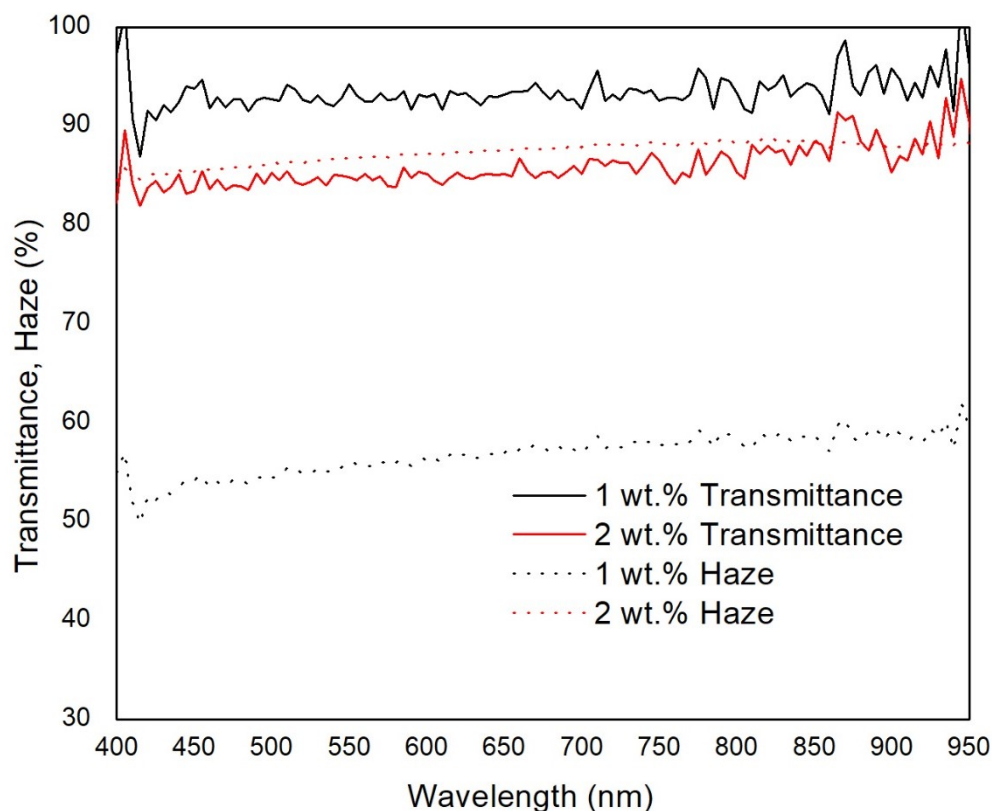
Figure 36. Transmittance and haze of 1 wt.% CNCs and 2 wt.% CNC as a function of wavelength.

A mini panel of size 3 x 3 cm consist of polycrystalline silicon solar cells was taken (Figure 37 inset), and cellulose-upgraded polymers were placed on top of it to study its effect. At first, we monitored the temperature of the panel under solar radiation throughout the day, which is shown in Figure 37. This graph shows the surrounding temperature, bare solar panel temperature, and temperature of the solar panel with CNC placed on top. It shows that the temperature of the solar panel that had CNC on top had a relatively lower temperature than a bare solar panel, indicating the cooling capability of CNC based radiative cooler. The reduction

in solar panel's operating temperature was relatively small due to higher non-radiative heat losses by the cellulose-upgraded polymer since it was kept in an open environment.
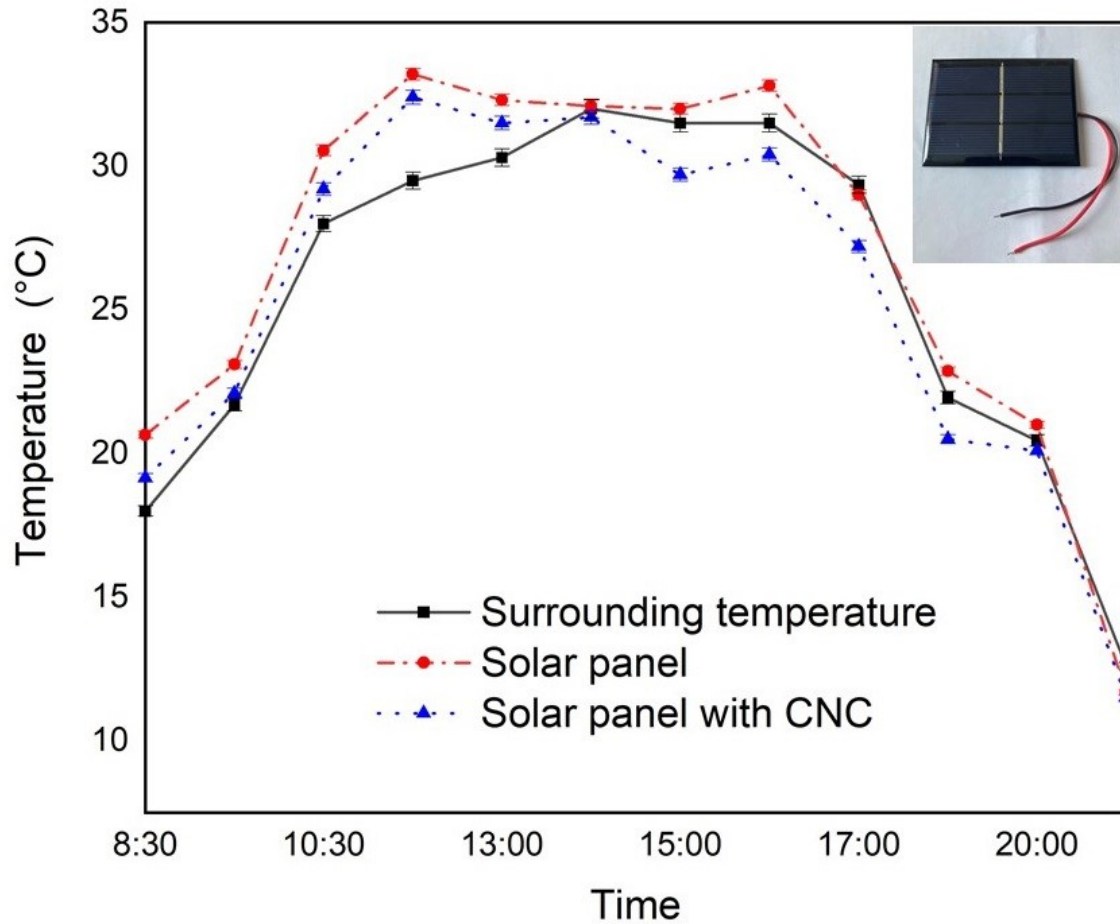
Figure 37. Effect of cellulose-upgraded polymer on solar panel temperature. Inset shows the solar panel that was used in this study.

After that, we conducted electrical characterization of the polycrystalline silicon solar cells of size 3 x 3 cm in an indoor setup where cellulose-upgraded polymer transfers heat with the surrounding environment instead of the cold universe through the sky. Since the surrounding environment has a temperature much higher than the universe, the cooling efficiency of the polymer might decrease. This approach was taken due to our inability to build an outdoor setup

but still provides a good insight into this polymer's ability to cool down. Figure 38 shows current-voltage characteristics of the solar cells under simulated AM1.5G solar spectrum with cellulose-upgraded polymers placed on top of the cell.
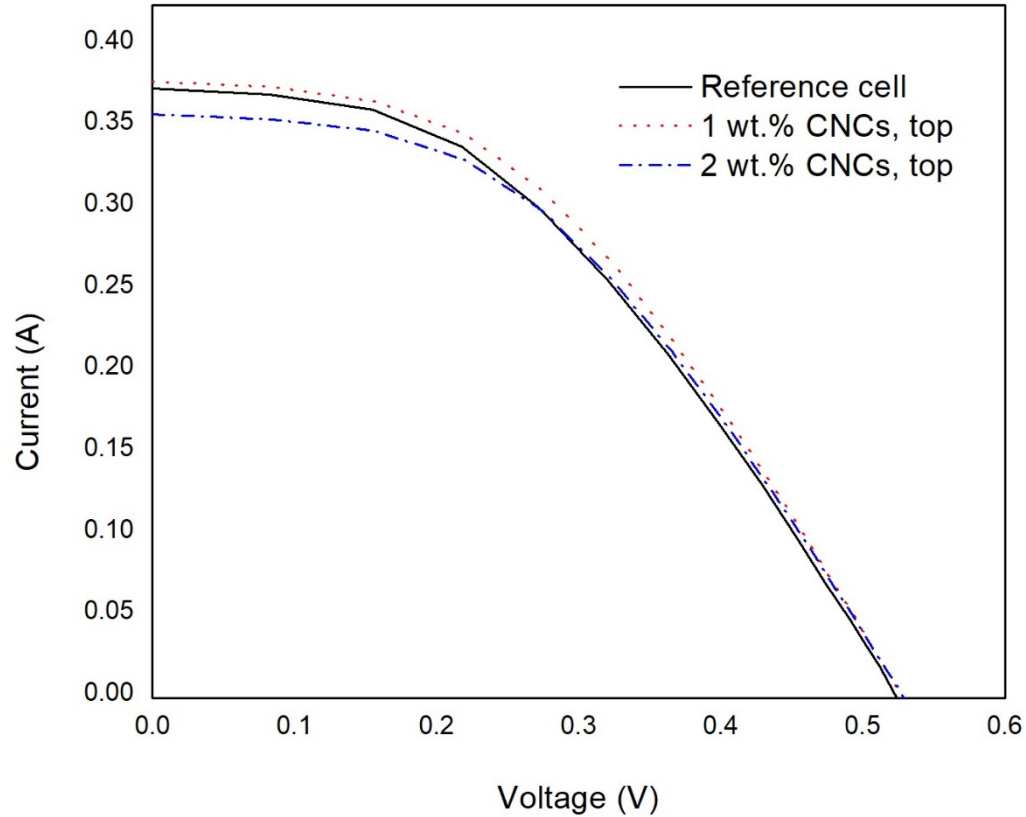
Figure 38. Current-voltage characterization of the solar cell under simulated AM1.5G solar spectrum.

With cellulose-upgrade polymers, alongside lower operating temperature, we observed a reduction in short circuit current and enhancement in open-circuit voltage. Higher temperature induces thermal carrier excitation which increases the short circuit current. At the same time, higher operating temperature increases the energy of electrons in the material and decreases

the bandgap which reduces the open-circuit voltage and fill factor. Though lower operating temperature would reduce short circuit current slightly, it would also reduce the energy of electrons and ensure higher open-circuit voltage and fill factor, providing higher output power. Now placing the sample on top of the cell would also induce light scattering, as predicted by Figure 8. Such scattering of light will increase the optical path length inside the cell and increase the short circuit current. Figure 38 shows an enhancement in short circuit current and open-circuit voltage after placing 1 wt.% CNCs sample on top of the cell which can be attributed to the combined effect of radiative cooling and light scattering by this sample. 2 wt.% CNCs sample was also studied and found to be reducing short circuit current significantly when placed on top of the cell which may be related to lower transmittance and a higher haze value of this sample that limits the performance of the cell.

Table 4 summarizes the performance of the solar cells with and without cellulose-upgraded polymers.

Table 4. Summary of results.

	Reference	1 wt.% CNCs, bottom	1 wt.% CNCs, top	2 wt.% CNCs, top
V_{oc} (V)	0.526±0.001	0.535±0.007	0.530±0.003	0.532±0.003
I_{sc} (A)	0.379±0.003	0.368±0.006	0.383±0.005	0.355±0.006
Fill Factor (%)	0.419±0.002	0.436±0.006	0.432±0.003	0.446±0.005
Efficiency (%)	8.217±0.059	8.462±0.082	8.634±0.054	8.299±0.029

4.4. Conclusion

In summary, a selective emitter composed of the cellulose-upgraded polymer has been proposed for radiative cooling application. It was found that adding cellulose into PDMS has improved the emission from the structure with emission peaks ~ 90%. Cooling temperatures and cooling powers of the sample were also measured, and higher cooling temperatures and cooling powers were achieved mostly during the early morning and late afternoon. The maximum cooling temperature was 3.97 °C below ambient temperature and the corresponding cooling power was around 82.66 W/m^2, which were recorded at 16:00. Although our developed structure's ability to radiation is limited by its property, the easy fabrication process makes it highly suitable for practical implementation. Additionally, as a proof of concept, this polymer was attached with a solar cell and found to reduce the operating temperature compared to a bare solar cell under solar radiation. Indoor electrical characterization showed an enhancement in open-circuit voltage, owing to an increased bandgap of the absorber material. CNCs were also found to forward scatter light which contributed towards the enhancement of short circuit current in the solar cell. Efficiency enhancement during indoor measurement was relatively small but larger enhancement is expected during outdoor measurement since cellulose-upgraded polymer would be able to transfer heat to the sky. Works are currently underway to prepare a complete setup to perform thorough electrical characterization outdoor. Though the long-term prospect of placing such a cooler on top of a solar cell needs to be investigated, still this study provides an excellent platform for future efforts to investigate new materials for radiative cooling and explore potential applications.

Chapter 5: Improving the light quality of white light-emitting diodes employing cellulose nanocrystal filled phosphors

5.1. Introduction

White light-emitting diodes (LEDs) are long-lasting and energy-efficient. As the future of solid-state lighting, LEDs are replacing incandescent light bulbs and compact fluorescent lamps (CFLs) in outdoor and indoor applications [125]. The most common approach to produce white LEDs is to use a blue LED chip and yellow phosphor [126]. In these phosphor-converted white LEDs, the short-wavelength (blue light) LED is used to excite the phosphor and down-convert higher energy short-wavelength photons to low energy long-wavelength photons and combine both types of photons to create a perceived white spectrum [127]. This technique has several advantages like simple fabrication, low cost, and high conversion efficiency compared to other techniques like using individual red, green and blue LEDs are used to generate white spectrum or using UV-LEDs to excite red, green, and blue phosphors [128].

The performance of white LEDs depends on different factors including luminous efficiency, color rendering index (CRI), and correlated color temperature (CCT) [129]. Luminous efficiency can be improved by various techniques such as nanostructured blue-chip, sapphire substrate with cone-shaped nanoparticle [130], GaN nanoparticles as phosphors, and GQDs as charge-transfer medium [131], and air voids between GaN nanopillars and the GaN layer [132,133]. Dual structure phosphor layer and textured phosphor structures were also found to

improve luminous efficiency [134,135]. In recent work, a series of Bi^{3+}, Zn^{2+}, La^{3+}, Eu^{3+} doped $Ca_3Ga_4O_9$ (CGO) phosphors were prepared for white LED application and found to have high luminous efficiency [136]. On the other hand, red phosphor technologies [137,138], multiple lateral quantum wells (QWs) [139,140] have been reported to enhance the CRI value of white LEDs. Carbon quantum dot (QD) based white LEDs were also reported recently that showed a CRI value of 91, the highest among rare-earth and inorganic semiconductor QDs based white LED [141].

Another important parameter that determines the performance of white LEDs is the uniformity of CCT which is the difference between high color temperature (a blueish type of white or cool white) and low color temperature (a yellowish type of white or warm white) at the various angles [142]. Non-uniform emission of white light can cause by the uneven angular distribution of CCT and can lead towards an unwanted phenomenon known as "yellow ring" [143]. Conformal phosphor structure can produce better uniformity of angular CCT by reducing the CCT deviation, but such structure has poor light extraction due to large light reflection [144]. Different types of remote phosphor packaging were proposed and, factors such as surface curvature of the phosphors and location of the phosphors were studied to improve the color homogeneity of the white LEDs [145–147]. Other methods such as improved silicon lens design [148] and patterned sapphire substrate [149] were studied to improve the homogeneity of the white LEDs. TiO_2 nanoparticles were incorporated into the packaging materials to resemble a graded-refractive-index multilayer structure.[150] By modifying the surface of TiO_2 nanoparticles and dispersibility CCT uniformity was improved in another work [151]. In another work, blue laser irradiation was used to control the spatial phosphor particle spatial distribution to improve CCT uniformity [152]. Red phosphor thin films (PTFs) with different

MgO nanoparticle concentrations were also used that improved the CCT by 8.81% [153]. In such a device, light can be scattered by nanoparticles which in turn could strongly influence the optical path and change the CCT deviation in white LEDs [154]. More recently, boron nitride nanoparticles were studied for reflection enhancement of an inverted packaging structure [155]. However, some of these methods enhance the uniformity of CCT at the cost of luminous efficiency [156,157] and thus it is important to find a balance between luminous efficiency and CCT uniformity that could help white LEDs to become the primary solid-state light source.

In this study, cellulose nanocrystals (CNCs), a biopolymer derived from wood, were employed to improve the performance of white LEDs. CNCs have superior light scattering capability and are promising candidates for optical diffusers [32,158]. Filling CNCs into the phosphor layer enabled better utilization of blue light which increased the luminous flux. Furthermore, such scattering capability of CNCs also helped to reduce angle dependent CCT deviation.

5.2. Experiment

Figure 39 (a) and Figure 39 (b) illustrate the device structures of conventional phosphor-converted white LEDs and our LEDs with CNC-filled phosphors, and Figure 39 (c) shows the top view (photo) of our LED device [159]. A blue LED chip (Shenzhen Getian Opto-Electronics Co., Ltd, 3030 blue SMD LED) with an emission peak between 460-470 nm was outsourced with operating voltage 2.4-3 V. Then CNCs were uniformly mixed with yttrium aluminum garnet (YAG) phosphors, and the PDMS (Dow Corning, Sylgard 184 kit) and dispensed in the package. The reference sample only had a uniform mixture of phosphor and PDMS. To investigate the effect of CNCs on the improvement of the luminous flux and CCT

of our LEDs, different concentrations of the CNCs were added to the phosphor and PDMS mixture. The size of the phosphors was around 4 µm, and individual CNC and CNC clusters were sized between 100-200 nm and 1-3 µm respectively. Figure 40 shows the experimental setup that was used to characterize the LED. All light from the LED was captured using an integrating sphere which was connected to a spectrometer (Ocean Optics, FLAME-S-VIS-NIR-ES) by an optical fiber. The detector (spectrometer) was connected to a workstation where the data was recorded and analyzed.
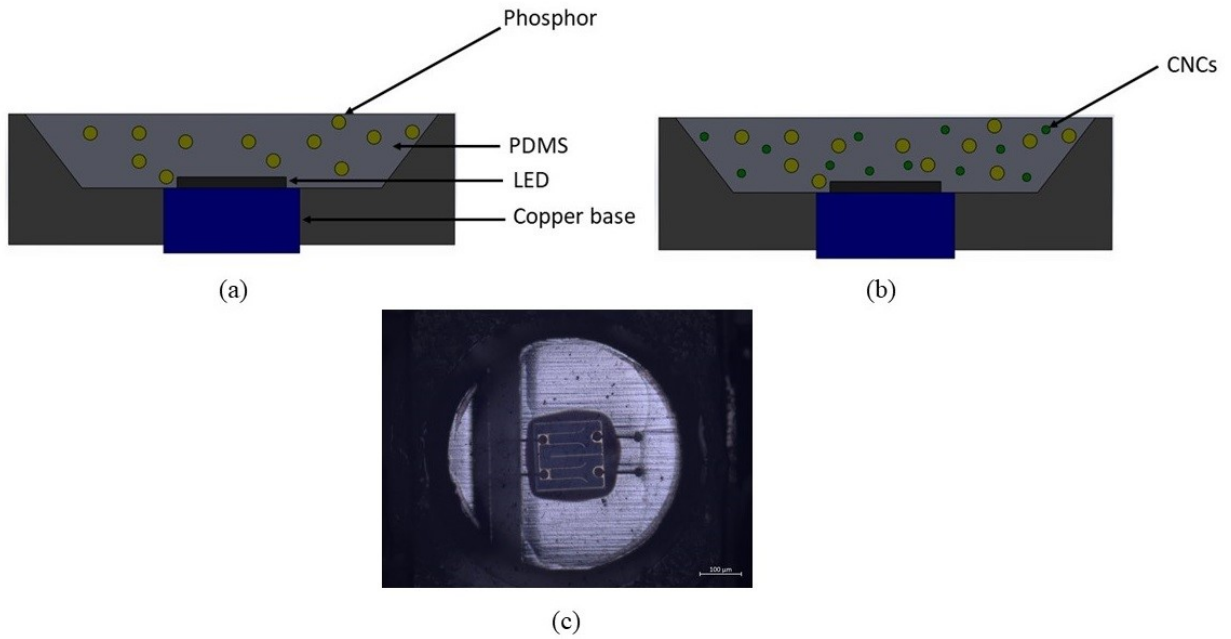
Figure 39. (a) The schematic cross-sectional view of conventional structure (b) CNCs-embedded structure (c) Top view of the LED chip.
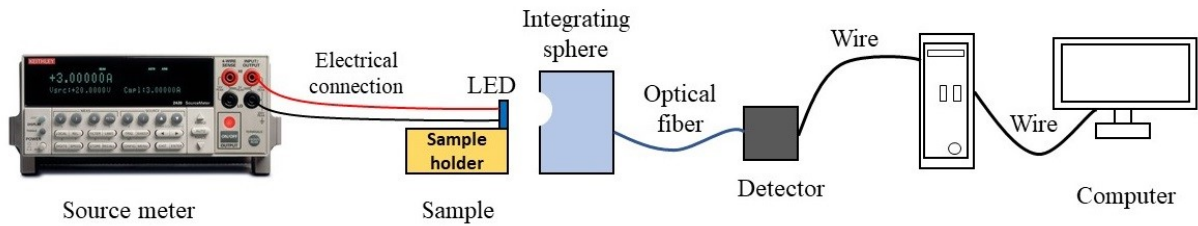
Figure 40. Experimental setup to characterize the performance of LEDs.

5.3. Results and discussion

(a)   (b)
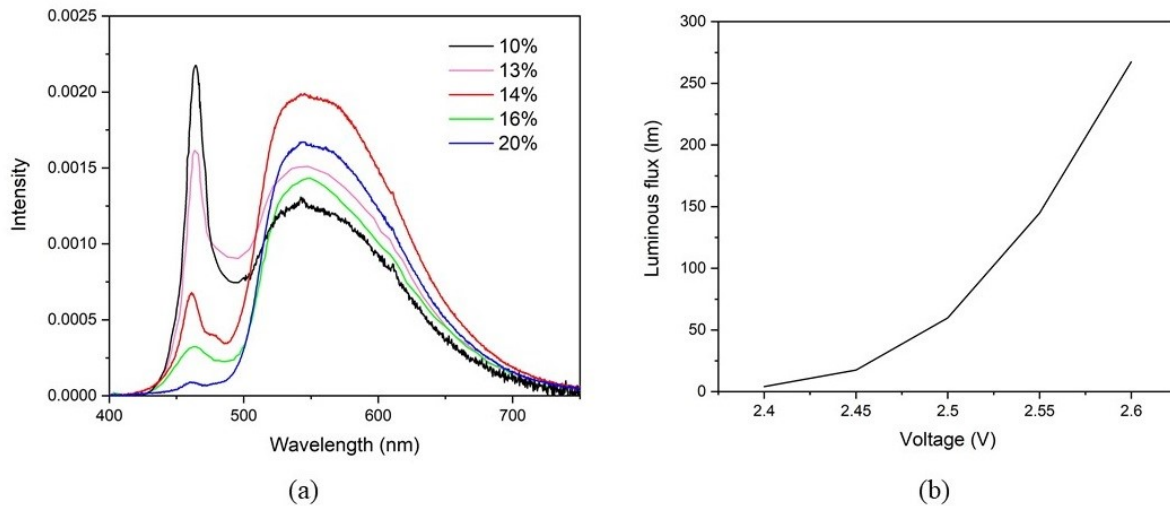
Figure 41. Effect of (a) phosphor concentration and (b) applied voltage on the performance of LED.

The influence of phosphor concentration on the performance of white LEDs was first investigated to find an appropriate phosphor concentration for studying white LEDs using CNCs filled phosphors. Figure 41 (a) shows the emission spectra of white LED structures with different concentrations of phosphor. Phosphor concentration can change blue and yellow light

intensities in the emission spectra and based on the result 14 wt.% phosphors were chosen as the luminous flux was the highest at this concentration. More information about this can be found in Appendix, Figure 61 and Figure 62. Figure 41 (b) shows the effect of applied voltage on a white LED with 14 wt.% phosphors ranging from 2.4 to 2.6 V. It shows that with increased voltage luminous flux also increased. For the remainder of this work, all the samples were prepared with 14 wt.% phosphors concentration and characterized at 2.6 V.
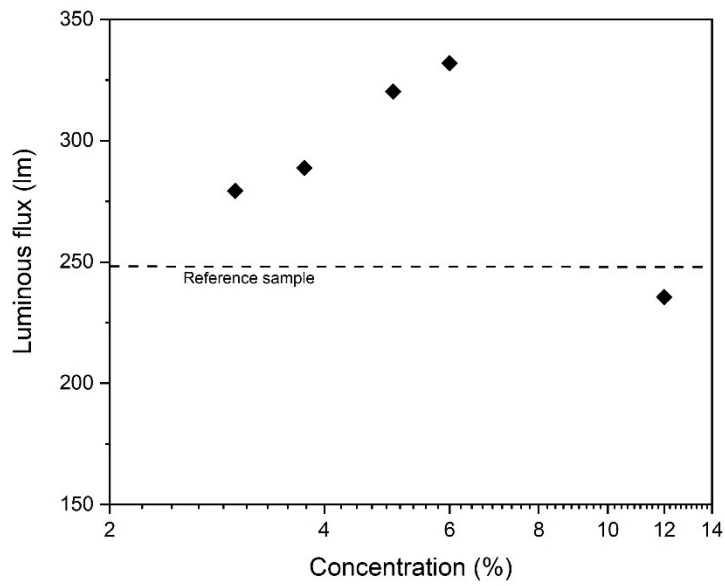
(a)
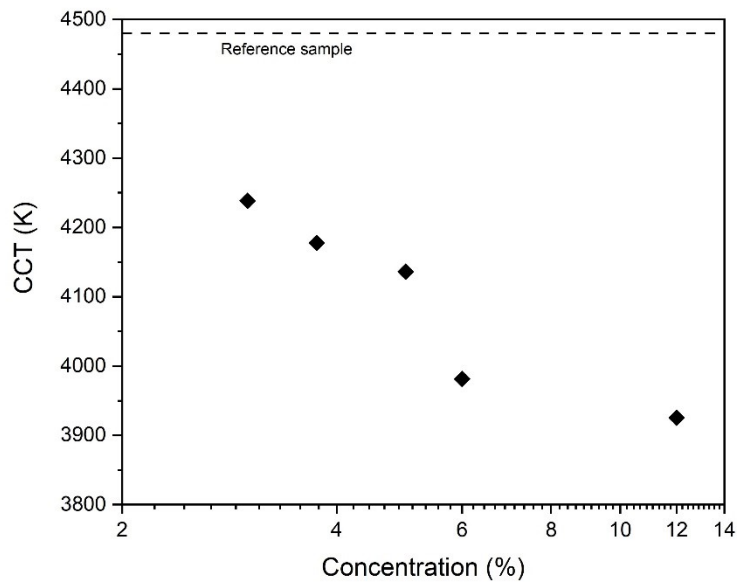
(b)

Figure 42. Change in (a) luminous flux and (b) correlated color temperature with different concentrations of CNCs.

After that, different concentrations of CNCs were mixed with phosphor and more information about mixing phosphor and CNCs can be found in Figure 63 in Appendix. Figure 42 (a) shows the luminous flux of white LEDs with different concentrations of CNCs. The luminous flux of the reference sample (phosphor only) was around 247 lumens and it started increasing with increasing concentration of CNCs and an increase of around 33% was recorded with 6 wt.% CNCs compared to the reference sample. CNCs-embedded white LED structures had higher yellow-light intensities compared to the reference sample due to improved conversion of blue photons which resulted in a higher luminous flux and efficiency. These CNCs can scatter light which has been thoroughly analyzed and discussed in our previous work [32,124,127,160]. This scattering effect of CNCs increased the luminous flux by increasing the optical path length of blue light which led to the higher possibility of exciting yellow phosphor and generate yellow photons. Though with the increasing concentration of CNCs, transmission through the CNCs will start to decrease. Luminous flux of the white LED structure was found to be around 235 lumens at 12 wt.% CNCs concentration (not shown in the figure) which is due to the light trapping and absorption phenomenon between CNCs and phosphor materials. Figure 42 (b) shows the CCTs with different concentrations of CNCs. The CCT of the reference sample was around 4470 K and it decreased with increasing CNCs concentration due to the higher yellow conversion ratio. Figure 43 shows the emission spectra of the reference and CNCs-embedded white LED structures. Due to increased scattering, blue light had a higher likelihood to excite yellow phosphors and this increased utilization rate of blue light increased the output of yellow light, resulting in the enhancement of luminous flux.

To further understand the scattering effect of the CNCs on the CCT and luminous flux, angle-dependent CCTs of the white LED structures containing different concentrations of CNCs

were measured and showed in Figure 44 (a). Angle-dependent CCTs showed better uniformity with the addition of CNCs which indicates increasing CNCs yielded a stronger scattering effect. The uniformity of the CCTs was determined by subtracting maximum CCT and minimum CCT. For the reference sample, it was found to be around 173.45 K which decreased with increasing concentration of CNCs and reached a value of around 59 K for 6 wt.% CNCs as showed in Figure 44 (b). The reference sample and 6 wt.% CNCs sample showed CCTs of approximately 4220 K and 3985 K respectively, at 0º viewing angle which implies a reduction of blue light due to the addition of CNCs with phosphor. Figure 44 (b) also shows that increasing concentration of CNCs will increase the figure of merit (FOM) which is defined as [142]:

$$FOM = \frac{Lumen_{CNCs} - Lumen_{No\ CNCs}}{\Delta CCT}$$
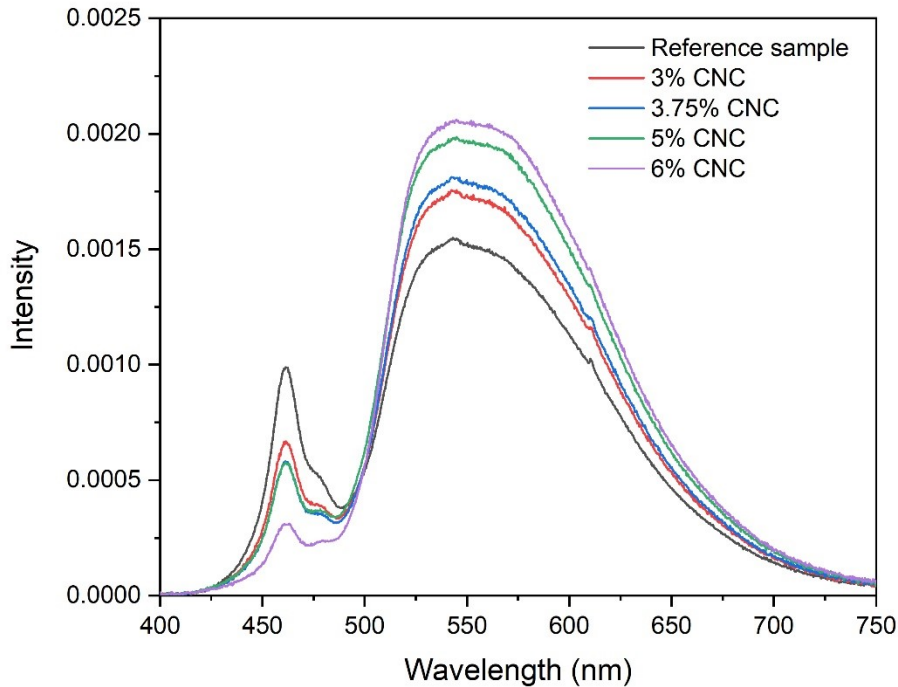
Figure 43. The emission spectra of CNCs-embedded and reference (phosphor only) samples.

(a)

(b)
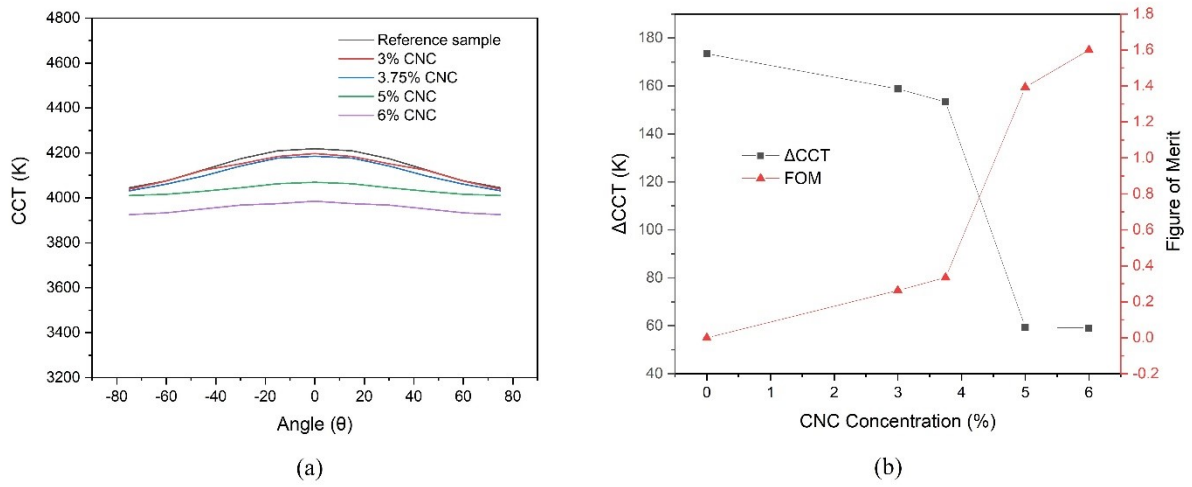
Figure 44. (a) Angular-dependent correlated color temperature of CNCs-embedded white LED structures (b) Deviation of correlated color temperature and figure of merit of different concentrations of CNCs-embedded white LED structures.
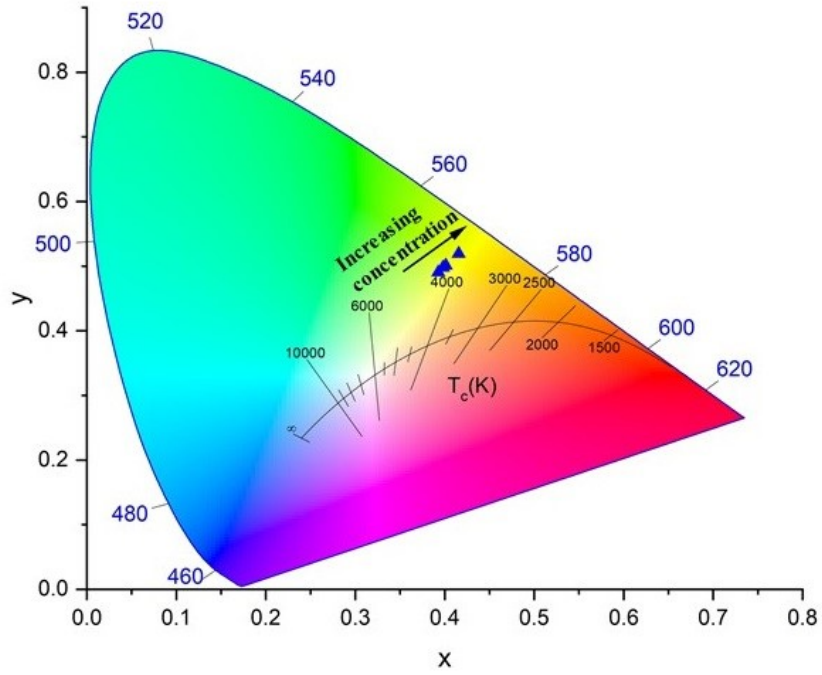
(a)
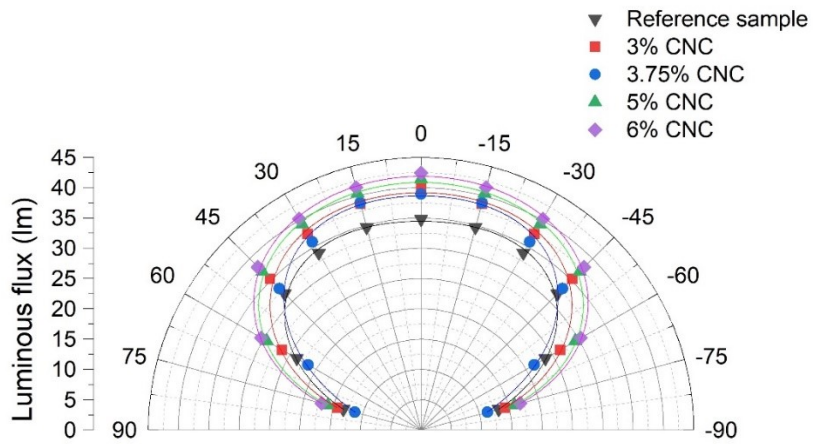
(b)

Figure 45. (a) Chromaticity coordinates and (b) relative lumen of LED with different concentrations of CNCs.

In the end, the color qualities of the CNCs-embedded white LED structures were evaluated by measuring the chromaticity coordinates, which is a widely adopted standard. The chromaticity coordinates of the CNCs-embedded white LED structures are shown in Figure 45 (a). As the CNCs concentration was increased, there was a gradual shift of the chromaticity coordinates to the yellow region which means that the intensity of the yellow light was increasing and thus reducing the CCTs. The angular-dependent emission intensity was also studied and shown in Figure 45 (b). It shows that CNCs-embedded white LED structures can exhibit superior performance and produce high-quality white light at different viewing angles.

5.4. Simulation

In this section, a simulation study is presented to study the effect of two different types of CNC-phosphor structures for white LED applications. Zemax ray tracing software was used for this work. Figure 46 (a) and Figure 46 (b) show the two different LED structures without any lens that were studied to understand the effect of CNCs. The size of the LED chip was 1x1 mm^2 and had five layers: p-GaN, a multi-quantum well (MQW), n-GaN, sapphire substrate, and metal alloy film. The thicknesses of the layers were set at 150 nm, 100 nm, 4 μm, 140 μm, and 0.1 μm, respectively. Refractive indices and absorption coefficient values were taken from elsewhere [161,162]. The dispensing-coated phosphor-silicone layer was constructed as a spherical cap. The size of phosphor was 4 μm and its optical properties were taken from elsewhere [161]. To represent blue and yellow light, two specific wavelengths, 454 nm, and 569 nm were chosen where the blue light was assumed to be radiated from the top surface of the chip with Lambertian distribution [163]. This blue light was absorbed and re-emitted into yellow light from the phosphor-PDMS layer. A hemisphere detector was placed on top of this

structure to cover -70º to 70º viewing angles. After that, CNCs were also constructed using a precise optical model described in our previous work [124,127]. The size of these CNCs was set at 4 μm and concentration was tuned at 6 wt.%. The scattering coefficient was obtained by Mie theory which depends on the distribution of CNCs. A similar model with the lens was simulated in our previous work [127] and compared with published data [161] that verified the accuracy of this particular model. Two different kinds of structures were investigated: 1) two layers of CNCs and phosphors as showed in Figure 46 (a), and 2) a single layer made of CNC filled phosphors as showed in Figure 46 (b).
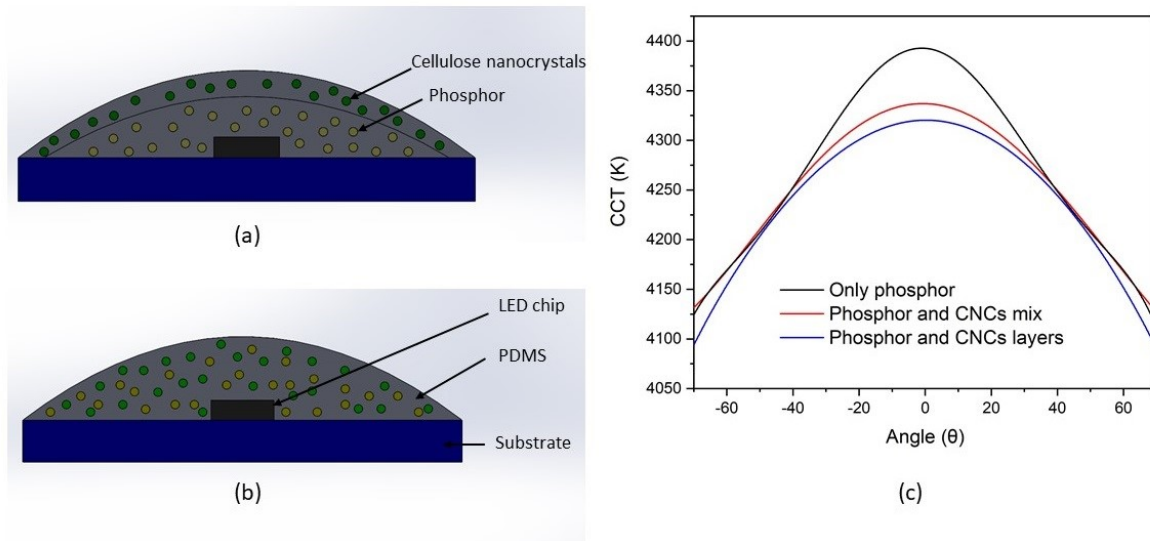
Figure 46. (a) White LED package with separate CNC and phosphor layers (b) white LED package with a single CNC filled phosphor layer (c) angular-dependent correlated color temperature of different LED samples with 6 wt.% CNCs concentration.

Figure 46 (c) shows the angular-dependent CCT variation for different white LED structures. For the phosphor-only sample, variation in CCT was 270 K. It was reduced to 224 K for the

sample that had one layer of CNCs and one layer of phosphors. This further reduced to 200 K for the sample that had a single layer with CNC-filled phosphors. This figure also shows that samples with CNCs had lower CCT at 0° viewing angle than the phosphor-only sample, which verified the scattering ability of CNCs that enabled better utilization of blue light. As discussed above, this simulation study showed our approach of filling CNCs into the phosphor layer enabled better utilization of blue light, which increased the average CCT while maintained low CCT deviation for white LEDs. In addition to the improvement in CCT, CNCs also helped enhance luminous intensity and flux for white LEDs. The sample with a single CNC filled phosphor layer showed 39.6% enhancement of luminous flux (126.16 lumens), which is the integral of angular luminous intensity over the hemisphere detection in simulation, and the sample with separate CNC and phosphor layers showed 27.3% enhancement of luminous flux (115 lumens) compared to the sample with phosphor only (90.34 lumens). This study showed that mixing the CNCs and phosphors would yield better results because scattered blue light will have higher chances of getting reabsorbed by phosphors which would emit yellow light and reduce CCT deviation.

5.5. Conclusion

In conclusion, the effect of CNCs to improve the light quality of white LEDs was investigated. It was found that adding 3 wt.% CNCs with phosphor increased the luminous flux by around 11% and it increased to around 33% for 6 wt.% of CNCs. This enhancement in light output was due to the scattering ability of CNCs that enabled better utilization of the blue light. This also helped to increase the uniformity of angle-dependent correlated color temperature and for 6 wt.% CNCs concentration, uniformity improved to 59 K compared to 173.45 K of the

reference sample. The chromaticity coordinates showed a shift of CCT towards the yellow region that also verified the scattering ability of CNCs. Lumen output was also increased between -75º to 75º viewing angles. A simulation model was also developed to compare the performance of two different kinds of CNC-phosphor structures, and it was found that mixing CNCs and phosphors would yield better CCT and increase light output. In this work, YAG phosphor was chosen due to its superior thermal stability and brightness and though other phosphors can be chosen based on requirements it is important to make sure about its thermal stability as otherwise, the luminescence of phosphor and quality of light from white LED will decrease [164]. PDMS type and mixing technique can also change the optical properties [165,166] and even though the mechanical properties of CNCs and PDMS mixture have already been studied which did not show significant degradation [167], further investigation is needed, first to understand the effect of PDMS on the light quality of white LED and second to find out the change in optical properties of such film over time. Going forward, this study provides an excellent platform for future efforts to investigate the potential of CNCs for application in solid-state lighting.

Chapter 6: Conclusions and future works

6.1. Summary of accomplishments and contributions

In recent years, there has been a great increase in demand for polymers, and petroleum-based polymers have found significant market space even after significant concern about their role in global warming. One of the most commonly used petroleum-based polymers is PMMA which is not biodegradable and can produce toxic by-products if not properly recycled. That is why biopolymers, which are derived from living organisms, are gaining attention as they are biodegradable by different aerobic and non-aerobic procedures in nature, sediments, or landfills. The objective of this thesis was to leverage the excellent properties of these biopolymers for photonics application which was accomplished by taking advantage of the theory, and experimental design, fabrication, and characterization.

At first, CNCs were utilized as waveguide material in a luminescent solar concentrator, and performance was compared with APE, a petroleum-based polymer. It was found that when the device size was small, the performance of CNCs as a waveguide is better than APE. With increasing device size, performance dropped for both these types of waveguides though it was much higher for CNCs-based waveguides. A recyclability study was also performed, and it was found that CNCs-based waveguide could be reused with little to no performance drop whereas APE-based waveguide was not able to do so. Even though further modification is required to reduce the scattering for large devices, the results looked promising and an excellent reference for future effort.

Later, lignin and CNCs were both studied for radiative cooling application by utilizing the unique property that enables them to transfer heat through the earth's atmosphere to the universe. This allows them to achieve a cooling temperature lower than the surrounding. At first, lignin was investigated which had high solar absorption that required to modify the radiative cooling structure. Daytime study with this modified structure showed high cooling power and lower sample temperature than the surrounding. This radiative cooler was attached to the backside of a solar cell and it showed an enhancement as the radiative cooler was able to lower the operating temperature of the cell. But due to lignin's concern over high solar absorption that required some modification, CNCs were also explored since it has a high solar reflection. CNCs based radiative cooler also showed high cooling power and managed to lower the temperature of the sample below the surrounding temperature. Moreover, once placed on top of a solar panel, high output was recorded which might be due to the combined effect of scattering and radiative cooling.

Finally, the scattering property of CNCs was leveraged for improving light quality in white LEDs. The most common way of producing white LED is to use phosphor and blue LED chip where phosphor would absorb some on of the blue light and emit yellow light and combination if this two would produce white light. Scattering of light by CNCs increased the chances of blue light absorption by the phosphor and produced better quality light. The uniformity of the color temperature was improved, and enhanced luminous flux was recorded from the LEDs containing CNCs as a scattering medium.

Overall, this thesis utilized biopolymers for different applications in photonics. Though further studies would need to be conducted, results were encouraging and showed excellent prospect of biopolymers for photonics.

6.2. Future outlook

6.2.1. Cellulose nanocrystals size optimization and chiral nematic structure formation for LSC device

During this research, it was found that CNCs can be used as matrix material in luminescent solar concentrators and performance was better compared to APE in small devices. When the size was increased, performance dropped sharply which we believe due to enhance scattering of light by CNCs. We expect this can be tackled by optimizing the size of CNCs. A thorough study needs to be conducted to understand the relation between the size of CNCs and optical properties and optimize it for luminescent solar concentration (LSC) application. Another way the performance of LSC can be improved by placing CNCs-based reflective liquid crystal films underneath the LSC device to improve light trapping. CNCs can self-assemble into periodic optical planes serving as Bragg diffractors [168]. The reflection peak of this kind of film can be tuned as shown in Figure 47. Now based on the property of organic dyes/quantum dots used in the LSC device, CNCs-based liquid crystal film can be optimized to have a high reflection at the emission peak of organic dyes/quantum dots which would reduce escape cone losses in the LSC device.
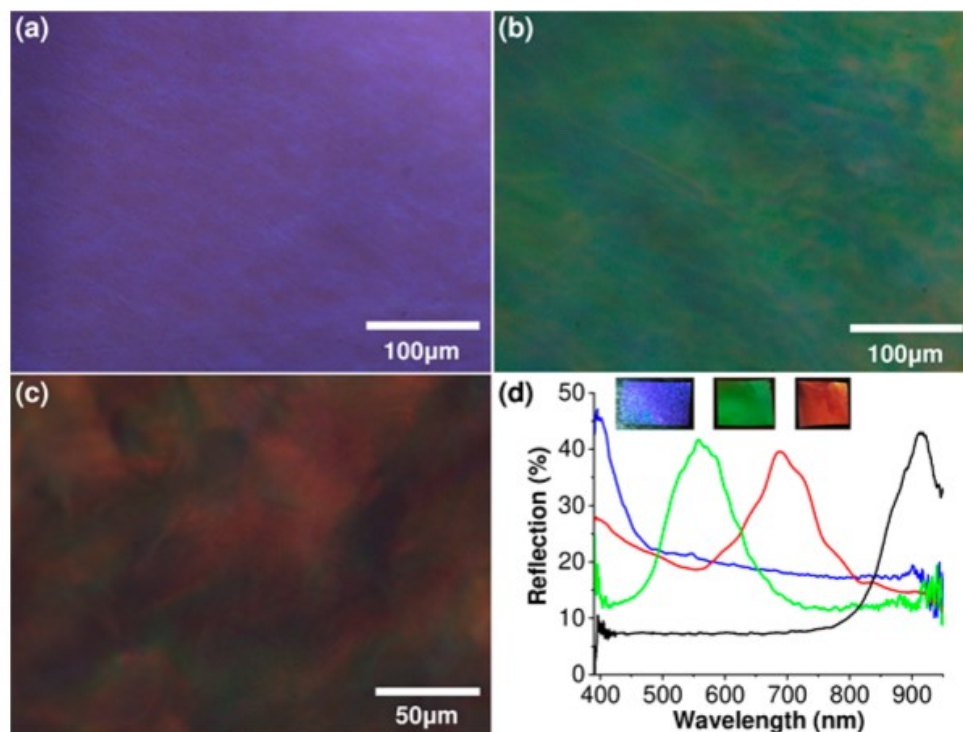
Figure 47. Reflective optical micrographs with natural light incident upon CNC-based reflective films with reflection peaks centered at (a) 400 nm (b) 557 nm, and (c) 688 nm prepared with organosilica loading ranging from 21.3 to 32.6 wt % in the presence of a static 2000G magnetic field directed parallel to the surface normal. In (d) these films' reflection spectrum is plotted in their predominant reflective color. Reprinted (adapted) with permission from [169]. Copyright © 2018 American Chemical Society.

6.2.2. Modification of lignin for Radiative cooling application

During the radiative cooling study, it was found that even though lignin has excellent emissivity property for radiative cooling applications, its use for daytime radiative cooling could be limited as it absorbs solar radiation. In our work, a simple and cost-effective solution was implemented by using Al foil but for large-scale implementation, such a solution is not

feasible. Interestingly, it was found that the color of lignin can be controlled either by optimizing the process [110] or by choosing an appropriate source [111]. Figure 48 shows a comparison of lignin produced from different sources for sunscreen application. Such optical property would be beneficial for lignin's application in radiative cooling as it would reduce the absorption of solar radiation and at the same time, there may not be any necessity to use a reflective top layer. A thorough study of lignin from different sources showing such light color would increase the potential of lignin for large-scale implementation.
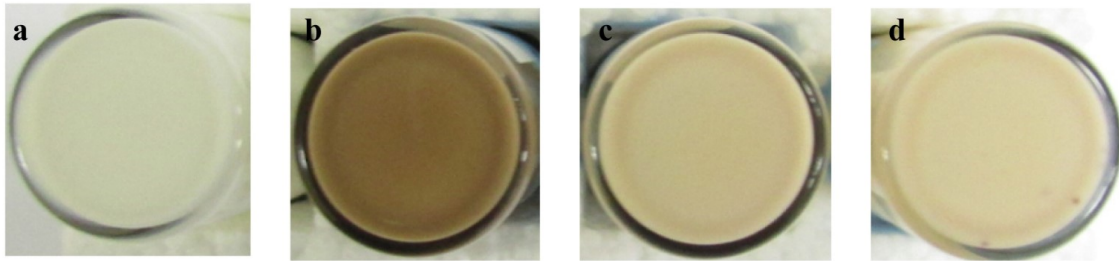
Figure 48. Photographs of the sunscreen (a) without lignin and with 1 wt. % lignin added [(b) OL, (c) MWL-M, and (d) MWL-P] [111]. Copyright Elsevier, license number: 5010541384617.

6.2.3. *Application of cellulose-based film for other types of photovoltaic and light emitting diodes*

In this work, the proposed cellulose-based film was used as a separate layer and its radiative cooling property was used to reduce the operating temperature of a silicon-based solar cell. This kind of film can be utilized easily for other types of solar cells since it only requires a simple lamination process. Especially in the case of solar cells with glass substrate as a top

layer, this cellulose-based film can be utilized as a top layer that would promote light scattering and improve solar absorption by the absorber material and at the same time will reduce the operating temperature utilizing its radiative cooling property.

This cellulose-based film can also be utilized to enhance the light extraction from LED devices with high refractive values such as QDs or perovskite-based LEDs where light trapping is a major bottleneck. Moreover, a previous simulation study has found to improve the output of LED devices by having a layer of CNC film on the outer side of the lens [127]. As such, a study can be conducted to see the effect of cellulose-based film as an outer layer on top of the lens and compare its performance with our work where the cellulose-based film was investigated as an internal layer by placing it on the LED chip.

Reference

[1]   N. Hernández, R.C. Williams, E.W. Cochran, The battle for the "green" polymer. Different approaches for biopolymer synthesis: bioadvantaged vs. bioreplacement, Org. Biomol. Chem. 12 (2014) 2834–2849. https://doi.org/10.1039/C3OB42339E.

[2]   N.R. Nair, V.C. Sekhar, K.M. Nampoothiri, A. Pandey, Biodegradation of Biopolymers, Curr. Dev. Biotechnol. Bioeng. (2017) 739–755. https://doi.org/10.1016/B978-0-444-63662-1.00032-4.

[3]   D.W. Laist, Impacts of Marine Debris: Entanglement of Marine Life in Marine Debris Including a Comprehensive List of Species with Entanglement and Ingestion Records, in: Springer, New York, NY, 1997: pp. 99–139. https://doi.org/10.1007/978-1-4613-8486-1_10.

[4]   K.D. Hanni, P. Pyle, Entanglement of Pinnipeds in Synthetic Materials at South-east Farallon Island, California, 1976–1998, Mar. Pollut. Bull. 40 (2000) 1076–1081. https://doi.org/10.1016/S0025-326X(00)00050-3.

[5]   B. Page, J. McKenzie, R. McIntosh, A. Baylis, A. Morrissey, N. Calvert, T. Haase, M. Berris, D. Dowie, P.D. Shaughnessy, S.D. Goldsworthy, Entanglement of Australian sea lions and New Zealand fur seals in lost fishing gear and other marine debris before and after Government and industry attempts to reduce the problem, Mar. Pollut. Bull. 49 (2004) 33–42. https://doi.org/10.1016/J.MARPOLBUL.2004.01.006.

[6]   P.G. Ryan, A.D. Connell, B.D. Gardner, Plastic ingestion and PCBs in seabirds: Is there a relationship?, Mar. Pollut. Bull. 19 (1988) 174–176. https://doi.org/10.1016/0025-

326X(88)90674-1.

[7]   C. Eriksson, H. Burton, Origins and Biological Accumulation of Small Plastic Particles in Fur Seals from Macquarie Island, AMBIO A J. Hum. Environ. 32 (2003) 380–384. https://doi.org/10.1579/0044-7447-32.6.380.

[8]   Plasticexpert, (n.d.). https://www.plasticexpert.co.uk/plastic-recycling/pmma-acrylic-recycling/.

[9]   N. Reddy, Y. Yang, Potential of plant proteins for medical applications, Trends Biotechnol. 29 (2011) 490–498. https://doi.org/10.1016/J.TIBTECH.2011.05.003.

[10]   J.C. Middleton, A.J. Tipton, Synthetic biodegradable polymers as orthopedic devices, Biomaterials. 21 (2000) 2335–2346. https://doi.org/10.1016/S0142-9612(00)00101-0.

[11]   K. Van de Velde, P. Kiekens, Biopolymers: overview of several properties and consequences on their applications, Polym. Test. 21 (2002) 433–442. https://doi.org/10.1016/S0142-9418(01)00107-6.

[12]   M. Ekiert, A. Młyniec, T. Uhl, Diagnostyka czasopismo naukowe, [s.n.], 2017. http://www.diagnostyka.net.pl/The-influence-of-degradation-on-the-viscosity-and-molecular-mass-of-poly-lactide,81489,0,2.html (accessed December 14, 2019).

[13]   M. Niaounakis, Biopolymers reuse, recycling, and disposal, William Andrew, 2013.

[14]   Wood Energy, (n.d.). http://www.fao.org/forestry/energy/en/ (accessed December 2, 2019).

[15]   R.M. Rowell, R. Pettersen, M.A. Tshabalala, Chapter 3 Cell Wall Chemistry, Inhandb. Wood Chem. Wood Compos. 2nd Ed. Chapter 3. Pp. 33-72. 2013. 3 (2012) 33–72. https://www.fs.usda.gov/treesearch/pubs/42245 (accessed December 3, 2019).

[16] Composition and Structure of Wood Cells, in: For. Prod. Wood Sci. An Introd., Wiley-Blackwell, Oxford, UK, 2011: pp. 45–63. https://doi.org/10.1002/9780470960035.ch3.

[17] H. V. Lee, S.B.A. Hamid, S.K. Zain, Conversion of lignocellulosic biomass to nanocellulose: Structure and chemical process, Sci. World J. (2014) 1–20. https://doi.org/10.1155/2014/631013.

[18] Z.-Y. Sun, Y.-Q. Tang, T. Iwanaga, T. Sho, K. Kida, Production of fuel ethanol from bamboo by concentrated sulfuric acid hydrolysis followed by continuous ethanol fermentation, Bioresour. Technol. 102 (2011) 10929–10935. https://doi.org/10.1016/J.BIORTECH.2011.09.071.

[19] Z. Zhang, I.M. O'Hara, W.O.S. Doherty, Pretreatment of sugarcane bagasse by acid-catalysed process in aqueous ionic liquid solutions, Bioresour. Technol. 120 (2012) 149–156. https://doi.org/10.1016/J.BIORTECH.2012.06.035.

[20] C. Li, B. Knierim, C. Manisseri, R. Arora, H. V. Scheller, M. Auer, K.P. Vogel, B.A. Simmons, S. Singh, Comparison of dilute acid and ionic liquid pretreatment of switchgrass: Biomass recalcitrance, delignification and enzymatic saccharification, Bioresour. Technol. 101 (2010) 4900–4906. https://doi.org/10.1016/J.BIORTECH.2009.10.066.

[21] S.T. Moe, K.K. Janga, T. Hertzberg, M.-B. Hägg, K. Øyaas, N. Dyrset, Saccharification of Lignocellulosic Biomass for Biofuel and Biorefinery Applications – A Renaissance for the Concentrated Acid Hydrolysis?, Energy Procedia. 20 (2012) 50–58. https://doi.org/10.1016/J.EGYPRO.2012.03.007.

[22] R. Willstätter, L. Zechmeister, Zur Kenntnis der Hydrolyse von Cellulose I, Berichte Der Dtsch. Chem. Gesellschaft. 46 (1913) 2401–2412.

https://doi.org/10.1002/cber.191304602174.

[23] J.C. Irvine, E.L. Hirst, LXIV.—The constitution of polysaccharides. Part VI. The molecular structure of cotton cellulose, J. Chem. Soc., Trans. 123 (1923) 518–532. https://doi.org/10.1039/CT9232300518.

[24] S. Dumitriu, Polysaccharides : structural diversity and functional versatility, Marcel Dekker, 2005. https://www.crcpress.com/Polysaccharides-Structural-Diversity-and-Functional-Versatility-Second/Dumitriu/p/book/9780824754808 (accessed December 3, 2019).

[25] M.C. Jarvis, Structure and properties of pectin gels in plant cell walls., Plant, Cell Environ. 7 (1984) 153–164. https://doi.org/10.1111/1365-3040.ep11614586.

[26] O. (Ed. . et al. Olatunji, Natural Polymers Industry Techniques and Applications, 2015. https://www.springer.com/gp/book/9783319264127.

[27] Y. Pu, M. Kosa, U.C. Kalluri, G.A. Tuskan, A.J. Ragauskas, Challenges of the utilization of wood polymers: how can they be overcome?, Appl. Microbiol. Biotechnol. 91 (2011) 1525–1536. https://doi.org/10.1007/s00253-011-3350-z.

[28] S.A. Wainwright, Mechanical design in organisms, Princeton University Pr, 1982. https://books.google.ca/books/about/Mechanical_Design_in_Organisms.html?id=7ZJvm_EPjBEC&redir_esc=y (accessed December 3, 2019).

[29] E. Sjöström, Wood chemistry : fundamentals and applications, n.d.

[30] Lignin, (n.d.). http://polymerdatabase.com/polymer classes/Lignin type.html (accessed December 16, 2019).

[31] I. Niskanen, T. Suopajärvi, H. Liimatainen, T. Fabritius, R. Heikkilä, G. Thungström, Determining the complex refractive index of cellulose nanocrystals by combination of Beer-Lambert and immersion matching methods, J. Quant. Spectrosc. Radiat. Transf. 235 (2019) 1–6. https://doi.org/10.1016/j.jqsrt.2019.06.023.

[32] S.M. Mahpeykar, Y. Zhao, X. Li, Z. Yang, Q. Xu, Z.-H. Lu, E.H. Sargent, X. Wang, Cellulose Nanocrystal:Polymer Hybrid Optical Diffusers for Index-Matching-Free Light Management in Optoelectronic Devices, Adv. Opt. Mater. 5 (2017) 1700430. https://doi.org/10.1002/adom.201700430.

[33] S.K. Evans, O.N. Wesley, O. Nathan, M.J. Moloto, Chemically purified cellulose and its nanocrystals from sugarcane baggase: isolation and characterization, Heliyon. 5 (2019) e02635. https://doi.org/10.1016/j.heliyon.2019.e02635.

[34] N.M. Stark, D.J. Yelle, U.P. Agarwal, Techniques for Characterizing Lignin, in: Lignin Polym. Compos., Elsevier Inc., 2016: pp. 49–66. https://doi.org/10.1016/B978-0-323-35565-0.00004-7.

[35] A. Goetzberger, W. Greube, Solar energy conversion with fluorescent collectors, Appl. Phys. 14 (1977) 123–139. https://doi.org/10.1007/BF00883080.

[36] U. Rau, F. Einsele, G.C. Glaeser, Efficiency limits of photovoltaic fluorescent collectors, Appl. Phys. Lett. 87 (2005) 171101. https://doi.org/10.1063/1.2112196.

[37] W.H. Weber, J. Lambe, Luminescent greenhouse collector for solar radiation, Appl. Opt. 15 (1976) 2299. https://doi.org/10.1364/AO.15.002299.

[38] M.K. Assadi, H. Hanaei, N.M. Mohamed, R. Saidur, S. Bakhoda, R. Bashiri, M. Moayedfar,

Enhancing the efficiency of luminescent solar concentrators (LSCs), Appl. Phys. A. 122 (2016) 821. https://doi.org/10.1007/s00339-016-0359-2.

[39] W.G.J.H.M. van Sark, K.W.J. Barnham, L.H. Slooff, A.J. Chatten, A. Büchtemann, A. Meyer, S.J. McCormack, R. Koole, D.J. Farrell, R. Bose, E.E. Bende, A.R. Burgers, T. Budel, J. Quilitz, M. Kennedy, T. Meyer, C.D.M. Donegá, A. Meijerink, D. Vanmaekelbergh, Luminescent Solar Concentrators - A review of recent results, Opt. Express. 16 (2008) 21773. https://doi.org/10.1364/OE.16.021773.

[40] A.M. Hermann, Luminescent solar concentrators—A review, Sol. Energy. 29 (1982) 323–329. https://doi.org/10.1016/0038-092X(82)90247-X.

[41] R. Reisfeld, C.K. Jørgensen, Luminescent solar concentrators for energy conversion, in: Sol. Energy Mater., Springer Berlin Heidelberg, Berlin, Heidelberg, 1982: pp. 1–36. https://doi.org/10.1007/BFb0111291.

[42] B.C. Rowan, L.R. Wilson, B.S. Richards, Advanced Material Concepts for Luminescent Solar Concentrators, IEEE J. Sel. Top. Quantum Electron. 14 (2008) 1312–1322. https://doi.org/10.1109/JSTQE.2008.920282.

[43] M.J. Currie, J.K. Mapel, T.D. Heidel, S. Goffri, M.A. Baldo, High-Efficiency Organic Solar Concentrators for Photovoltaics, Science (80-.). 321 (2008) 226–228. https://doi.org/10.1126/science.1158342.

[44] L.R. Wilson, B.S. Richards, Measurement method for photoluminescent quantum yields of fluorescent organic dyes in polymethyl methacrylate for luminescent solar concentrators, Appl. Opt. 48 (2009) 212. https://doi.org/10.1364/AO.48.000212.

[45] F. Purcell-Milton, Y.K. Gun'ko, Quantum dots for Luminescent Solar Concentrators, J. Mater. Chem. 22 (2012) 16687. https://doi.org/10.1039/c2jm32366d.

[46] K. Barnham, J.L. Marques, J. Hassard, P. O'Brien, Quantum-dot concentrator and thermodynamic model for the global redshift, Appl. Phys. Lett. (2000). https://doi.org/10.1063/1.125981.

[47] A.J. Chatten, K.W.J. Barnham, B.F. Buxton, N.J. Ekins-Daukes, M.A. Malik, Quantum dot solar concentrators, Semiconductors. 38 (2004) 909–917. https://doi.org/10.1134/1.1787111.

[48] A.J. Chatten, K.W.J. Barnham, B.F. Buxton, N.J. Ekins-Daukes, M.A. Malik, A new approach to modelling quantum dot concentrators, Sol. Energy Mater. Sol. Cells. 75 (2003) 363–371. https://doi.org/10.1016/S0927-0248(02)00182-4.

[49] J. Bomm, A. Büchtemann, A.J. Chatten, R. Bose, D.J. Farrell, N.L.A. Chan, Y. Xiao, L.H. Slooff, T. Meyer, A. Meyer, W.G.J.H.M. van Sark, R. Koole, Fabrication and full characterization of state-of-the-art quantum dot luminescent solar concentrators, Sol. Energy Mater. Sol. Cells. 95 (2011) 2087–2094. https://doi.org/10.1016/j.solmat.2011.02.027.

[50] J. Xue, F. Song, X. Yin, X. Wang, Y. Wang, Let It Shine: A Transparent and Photoluminescent Foldable Nanocellulose/Quantum Dot Paper, ACS Appl. Mater. Interfaces. 7 (2015) 10076–10079. https://doi.org/10.1021/acsami.5b02011.

[51] M. Zhu, X. Peng, Z. Wang, Z. Bai, B. Chen, Y. Wang, H. Hao, Z. Shao, H. Zhong, S. Kim, Highly transparent and colour-tunable composite films with increased quantum dot loading, J. Mater. Chem. C. 2 (2014) 10031–10036. https://doi.org/10.1039/C4TC01768D.

[52]   M. Kennedy, S.J. McCormack, J. Doran, B. Norton, Modelling the Effect of Device Geometry on Concentration Ratios of Quantum Dot Solar Concentrators, in: Proc. ISES World Congr. 2007 (Vol. I – Vol. V), Springer Berlin Heidelberg, Berlin, Heidelberg, 2008: pp. 1484–1488. https://doi.org/10.1007/978-3-540-75997-3_301.

[53]   S.T. Bailey, G.E. Lokey, M.S. Hanes, J.D.M. Shearer, J.B. McLafferty, G.T. Beaumont, T.T. Baseler, J.M. Layhue, D.R. Broussard, Y.-Z. Zhang, B.P. Wittmershaus, Optimized excitation energy transfer in a three-dye luminescent solar concentrator, Sol. Energy Mater. Sol. Cells. 91 (2007) 67–75. https://doi.org/10.1016/j.solmat.2006.07.011.

[54]   A.A. Earp, G.B. Smith, J. Franklin, P. Swift, Optimisation of a three-colour luminescent solar concentrator daylighting system, Sol. Energy Mater. Sol. Cells. 84 (2004) 411–426. https://doi.org/10.1016/j.solmat.2004.02.046.

[55]   H. Hernandez-Noyola, D.H. Potterveld, R.J. Holt, S.B. Darling, Optimizing luminescent solar concentrator design, Energy Environ. Sci. 5 (2012) 5798–5802. https://doi.org/10.1039/C1EE02376D.

[56]   † Julie S. Biteen, † Luke A. Sweatlock, ‡ Hans Mertens, † Nathan S. Lewis, ‡ and Albert Polman, † Harry A. Atwater*, Plasmon-Enhanced Photoluminescence of Silicon Quantum Dots: Simulation and Experiment, (2007). https://doi.org/10.1021/JP074160+.

[57]   C. Tummeltshammer, A. Taylor, A.J. Kenyon, I. Papakonstantinou, Losses in luminescent solar concentrators unveiled, Sol. Energy Mater. Sol. Cells. 144 (2016) 40–47. https://doi.org/10.1016/J.SOLMAT.2015.08.008.

[58]   G. Griffini, M. Levi, S. Turri, Novel high-durability luminescent solar concentrators based on fluoropolymer coatings, Prog. Org. Coatings. 77 (2014) 528–536.

https://doi.org/10.1016/j.porgcoat.2013.11.016.

[59] G. Griffini, M. Levi, S. Turri, Novel crosslinked host matrices based on fluorinated polymers for long-term durability in thin-film luminescent solar concentrators, Sol. Energy Mater. Sol. Cells. 118 (2013) 36–42. https://doi.org/10.1016/j.solmat.2013.05.041.

[60] G. Griffini, L. Brambilla, M. Levi, M. Del Zoppo, S. Turri, Photo-degradation of a perylene-based organic luminescent solar concentrator: Molecular aspects and device implications, Sol. Energy Mater. Sol. Cells. 111 (2013) 41–48. https://doi.org/10.1016/j.solmat.2012.12.021.

[61] V. Fattori, M. Melucci, L. Ferrante, M. Zambianchi, I. Manet, W. Oberhauser, G. Giambastiani, M. Frediani, G. Giachi, N. Camaioni, Poly(lactic acid) as a transparent matrix for luminescent solar concentrators: a renewable material for a renewable energy technology, Energy Environ. Sci. 4 (2011) 2849. https://doi.org/10.1039/c1ee01391b.

[62] M. Melucci, M. Durso, L. Favaretto, M.L. Capobianco, V. Benfenati, A. Sagnella, G. Ruani, M. Muccini, R. Zamboni, V. Fattori, N. Camaioni, Silk doped with a bio-modified dye as a viable platform for eco-friendly luminescent solar concentrators, RSC Adv. 2 (2012) 8610. https://doi.org/10.1039/c2ra21568c.

[63] D. Klemm, F. Kramer, S. Moritz, T. Lindström, M. Ankerfors, D. Gray, A. Dorris, Nanocelluloses: A New Family of Nature-Based Materials, Angew. Chemie Int. Ed. 50 (2011) 5438–5466. https://doi.org/10.1002/anie.201001273.

[64] S.J. Eichhorn, A. Dufresne, M. Aranguren, N.E. Marcovich, J.R. Capadona, S.J. Rowan, C. Weder, W. Thielemans, M. Roman, S. Renneckar, W. Gindl, S. Veigel, J. Keckes, H. Yano, K. Abe, M. Nogi, A.N. Nakagaito, A. Mangalam, J. Simonsen, A.S. Benight, A. Bismarck,

L.A. Berglund, T. Peijs, Review: current international research into cellulose nanofibres and nanocomposites, J. Mater. Sci. 45 (2010) 1–33. https://doi.org/10.1007/s10853-009-3874-0.

[65] R.J. Moon, A. Martini, J. Nairn, J. Simonsen, J. Youngblood, Cellulose nanomaterials review: structure, properties and nanocomposites, Chem. Soc. Rev. 40 (2011) 3941. https://doi.org/10.1039/c0cs00108b.

[66] Y. Habibi, L.A. Lucia, O.J. Rojas, Cellulose Nanocrystals: Chemistry, Self-Assembly, and Applications, Chem. Rev. 110 (2010) 3479–3500. https://doi.org/10.1021/cr900339w.

[67] E. Lam, K.B. Male, J.H. Chong, A.C.W. Leung, J.H.T. Luong, Applications of functionalized and nanoparticle-modified nanocrystalline cellulose, Trends Biotechnol. 30 (2012) 283–290. https://doi.org/10.1016/j.tibtech.2012.02.001.

[68] A. Isogai, T. Saito, H. Fukuzumi, TEMPO-oxidized cellulose nanofibers, Nanoscale. 3 (2011) 71–85. https://doi.org/10.1039/C0NR00583E.

[69] L. Meng, S.M. Mahpeykar, Q. Xiong, B. Ahvazi, X. Wang, Strain sensors on water-soluble cellulose nanofibril paper by polydimethylsiloxane (PDMS) stencil lithography, RSC Adv. 6 (2016) 85427–85433. https://doi.org/10.1039/C6RA10069D.

[70] Golden Artist Colors, Inc., (n.d.). http://www.goldenpaints.com/technicalinfo_selfgel (accessed January 1, 2017).

[71] F.I. Chowdhury, C. Dick, L. Meng, S.M. Mahpeykar, B. Ahvazi, X. Wang, Cellulose nanocrystals as host matrix and waveguide materials for recyclable luminescent solar concentrators, RSC Adv. 7 (2017) 32436–32441. https://doi.org/10.1039/C7RA04344A.

[72] L.R. Wilson, B.C. Rowan, N. Robertson, O. Moudam, A.C. Jones, B.S. Richards, Characterization and reduction of reabsorption losses in luminescent solar concentrators, Appl. Opt. 49 (2010) 1651. https://doi.org/10.1364/AO.49.001651.

[73] R.W. Olson, R.F. Loring, M.D. Fayer, Luminescent solar concentrators and the reabsorption problem, Appl. Opt. 20 (1981) 2934. https://doi.org/10.1364/AO.20.002934.

[74] Stan Cox, Cooling a Warming Planet: A Global Air Conditioning Surge - Yale E360, 2012-07-10. (n.d.). http://e360.yale.edu/features/cooling_a_warming_planet_a_global_air_conditioning_surge (accessed September 9, 2019).

[75] J. Steven Brown, P.A. Domanski, Review of alternative cooling technologies, Appl. Therm. Eng. 64 (2014) 252–262. https://doi.org/10.1016/j.applthermaleng.2013.12.014.

[76] The Guardian, World set to use more energy for cooling than heating | Environment | The Guardian, (2015). https://www.theguardian.com/environment/2015/oct/26/cold-economy-cop21-global-warming-carbon-emissions (accessed September 9, 2019).

[77] A.R. Gentle, G.B. Smith, Radiative Heat Pumping from the Earth Using Surface Phonon Resonant Nanoparticles, Nano Lett. 10 (2010) 373–379. https://doi.org/10.1021/nl903271d.

[78] A.R. Gentle, G.B. Smith, A Subambient Open Roof Surface under the Mid-Summer Sun, Adv. Sci. 2 (2015) 1500119. https://doi.org/10.1002/advs.201500119.

[79] A.W. Harrison, M.R. Walton, Radiative cooling of TiO2 white paint, Sol. Energy. 20 (1978) 185–188. https://doi.org/10.1016/0038-092X(78)90195-0.

[80] B. Bartoli, S. Catalanotti, B. Coluzzi, V. Cuomo, V. Silvestrini, G. Troise, Nocturnal and

diurnal performances of selective radiators, Appl. Energy. 3 (1977) 267–286. https://doi.org/10.1016/0306-2619(77)90015-0.

[81]   D.J. Fixsen, The temperature of the cosmic microwave background, Astrophys. J. 707 (2009) 916–920. https://doi.org/10.1088/0004-637X/707/2/916.

[82]   C.G. Granqvist, A. Hjortsberg, Radiative cooling to low temperatures: General considerations and application to selectively emitting SiO films, J. Appl. Phys. 52 (1981) 4205–4220. https://doi.org/10.1063/1.329270.

[83]   C.G. Granqvist, Radiative heating and cooling with spectrally selective surfaces, Appl. Opt. 20 (1981) 2606. https://doi.org/10.1364/AO.20.002606.

[84]   S. Catalanotti, V. Cuomo, G. Piro, D. Ruggi, V. Silvestrini, G. Troise, The radiative cooling of selective surfaces, Sol. Energy. 17 (1975) 83–89. https://doi.org/10.1016/0038-092X(75)90062-6.

[85]   D. Michell, K.L. Biggs, Radiation cooling of buildings at night, Appl. Energy. 5 (1979) 263–275. https://doi.org/10.1016/0306-2619(79)90017-5.

[86]   J. Hollick, Nocturnal Radiation Cooling Tests, Energy Procedia. 30 (2012) 930–936. https://doi.org/10.1016/J.EGYPRO.2012.11.105.

[87]   S.N. Bathgate, S.G. Bosi, A robust convection cover material for selective radiative cooling applications, Sol. Energy Mater. Sol. Cells. 95 (2011) 2778–2785. https://doi.org/10.1016/J.SOLMAT.2011.05.027.

[88]   X. Lu, P. Xu, H. Wang, T. Yang, J. Hou, Cooling potential and applications prospects of passive radiative cooling in buildings: The current state-of-the-art, Renew. Sustain. Energy

Rev. 65 (2016) 1079–1097. https://doi.org/10.1016/J.RSER.2016.07.058.

[89]   A.R. Gentle, G.B. Smith, Radiative Heat Pumping from the Earth Using Surface Phonon Resonant Nanoparticles, Nano Lett. 10 (2010) 373–379. https://doi.org/10.1021/nl903271d.

[90]   M.M. Hossain, B. Jia, M. Gu, A Metamaterial Emitter for Highly Efficient Radiative Cooling, Adv. Opt. Mater. 3 (2015) 1047–1051. https://doi.org/10.1002/adom.201500119.

[91]   Solar Spectra - an overview | ScienceDirect Topics, (n.d.). https://www.sciencedirect.com/topics/earth-and-planetary-sciences/solar-spectra (accessed September 9, 2019).

[92]   A.P. Raman, M.A. Anoma, L. Zhu, E. Rephaeli, S. Fan, Passive radiative cooling below ambient air temperature under direct sunlight, Nature. 515 (2014) 540–544. https://doi.org/10.1038/nature13883.

[93]   T. Li, Y. Zhai, S. He, W. Gan, Z. Wei, M. Heidarinejad, D. Dalgo, R. Mi, X. Zhao, J. Song, J. Dai, C. Chen, A. Aili, A. Vellore, A. Martini, R. Yang, J. Srebric, X. Yin, L. Hu, A radiative cooling structural material., Science. 364 (2019) 760–763. https://doi.org/10.1126/science.aau9101.

[94]   R. Service, This engineered wood radiates heat into space, potentially slashing cooling costs, 2019. https://doi.org/10.1126/science.aay1466.

[95]   S. Dubey, J.N. Sarvaiya, B. Seshadri, Temperature Dependent Photovoltaic (PV) Efficiency and Its Effect on PV Production in the World – A Review, Energy Procedia. 33 (2013) 311–321. https://doi.org/10.1016/J.EGYPRO.2013.05.072.

[96]   E. Skoplaki, J.A. Palyvos, On the temperature dependence of photovoltaic module electrical

performance: A review of efficiency/power correlations, Sol. Energy. 83 (2009) 614–624. https://doi.org/10.1016/J.SOLENER.2008.10.008.

[97] Lignin – a natural resource with huge potential - Bioeconomy, (n.d.). https://www.biooekonomie-bw.de/en/articles/dossiers/lignin-a-natural-resource-with-huge-potential (accessed November 22, 2019).

[98] D. Zhao, A. Aili, Y. Zhai, S. Xu, G. Tan, X. Yin, R. Yang, Radiative sky cooling: Fundamental principles, materials, and applications, Appl. Phys. Rev. 6 (2019) 021306. https://doi.org/10.1063/1.5087281.

[99] L. Zhu, A.P. Raman, S. Fan, Radiative cooling of solar absorbers using a visibly transparent photonic crystal thermal blackbody., Proc. Natl. Acad. Sci. U. S. A. 112 (2015) 12282–7. https://doi.org/10.1073/pnas.1509453112.

[100] Vikocell 4.5W 156 x 156MM Polycrystalline Solar Cells 6x6 for DIY Solar Panel (Pack of 10): Amazon.co.uk: Garden & Outdoors, (n.d.). https://www.amazon.co.uk/VIKOCELL-Grade-Photovoltaic-Polycrystalline-Solar-x/dp/B06XJS45HS (accessed September 29, 2019).

[101] Y. Zhai, Y. Ma, S.N. David, D. Zhao, R. Lou, G. Tan, R. Yang, X. Yin, Scalable-manufactured randomized glass-polymer hybrid metamaterial for daytime radiative cooling., Science. 355 (2017) 1062–1066. https://doi.org/10.1126/science.aai7899.

[102] L.M. Johnson, L. Gao, C. Shields IV, M. Smith, K. Efimenko, K. Cushing, J. Genzer, G.P. López, Elastomeric microparticles for acoustic mediated bioseparations, J. Nanobiotechnology. 11 (2013) 22. https://doi.org/10.1186/1477-3155-11-22.

[103] F.A.B. Silva, F.A. Chagas-Silva, F.H. Florenzano, F.L. Pissetti, Poly(dimethylsiloxane) and Poly[vinyltrimethoxysilane- *co* -2-(dimethylamino) ethyl methacrylate] Based Cross-Linked Organic-Inorganic Hybrid Adsorbent for Copper(II) Removal from Aqueous Solutions, J. Braz. Chem. Soc. 27 (2016) 2181–2191. https://doi.org/10.5935/0103-5053.20160110.

[104] I. Bykov, Characterization of natural and technical lignins using FTIR spectroscopy, 2008. http://www.diva-portal.org/smash/record.jsf?pid=diva2%3A1016107&dswid=-5069 (accessed September 10, 2019).

[105] M.M. Hossain, M. Gu, Radiative Cooling: Principles, Progress, and Potentials, Adv. Sci. 3 (2016) 1500360. https://doi.org/10.1002/advs.201500360.

[106] Y. Fu, J. Yang, Y.S. Su, W. Du, Y.G. Ma, Daytime passive radiative cooler using porous alumina, Sol. Energy Mater. Sol. Cells. 191 (2019) 50–54. https://doi.org/10.1016/J.SOLMAT.2018.10.027.

[107] Reference Solar Spectral Irradiance: Air Mass 1.5, (2016). http://rredc.nrel.gov/solar/spectra/am1.5/ (accessed May 1, 2016).

[108] D. Wang, Y.-H. Ye, Y. Zhu, Thin films of high reflectivity for efficient radiative cooling, in: Y. Yang (Ed.), Tenth Int. Conf. Inf. Opt. Photonics, SPIE, 2018: p. 179. https://doi.org/10.1117/12.2505995.

[109] H. Bao, C. Yan, B. Wang, X. Fang, C.Y. Zhao, X. Ruan, Double-layer nanoparticle-based coatings for efficient terrestrial radiative cooling, Sol. Energy Mater. Sol. Cells. 168 (2017) 78–84. https://doi.org/10.1016/J.SOLMAT.2017.04.020.

[110] H. Zhang, S. Fu, Y. Chen, Basic understanding of the color distinction of lignin and the proper selection of lignin in color-depended utilizations, Int. J. Biol. Macromol. 147 (2020) 607–615. https://doi.org/10.1016/J.IJBIOMAC.2020.01.105.

[111] S.C. Lee, T.M.T. Tran, J.W. Choi, K. Won, Lignin for white natural sunscreens, Int. J. Biol. Macromol. 122 (2019) 549–554. https://doi.org/10.1016/j.ijbiomac.2018.10.184.

[112] W. Wei, Y. Zhu, Q. Li, Z. Cheng, Y. Yao, Q. Zhao, P. Zhang, X. Liu, Z. Chen, F. Xu, Y. Gao, An Al2O3-cellulose acetate-coated textile for human body cooling, Sol. Energy Mater. Sol. Cells. 211 (2020) 110525. https://doi.org/10.1016/j.solmat.2020.110525.

[113] Y. Chen, B. Dang, J. Fu, C. Wang, C. Li, Q. Sun, H. Li, Cellulose-Based Hybrid Structural Material for Radiative Cooling, Nano Lett. (2020). https://doi.org/10.1021/acs.nanolett.0c03738.

[114] S. Gamage, E.S.H. Kang, C. Åkerlind, S. Sardar, J. Edberg, H. Kariis, T. Ederth, M. Berggren, M.P. Jonsson, Transparent nanocellulose metamaterial enables controlled optical diffusion and radiative cooling, J. Mater. Chem. C. 8 (2020) 11687–11694. https://doi.org/10.1039/d0tc01226b.

[115] Y. Zhai, Y. Ma, S.N. David, D. Zhao, R. Lou, G. Tan, R. Yang, X. Yin, Scalable-manufactured randomized glass-polymer hybrid metamaterial for daytime radiative cooling, Science (80-.). 355 (2017) 1062–1066. https://doi.org/10.1126/science.aai7899.

[116] C.L. Frye, The environmental fate and ecological impact of organosilicon materials: A review, Sci. Total Environ. 73 (1988) 17–22. https://doi.org/10.1016/0048-9697(88)90182-9.

[117] D.M. Smith, R. Narayan, R.G. Lehmann, G.E. Kozerski, J.R. Miller, Fate and effects of silicone polymer during the composting process, Compost Sci. Util. 6 (1998) 6–12. https://doi.org/10.1080/1065657X.1998.10701916.

[118] R.G. Lehmann, C.L. Frye, D.A. Tolle, T.C. Zwick, Fate of sludge-applied silicones in agricultural soil microcosms, Water. Air. Soil Pollut. 87 (1996) 231–243. https://doi.org/10.1007/BF00696839.

[119] T. Lv, J. Huang, W. Liu, R. Zhang, From sky back to sky: Embedded transparent cellulose membrane to improve the thermal performance of solar module by radiative cooling, Case Stud. Therm. Eng. 18 (2020) 100596. https://doi.org/10.1016/j.csite.2020.100596.

[120] SYLGARD® 184, (n.d.). https://www.sigmaaldrich.com/catalog/product/aldrich/761036?lang=en&region=CA&gclid=Cj0KCQiA-bjyBRCcARIsAFboWg1UuwXHmiNEMq2ACflP6c4t5xzpmyjqeoD51yaOMYb01lSjh3E1WdAaAsemEALw_wcB (accessed February 20, 2020).

[121] A. Mandal, D. Chakrabarty, Isolation of nanocellulose from waste sugarcane bagasse (SCB) and its characterization, Carbohydr. Polym. 86 (2011) 1291–1299. https://doi.org/10.1016/j.carbpol.2011.06.030.

[122] W.T. Wulandari*, A Rochliadi and I M Arcana, Nanocellulose prepared by acid hydrolysis of isolated cellulose from sugarcane bagasse, in: IOP Conf. Ser. Mater. Sci. Eng., 2016. https://doi.org/10.1088/1757-899X/107/1/012045.

[123] timeanddate.com, (n.d.). https://www.timeanddate.com/ (accessed July 1, 2020).

[124] Q. Xu, L. Meng, X. Wang, Reducing shadowing losses in silicon solar cells using cellulose nanocrystal: polymer hybrid diffusers, Appl. Opt. 58 (2019) 2505. https://doi.org/10.1364/AO.58.002505.

[125] P. Pust, P.J. Schmidt, W. Schnick, A revolution in lighting, Nat. Mater. 14 (2015). https://doi.org/10.1038/nmat4270.

[126] J. Cho, J.H. Park, J.K. Kim, E.F. Schubert, White light-emitting diodes: History, progress, and future, Laser Photonics Rev. 11 (2017). https://doi.org/10.1002/lpor.201600147.

[127] Q. Xu, L. Meng, X. Wang, Nanocrystal-filled polymer for improving angular color uniformity of phosphor-converted white LEDs, Appl. Opt. 58 (2019) 7649. https://doi.org/10.1364/ao.58.007649.

[128] T. Nishida, T. Ban, N. Kobayashi, High-color-rendering light sources consisting of a 350-nm ultraviolet light-emitting diode and three-basal-color phosphors, Appl. Phys. Lett. 82 (2003) 3817–3819. https://doi.org/10.1063/1.1580649.

[129] D.A. Steigerwald, J.C. Bhat, D. Collins, R.M. Fletcher, M.O. Holcomb, M.J. Ludowise, P.S. Martin, S.L. Rudaz, Illumination with solid state lighting technology, IEEE J. Sel. Top. Quantum Electron. 8 (2002) 310–320. https://doi.org/10.1109/2944.999186.

[130] J.K. Huang, D.W. Lin, M.H. Shih, K.Y. Lee, J.R. Chen, H.W. Huang, S.Y. Kuo, C.H. Lin, P.T. Lee, G.C. Chi, H.C. Kuo, Investigation and comparison of the gan-based light-emitting diodes grown on high aspect ratio nano-cone and general micro-cone patterned sapphire substrate, IEEE/OSA J. Disp. Technol. 9 (2013) 947–952. https://doi.org/10.1109/JDT.2013.2270276.

[131] M. Kumar, Sunny, A. Kumar, K.-S. Seong, S.-H. Park, GaN phosphors converted white light-emitting diodes for high luminous efficacy and improved thermal stability, IET Optoelectron. 14 (2020) 155–158. https://doi.org/10.1049/iet-opt.2019.0084.

[132] T.S. Zheleva, O.H. Nam, M.D. Bremser, R.F. Davis, Dislocation density reduction via lateral epitaxy in selectively grown GaN structures, Appl. Phys. Lett. 71 (1997) 2472–2474. https://doi.org/10.1063/1.120091.

[133] D.S. Wuu, W.K. Wang, K.S. Wen, S.C. Huang, S.H. Lin, S.Y. Huang, C.F. Lin, R.H. Horng, Defect reduction and efficiency improvement of near-ultraviolet emitters via laterally overgrown GaN on a GaN/patterned sapphire template, Appl. Phys. Lett. 89 (2006) 161105. https://doi.org/10.1063/1.2363148.

[134] K.J. Chen, H.C. Chen, M.H. Shih, C.H. Wang, H.H. Tsai, S.H. Chien, C.C. Lin, H.C. Kuo, Enhanced Luminous efficiency of WLEDs using a dual-layer structure of the remote phosphor package, J. Light. Technol. 31 (2013) 1941–1945. https://doi.org/10.1109/JLT.2013.2260322.

[135] H.C. Chen, K.J. Chen, C.H. Wang, C.C. Lin, C.C. Yeh, H.H. Tsai, M.H. Shih, H.C. Kuo, T.C. Lu, A novel randomly textured phosphor structure for highly efficient white light-emitting diodes, Nanoscale Res. Lett. 7 (2012) 1–5. https://doi.org/10.1186/1556-276X-7-188.

[136] D. Liu, X. Yun, G. Li, P. Dang, M.S. Molokeev, H. Lian, M. Shang, J. Lin, Enhanced Cyan Emission and Optical Tuning of $Ca_3Ga_4O_9:Bi^{3+}$ for High-Quality Full-Spectrum White Light-Emitting Diodes, Adv. Opt. Mater. 8 (2020) 2001037. https://doi.org/10.1002/adom.202001037.

[137] S.E. Brinkley, N. Pfaff, K.A. Denault, Z. Zhang, H.T. Hintzen, R. Seshadri, S. Nakamura, S.P. Denbaars, Robust thermal performance of Sr 2Si 5N 8:Eu 2+: An efficient red emitting phosphor for light emitting diode based white lighting, Appl. Phys. Lett. 99 (2011) 241106. https://doi.org/10.1063/1.3666785.

[138] Y. Zhang, L. Wu, M. Ji, B. Wang, Y. Kong, J. Xu, Structure and photoluminescence properties of KSr_4(BO_3)_3:Eu^3+ red-emitting phosphor, Opt. Mater. Express. 2 (2012) 92. https://doi.org/10.1364/ome.2.000092.

[139] M. Funato, K. Hayashi, M. Ueda, Y. Kawakami, Y. Narukawa, T. Mukai, Emission color tunable light-emitting diodes composed of InGaN multifacet quantum wells, Appl. Phys. Lett. 93 (2008) 021126. https://doi.org/10.1063/1.2956404.

[140] I.K. Park, M.K. Kwon, C.Y. Cho, J.Y. Kim, C.H. Cho, S.J. Park, Effect of InGaN quantum dot size on the recombination process in light-emitting diodes, Appl. Phys. Lett. 92 (2008) 253105. https://doi.org/10.1063/1.2951607.

[141] T. Meng, T. Yuan, X. Li, Y. Li, L. Fan, S. Yang, Ultrabroad-band, red sufficient, solid white emission from carbon quantum dot aggregation for single component warm white light emitting diodes with a 91 high color rendering index, Chem. Commun. 55 (2019) 6531–6534. https://doi.org/10.1039/c9cc01794a.

[142] K.-J. Chen, H.-V. Han, H.-C. Chen, C.-C. Lin, S.-H. Chien, C.-C. Huang, T.-M. Chen, M.-H. Shih, H.-C. Kuo, White light emitting diodes with enhanced CCT uniformity and luminous flux using ZrO2 nanoparticles, Nanoscale. 6 (2014) 5378–5383. https://doi.org/10.1039/C3NR06894C.

[143] H.-C. Chen, K.-J. Chen, C.-C. Lin, C.-H. Wang, H.-V. Han, H.-H. Tsai, H.-T. Kuo, S.-H.

Chien, M.-H. Shih, H.-C. Kuo, Improvement in uniformity of emission by ZrO $_2$ nano-particles for white LEDs, Nanotechnology. 23 (2012) 265201. https://doi.org/10.1088/0957-4484/23/26/265201.

[144] H.-T. Huang, C.-C. Tsai, Y.-P. Huang, Conformal phosphor coating using pulsed spray to reduce color deviation of white LEDs, Opt. Express. 18 (2010) A201. https://doi.org/10.1364/oe.18.00a201.

[145] Zongyuan Liu, Sheng Liu, Kai Wang, Xiaobing Luo, Optical Analysis of Color Distribution in White LEDs With Various Packaging Methods, IEEE Photonics Technol. Lett. 20 (2008) 2027–2029. https://doi.org/10.1109/LPT.2008.2005998.

[146] C. Sommer, P. Hartmann, P. Pachler, M. Schweighart, S. Tasch, G. Leising, F.P. Wenzl, A detailed study on the requirements for angular homogeneity of phosphor converted high power white LED light sources, Opt. Mater. (Amst). 31 (2009) 837–848. https://doi.org/10.1016/j.optmat.2008.09.009.

[147] Y. Shuai, Y. He, N.T. Tran, F.G. Shi, Angular CCT uniformity of phosphor converted white LEDs: Effects of phosphor materials and packaging structures, IEEE Photonics Technol. Lett. 23 (2011) 137–139. https://doi.org/10.1109/LPT.2010.2092759.

[148] K. Wang, D. Wu, F. Chen, Z. Liu, X. Luo, S. Liu, Angular color uniformity enhancement of white light-emitting diodes integrated with freeform lenses, Opt. Lett. 35 (2010) 1860. https://doi.org/10.1364/ol.35.001860.

[149] K.C. Huang, T.H. Lai, C.Y. Chen, Improved CCT uniformity of white LED using remote phosphor with patterned sapphire substrate, Appl. Opt. 52 (2013) 7376–7381. https://doi.org/10.1364/AO.52.007376.

[150] F.W. Mont, J.K. Kim, M.F. Schubert, E.F. Schubert, R.W. Siegel, High-refractive-index Ti O2 -nanoparticle-loaded encapsulants for light-emitting diodes, J. Appl. Phys. 103 (2008) 083120. https://doi.org/10.1063/1.2903484.

[151] G.Y. Song, I. Jang, S.W. Jeon, S.H. Ahn, J.Y. Kim, G. Sa, Controlling the Surface Properties of TiO2 for Improvement of the Photo-performance and Color Uniformity of the Light-emitting Diode Devices, J. Ind. Eng. Chem. 94 (2021) 180–187. https://doi.org/10.1016/j.jiec.2020.10.031.

[152] J. Liu, X. Lu, W. Wang, Z. Su, B. Xing, H. Zheng, S. Liu, Tailoring Particle Distribution for White LEDs with High Color-Uniformity by Selective Curing, IEEE Photonics Technol. Lett. (2020). https://doi.org/10.1109/LPT.2020.3046740.

[153] N. Zhuo, N. Zhang, P. Chen, H. Wang, Enhancement of efficiency and CCT uniformity for red phosphor thin films, red LEDs and laminated white LEDs based on near-ultraviolet LEDs using MgO nanoparticles, RSC Adv. 9 (2019) 28291–28298. https://doi.org/10.1039/c9ra06069c.

[154] J.P. You, N.T. Tran, F.G. Shi, Light extraction enhanced white light-emitting diodes with multi-layered phosphor configuration, Opt. Express. 18 (2010) 5055. https://doi.org/10.1364/oe.18.005055.

[155] Z.-T. Li, J.-Y. Liang, J.-S. Li, J.-X. Li, Y. Tang, Scattering Nanoparticles-Induced Reflection Effect for Enhancing Optical Efficiency of Inverted Quantum Dots-Light-Emitting Diodes Combined With the Centrifugation Technique, J. Electron. Packag. 143 (2021). https://doi.org/10.1115/1.4048034.

[156] L. Yang, Z. Lv, Y. Jiaojiao, S. Liu, Effects of melamine formaldehyde resin and CaCO3

diffuser-loaded encapsulation on correlated color temperature uniformity of phosphor-converted LEDs, Appl. Opt. 52 (2013) 5539–5544. https://doi.org/10.1364/AO.52.005539.

[157] L. Yang, S. Wang, Z. Lv, S. Liu, Color deviation controlling of phosphor conformal coating by advanced spray painting technology for white LEDs, Appl. Opt. 52 (2013) 2075–2079. https://doi.org/10.1364/AO.52.002075.

[158] Z. Li, Y. Zhai, Y. Wang, G.M. Wendland, X. Yin, J. Xiao, Harnessing Surface Wrinkling-Cracking Patterns for Tunable Optical Transmittance, Adv. Opt. Mater. 5 (2017) 1700425. https://doi.org/10.1002/adom.201700425.

[159] F.I. Chowdhury, Q. Xu, X. Wang, Improving the Light Quality of White Light-Emitting Diodes Using Cellulose Nanocrystal-Filled Phosphors, Adv. Photonics Res. (2021) 2100006. https://doi.org/10.1002/adpr.202100006.

[160] F.I. Chowdhury, C. Dick, L. Meng, S.M. Mahpeykar, B. Ahvazi, X. Wang, Cellulose nanocrystals as host matrix and waveguide materials for recyclable luminescent solar concentrators, RSC Adv. 7 (2017). https://doi.org/10.1039/c7ra04344a.

[161] H. Zheng, Y. Wang, L. Li, X. Fu, Y. Zou, X. Luo, Dip-transfer phosphor coating on designed substrate structure for high angular color uniformity of white light emitting diodes with conventional chips, Opt. Express. 21 (2013) A933. https://doi.org/10.1364/oe.21.00a933.

[162] S. Wang, X. Chen, M. Chen, H. Zheng, H. Yang, S. Liu, Improvement in angular color uniformity of white light-emitting diodes using screen-printed multilayer phosphor-in-glass, Appl. Opt. 53 (2014) 8492. https://doi.org/10.1364/ao.53.008492.

[163] K. Wang, F. Chen, Z. Liu, X. Luo, S. Liu, Design of compact freeform lens for application specific light-emitting diode packaging, Opt. Express. 18 (2010) 413. https://doi.org/10.1364/oe.18.000413.

[164] L. Chen, C.-C. Lin, C.-W. Yeh, R.-S. Liu, Light Converting Inorganic Phosphors for White Light-Emitting Diodes, Materials (Basel). 3 (2010) 2172–2195. https://doi.org/10.3390/ma3032172.

[165] F. Schneider, J. Draheim, R. Kamberger, U. Wallrabe, Process and material properties of polydimethylsiloxane (PDMS) for Optical MEMS, Sensors Actuators, A Phys. 151 (2009) 95–99. https://doi.org/10.1016/j.sna.2009.01.026.

[166] M. Novak, J. Nedoma, M. Fajkus, J. Jargus, V. Vasinek, Analysis of optical properties of special fibers of polydimethylsiloxane (PDMS) depending on the different methods of mixing PDMS and curing agent, in: K. Kalli, J. Kanka, A. Mendez, P. Peterka (Eds.), Micro-Structured Spec. Opt. Fibres V, SPIE, 2017: p. 102320O. https://doi.org/10.1117/12.2257064.

[167] S. Fan, L. Dan, L. Meng, W. Zheng, A. Elias, X. Wang, Improved response time of flexible microelectromechanical sensors employing eco-friendly nanomaterials, Nanoscale. 9 (2017) 16915–16921. https://doi.org/10.1039/c7nr05218a.

[168] M. Giese, L.K. Blusch, M.K. Khan, M.J. MacLachlan, Functional Materials from Cellulose-Derived Liquid-Crystal Templates, Angew. Chemie Int. Ed. 54 (2015) 2888–2910. https://doi.org/10.1002/anie.201407141.

[169] J.A. De La Cruz, Q. Liu, B. Senyuk, A.W. Frazier, K. Peddireddy, I.I. Smalyukh, Cellulose-Based Reflective Liquid Crystal Films as Optical Filters and Solar Gain Regulators, ACS
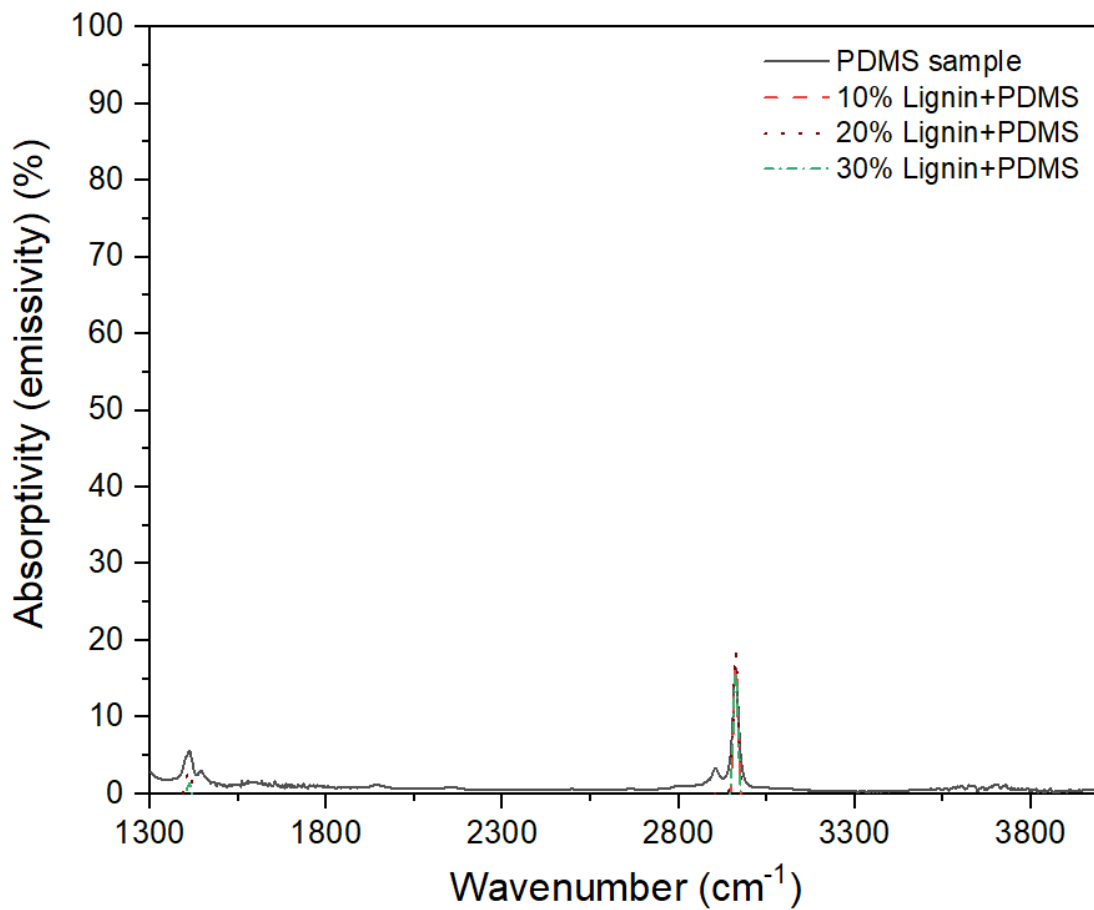
Figure 49. Spectral absorptivity (emissivity) of pure PDMS, 10 wt.%, 20 wt.%, and 30 wt.% lignin samples.

Figure 49 shows the absorption (emission) of the samples between 1300-4000 cm^{-1}, which is negligible compared to the absorption (emission) between 600-1300 cm^{-1}.
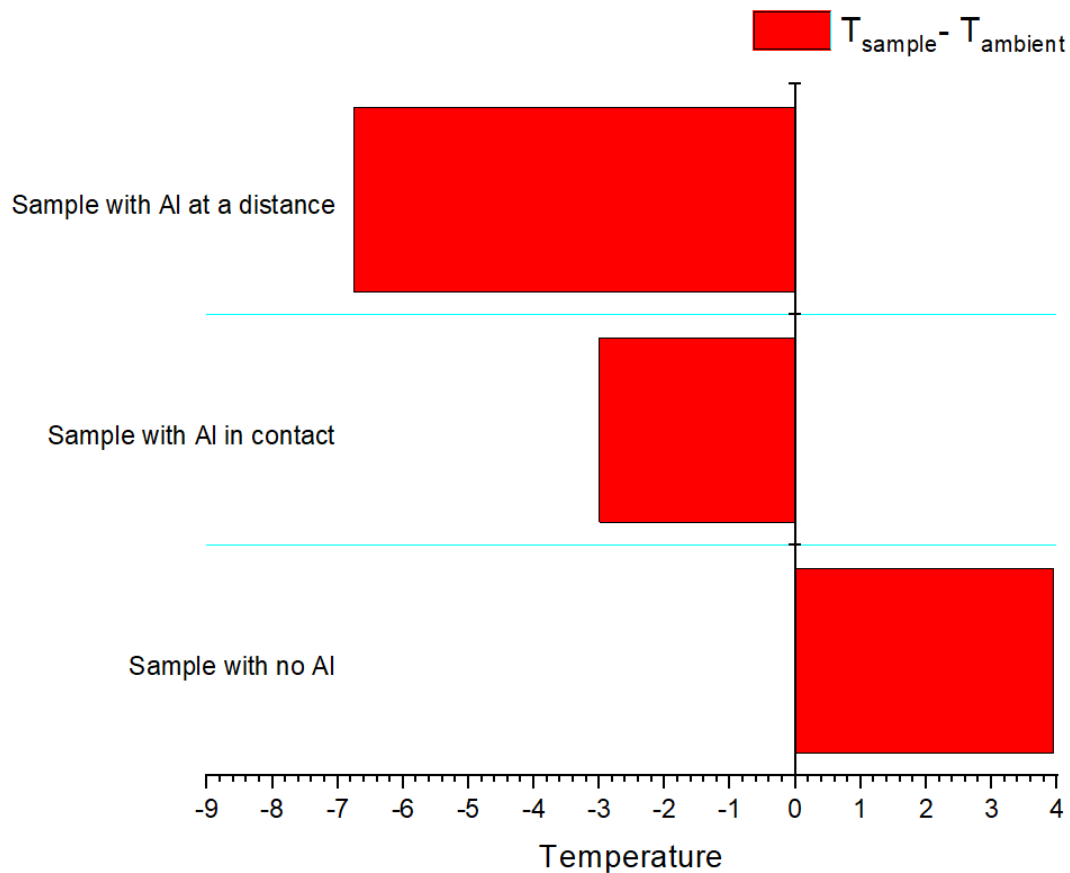
Figure 50. Effect of aluminum foil in the radiative cooling application.

Figure 50 shows the effect of Al foil on lignin-based samples under AM1.5G radiation. Without the foil, this sample would absorb the incoming solar radiation which would drastically change its radiative cooling potential. The experiment showed this sample will have an average temperature of 4 °C above the ambient temperature. Having a sample in contact with Al foil (Al foil was placed on the top) would ensure reflection of solar radiation but outgoing radiation from the sample would not be straight forward as it has to rely on internal reflection (reflection from the surface facing the sample) and gaps on the side. Still, such a sample would show some radiative cooling power as the experiment showing a sample

temperature 3 °C below the ambient temperature. The best solution would be placing Al foil a few mm over the sample so that Al foil reflects incoming solar radiation and at the same time allows radiation from the sample to escape efficiently. The experiment suggests such a technique would allow the sample to reach an average temperature 6.75 °C below the ambient temperature. Due to simplicity, the sample in contact with Al foil was used in this work.
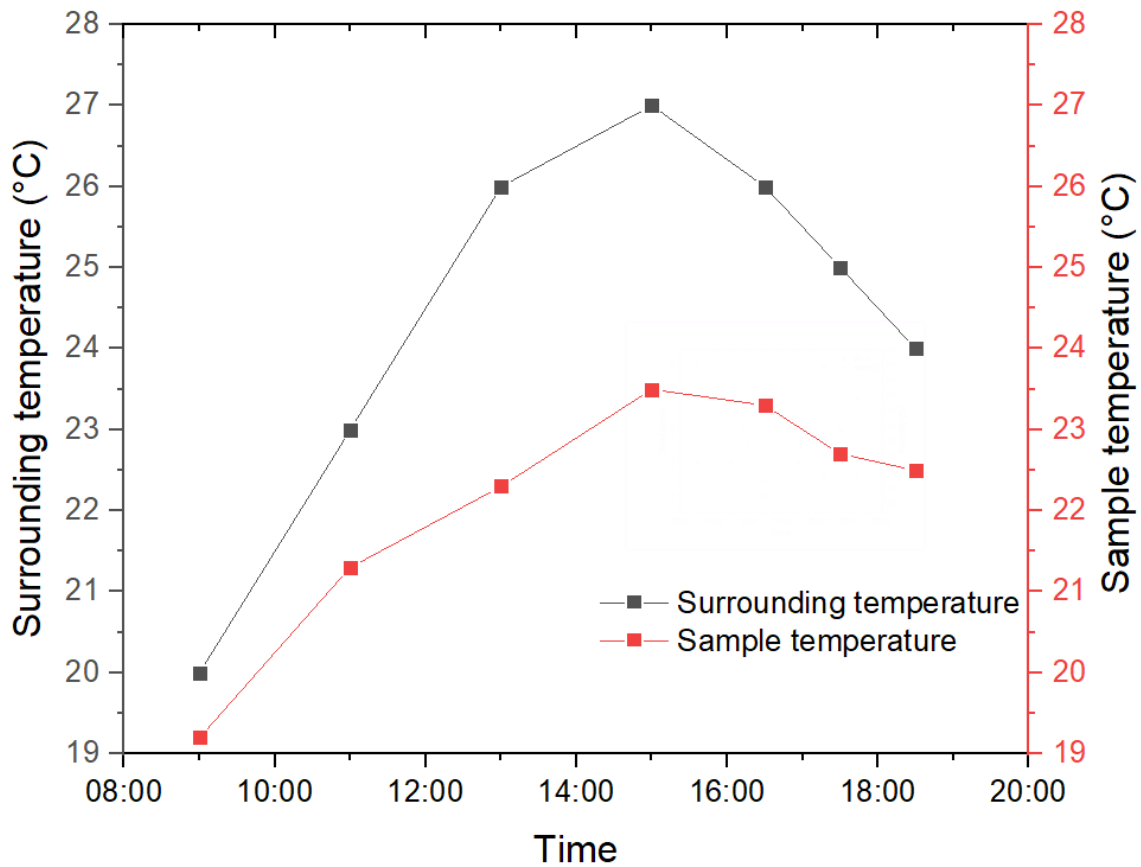
Figure 51. Surrounding and sample temperatures measured by the thermocouples.
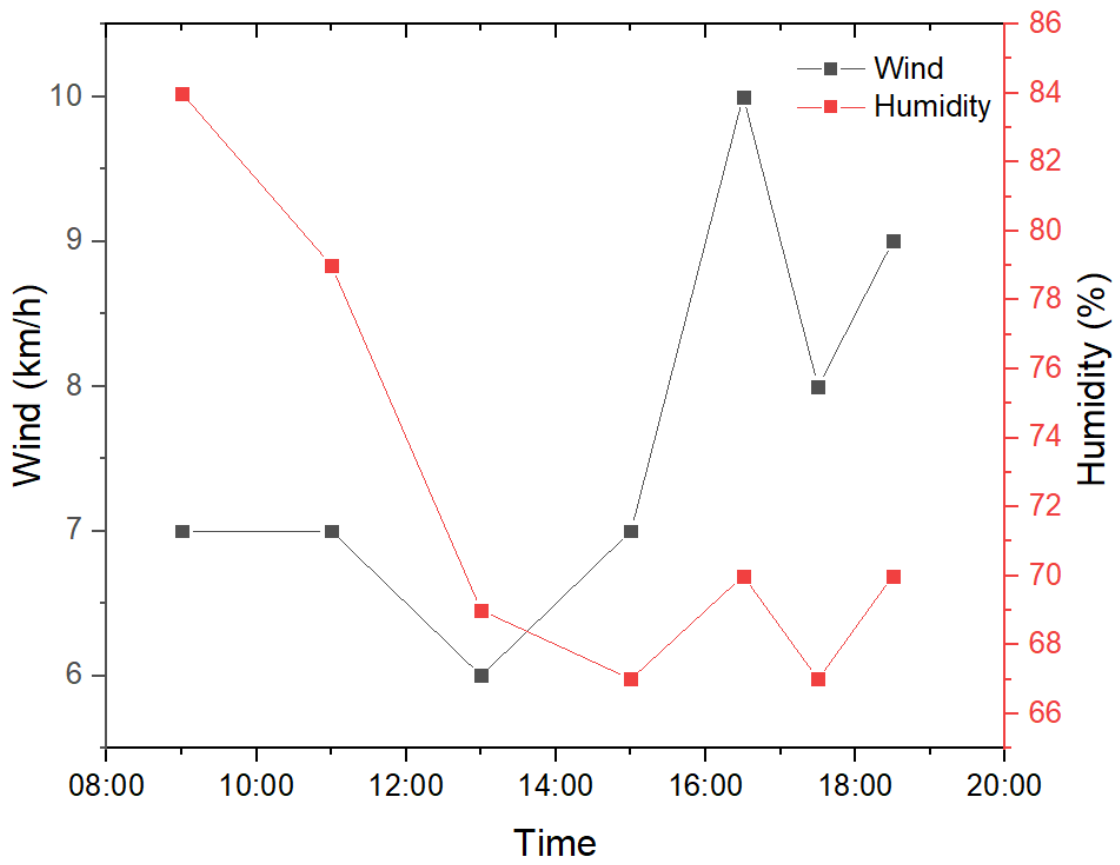
Figure 52. Wind speed and humidity during the outdoor measurement [123].
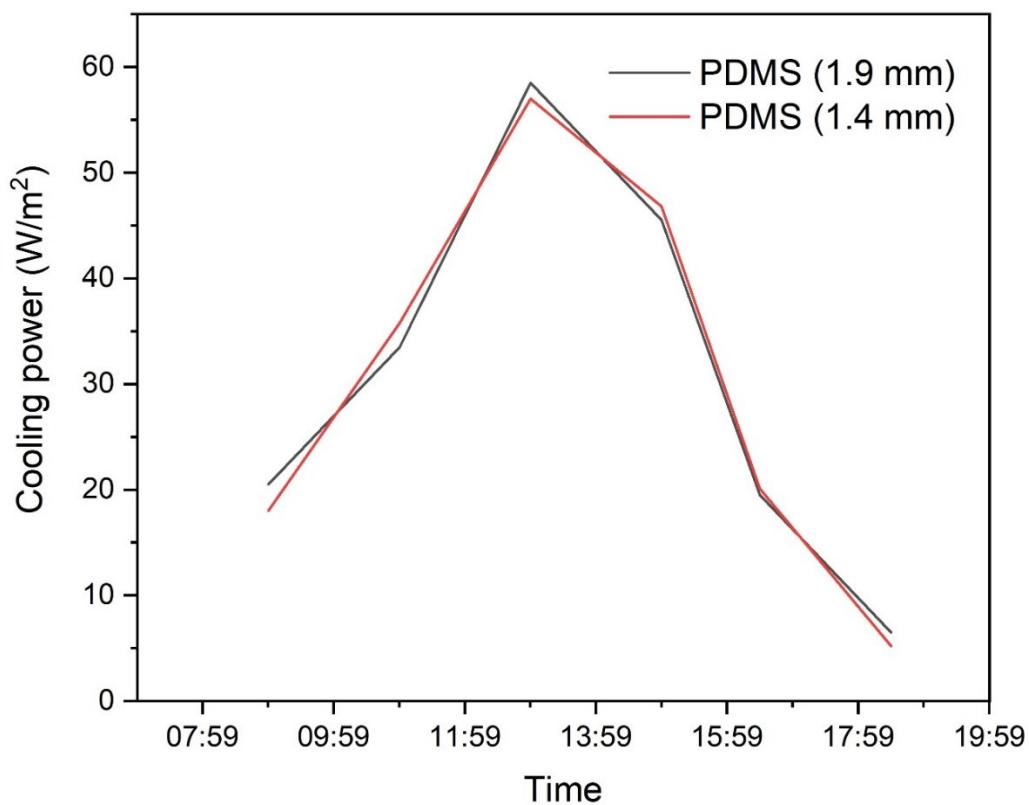
Figure 53. The measured cooling power of PDMS samples of different thicknesses.

Figure 53 shows the effect of thickness on the cooling power of the PDMS sample. Two samples of thicknesses 1.4 mm and 1.9 mm were fabricated, and their cooling powers were measured. The results show that thickness variation will have little effect on the cooling power of PDMS.
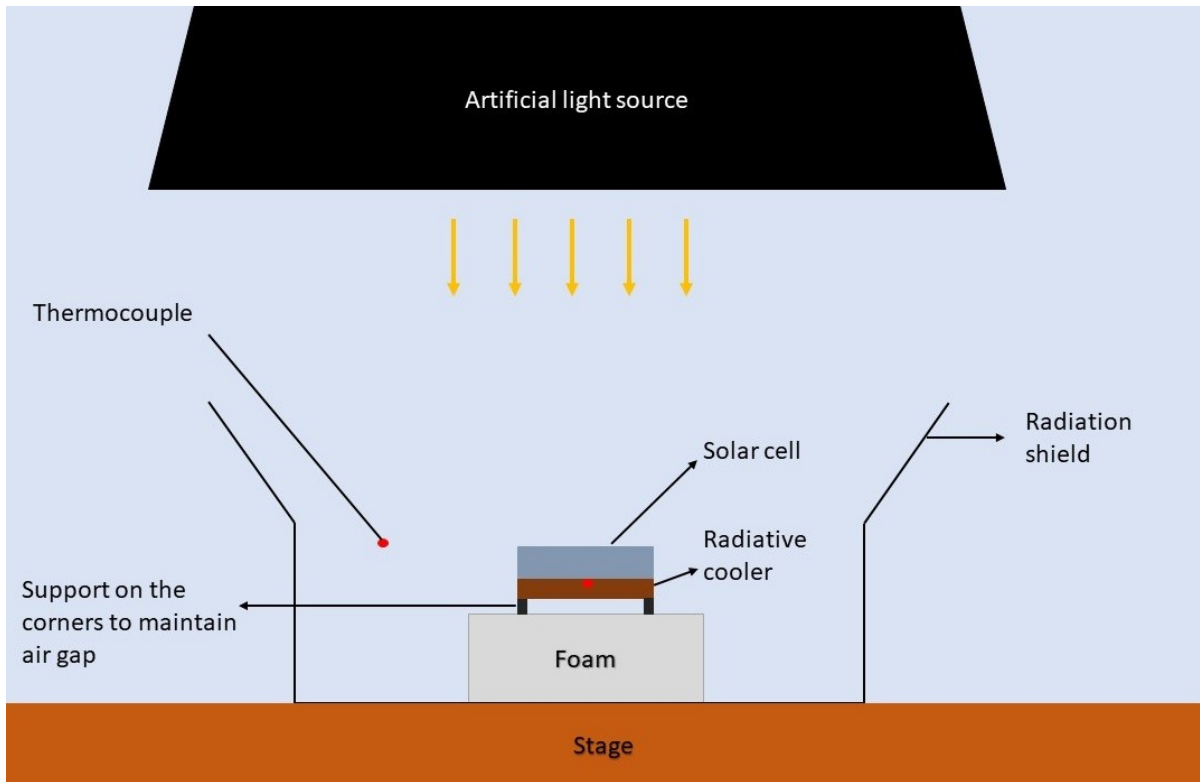
Figure 54. Schematic of the indoor setup for testing the effect of the radiative cooler on a solar cell.

Figure 54 shows the schematic of the setup that was used for evaluating the effect of a lignin-upgraded sample on a solar cell. Since we performed this experiment indoors, the lignin-upgraded sample exchanged heat with the surrounding instead of the sky. This experiment was conducted as a proof of concept to show that a lignin-upgraded sample can lower the operating temperature of a solar cell.
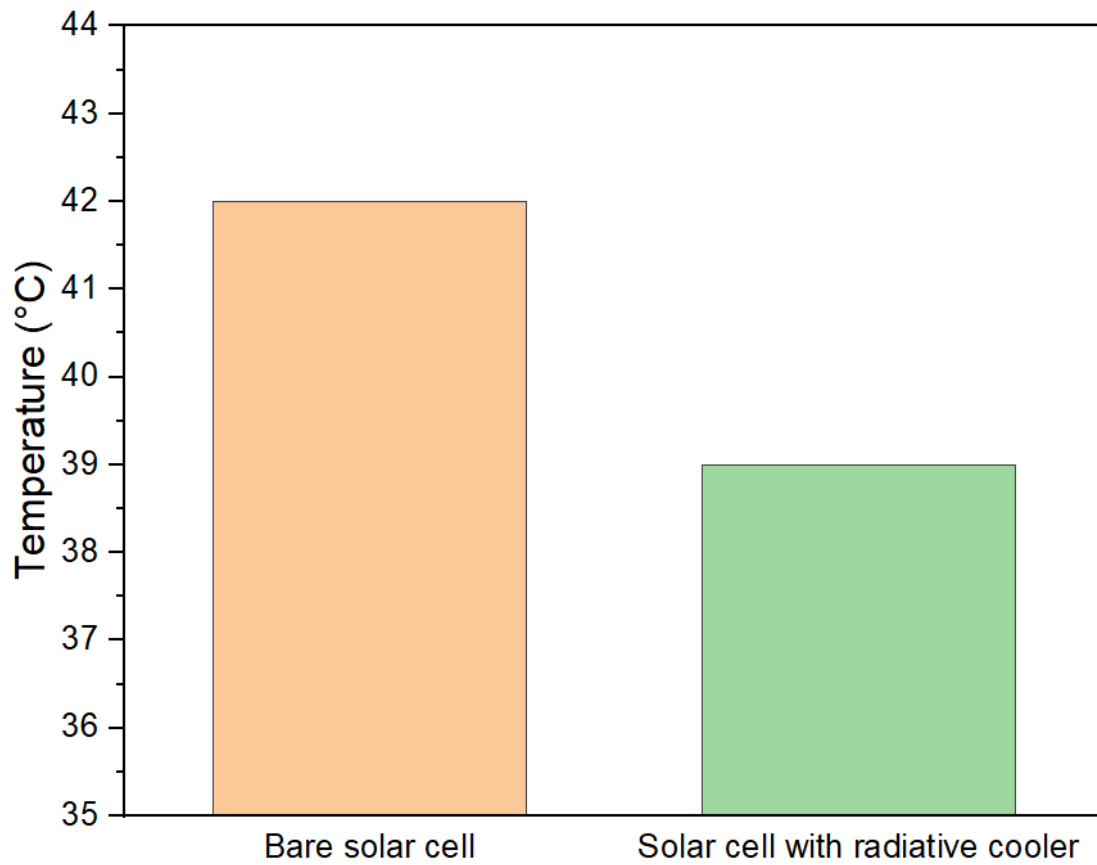
Figure 55. The temperature of the solar cell with and without a radiative cooler.
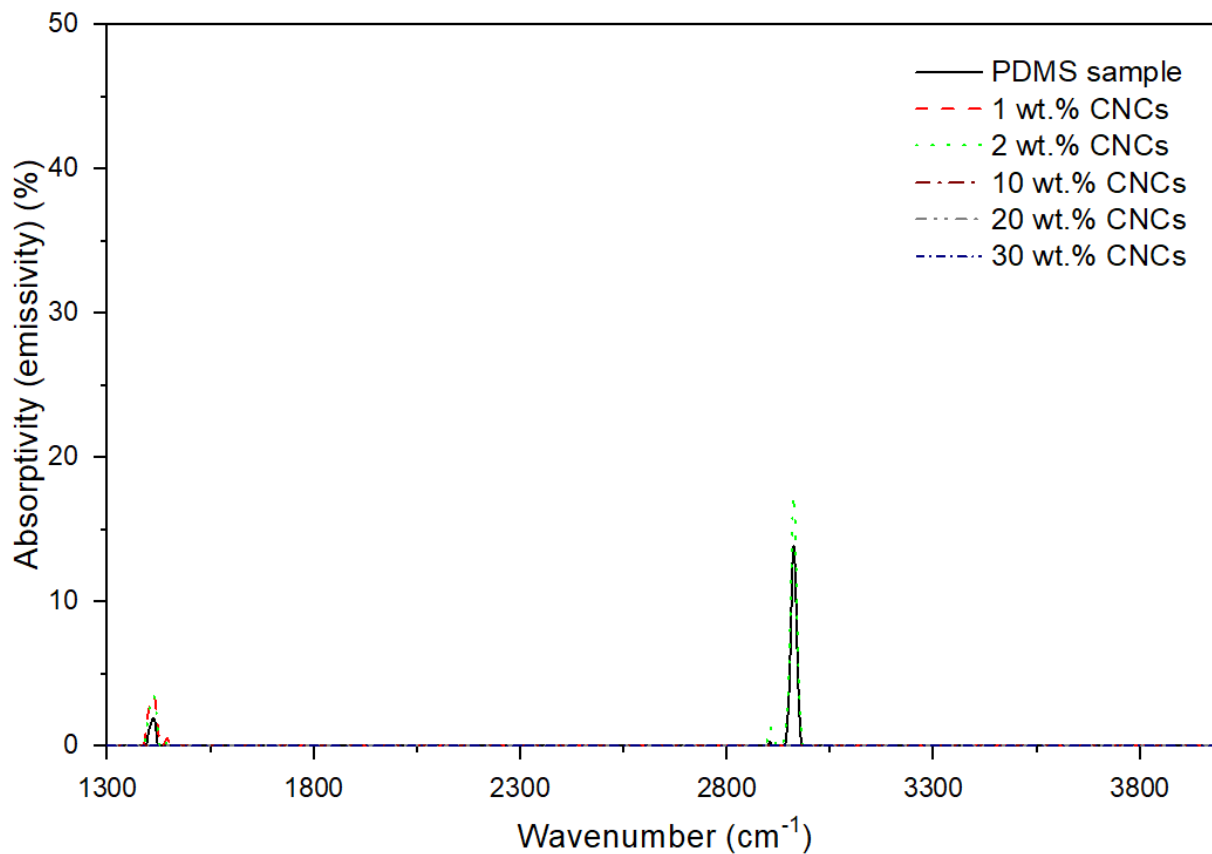
Figure 56. Spectral absorptivity (emissivity) of pure PDMS, 1 wt.%, 2 wt.%, 10 wt.%, 20 wt.% and 30 wt.% CNCs samples.

Figure 56 shows the absorption (emission) of the sample between 1300-4000 cm^{-1}, which is negligible compared to the absorption (emission) between 600-1300 cm^{-1}.
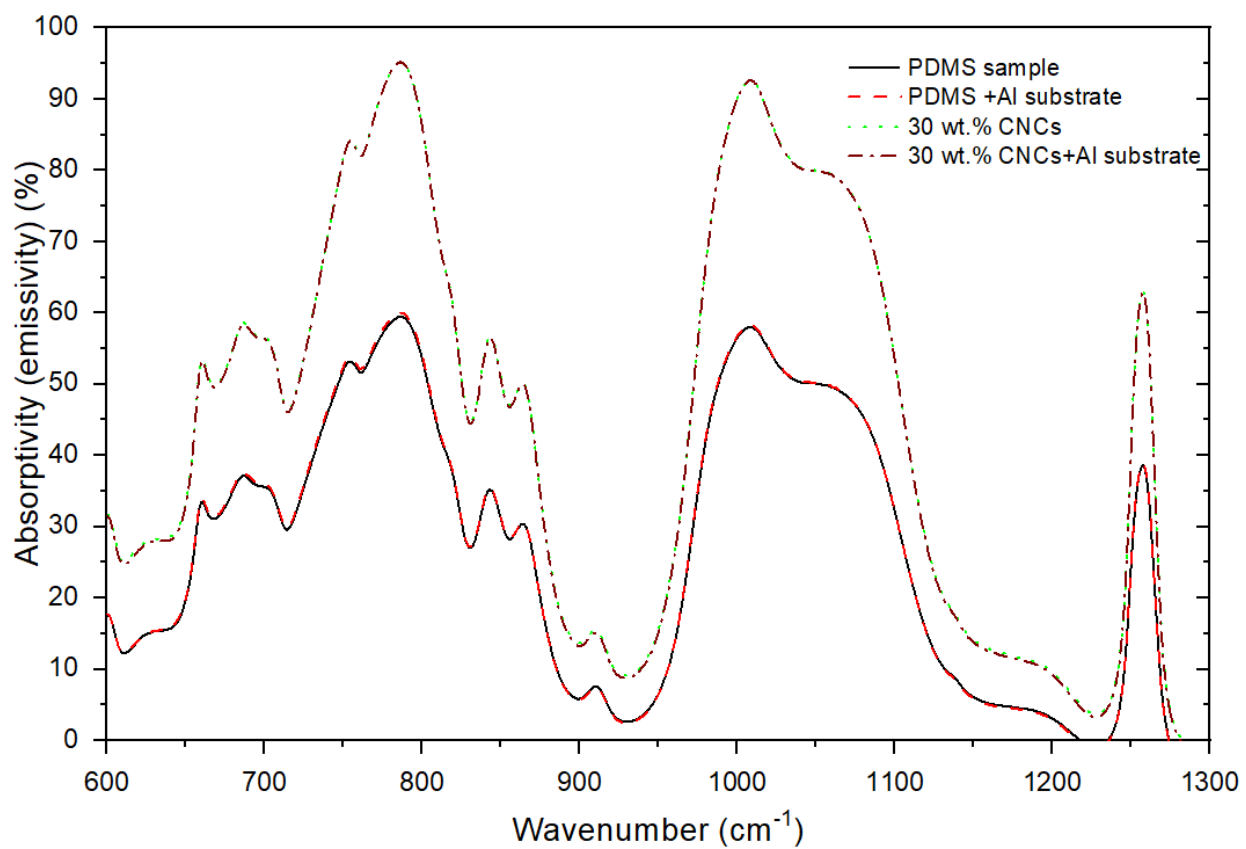
Figure 57. Spectral absorptivity (emissivity) of pure PDMS and 30 wt.% CNCs samples, with and without Al substrate.
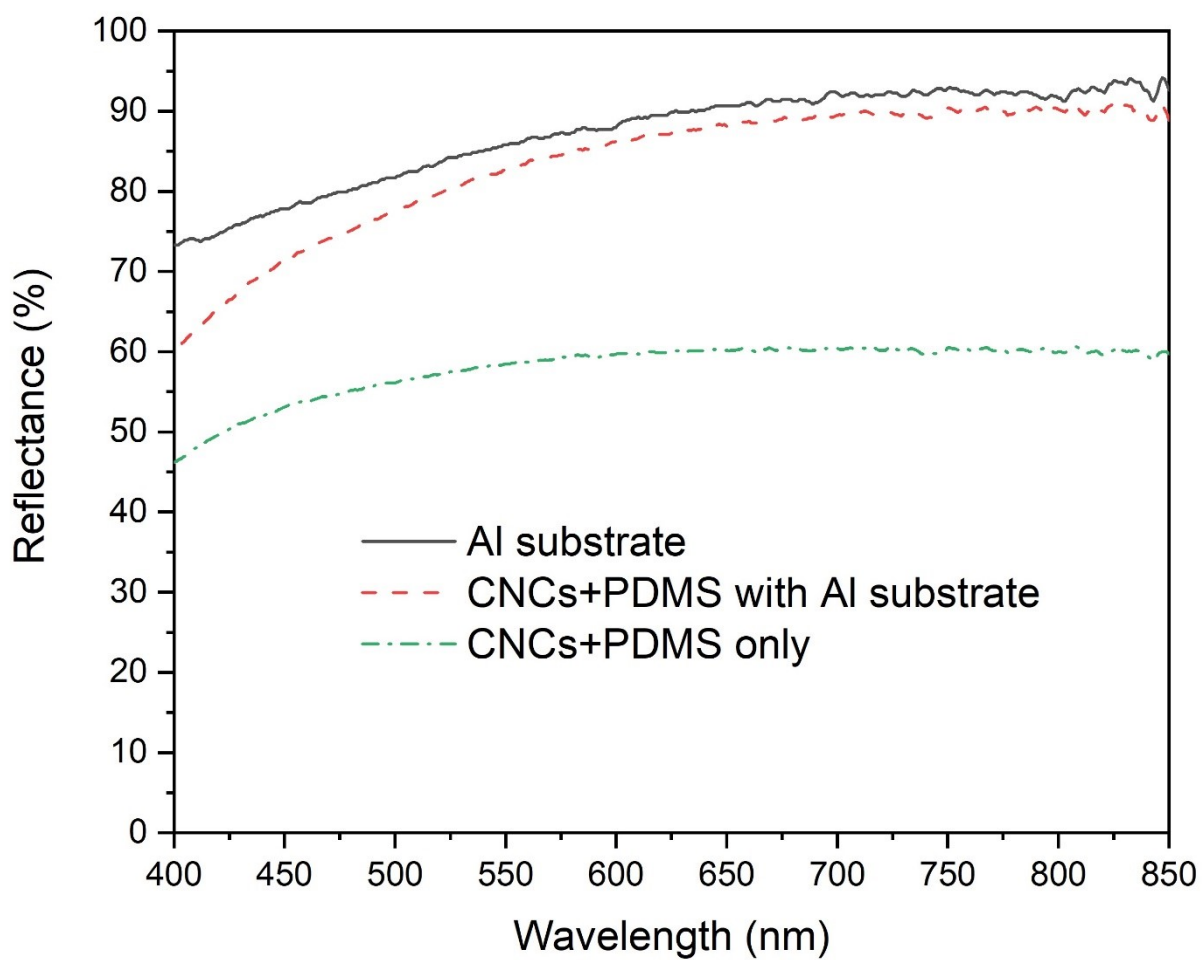
Figure 58. Reflection measurement of 30 wt.% CNCs+ PDMS sample, with and without Al substrate by spectrophotometer UV/VIS (Hitachi U-3900H).

Figure 57 and Figure 58 show the effect of Al substrate on fabricated samples. Though Al didn't change the emission of the overall structure it increased the solar reflectance significantly that increased the cooling ability of the cellulose-upgraded sample.
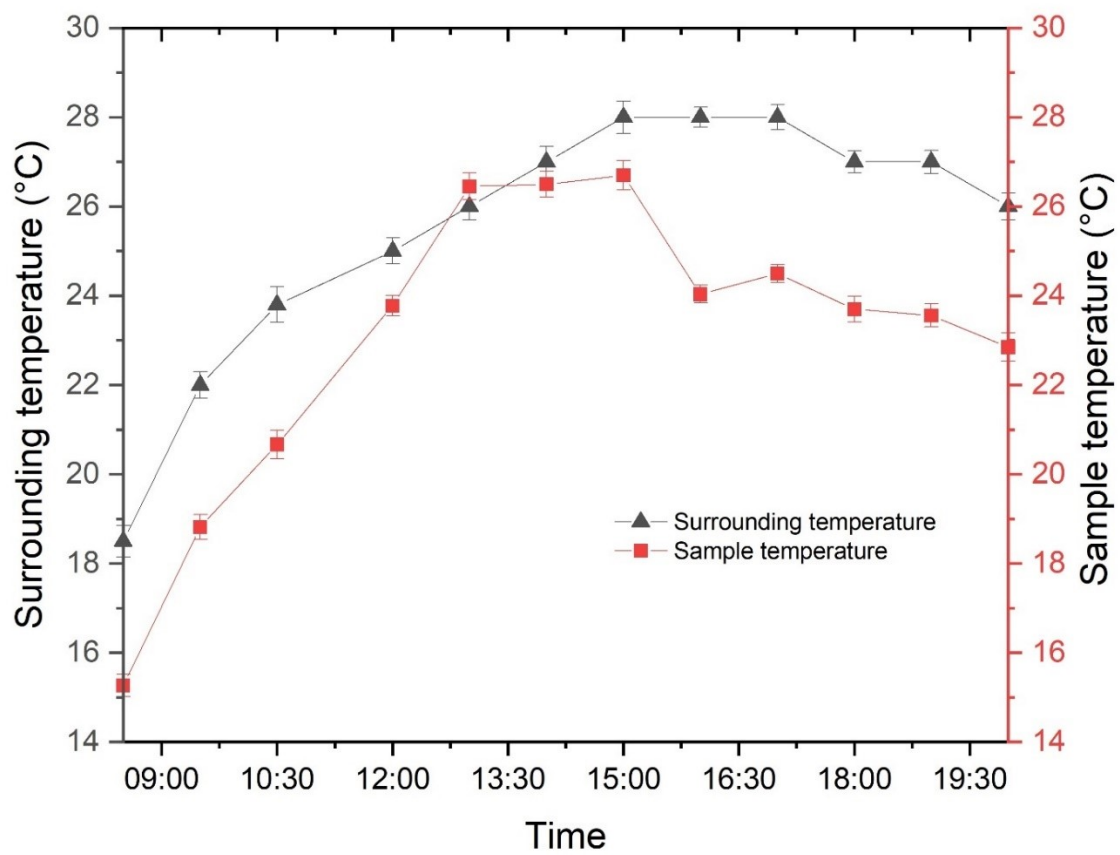
Figure 59. Surrounding and sample temperatures during the outdoor measurement.
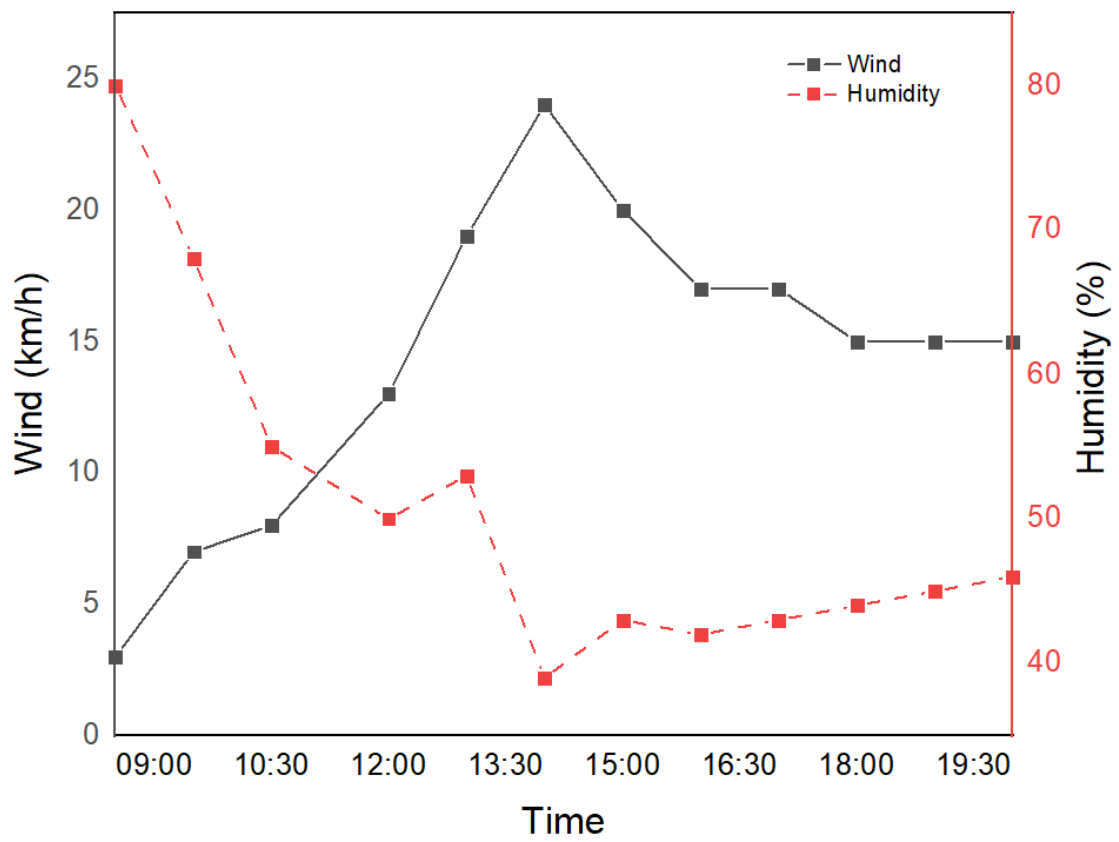
Figure 60. Wind speed and humidity during the outdoor measurement [123].
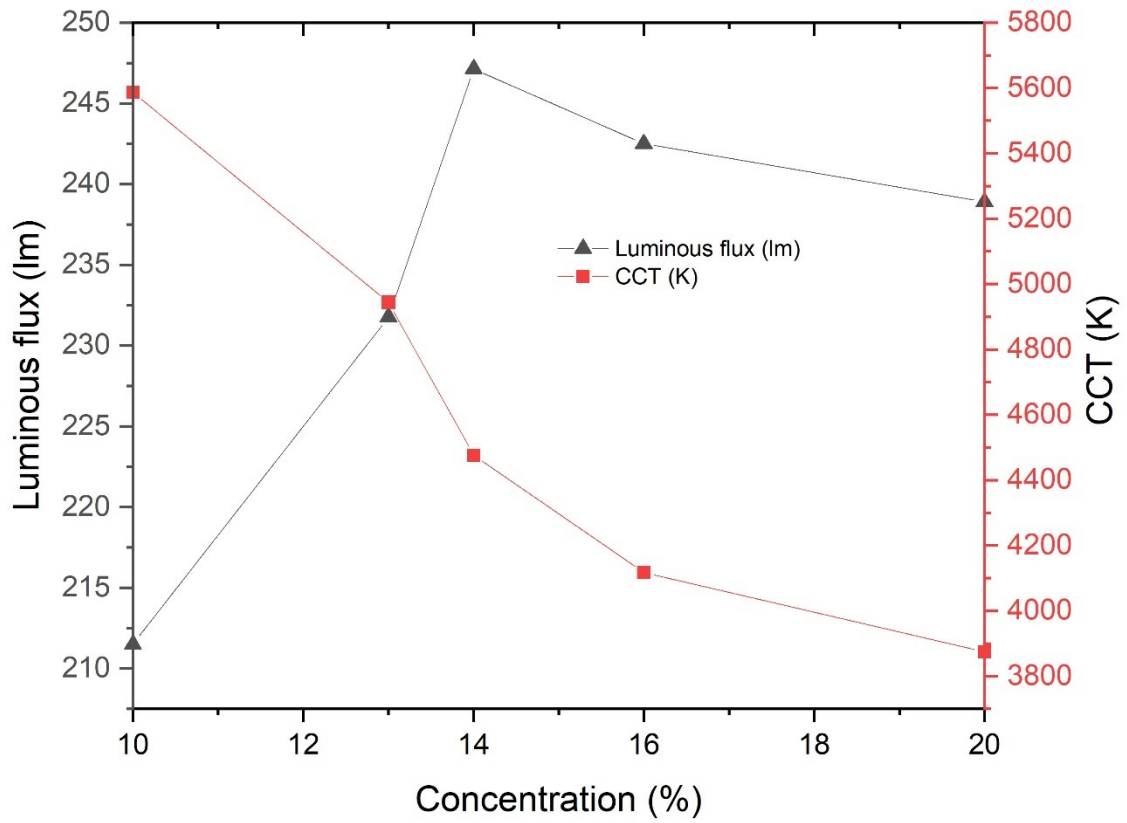
Figure 61. Change in luminous flux and CCT with phosphor concentrations.
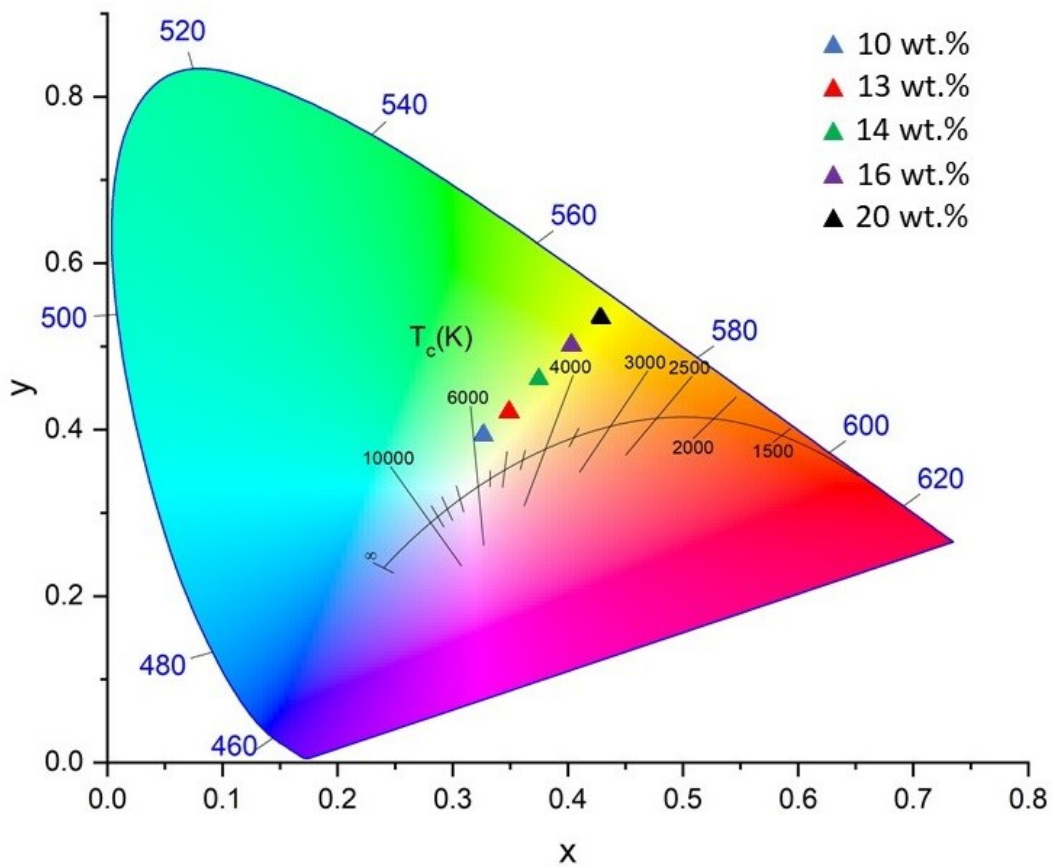
Figure 62. Chromaticity coordinates with different concentrations of phosphor.

Figure 61 shows the effect of phosphor concentration on luminous flux and CCT. It shows that luminous flux was highest for 14 wt.% phosphors. CCT shifts from towards lower temperature with increasing concentration of phosphors as shown in Figure 61 and Figure 62. This suggests an increase in yellow light intensity with increasing phosphor concentration.
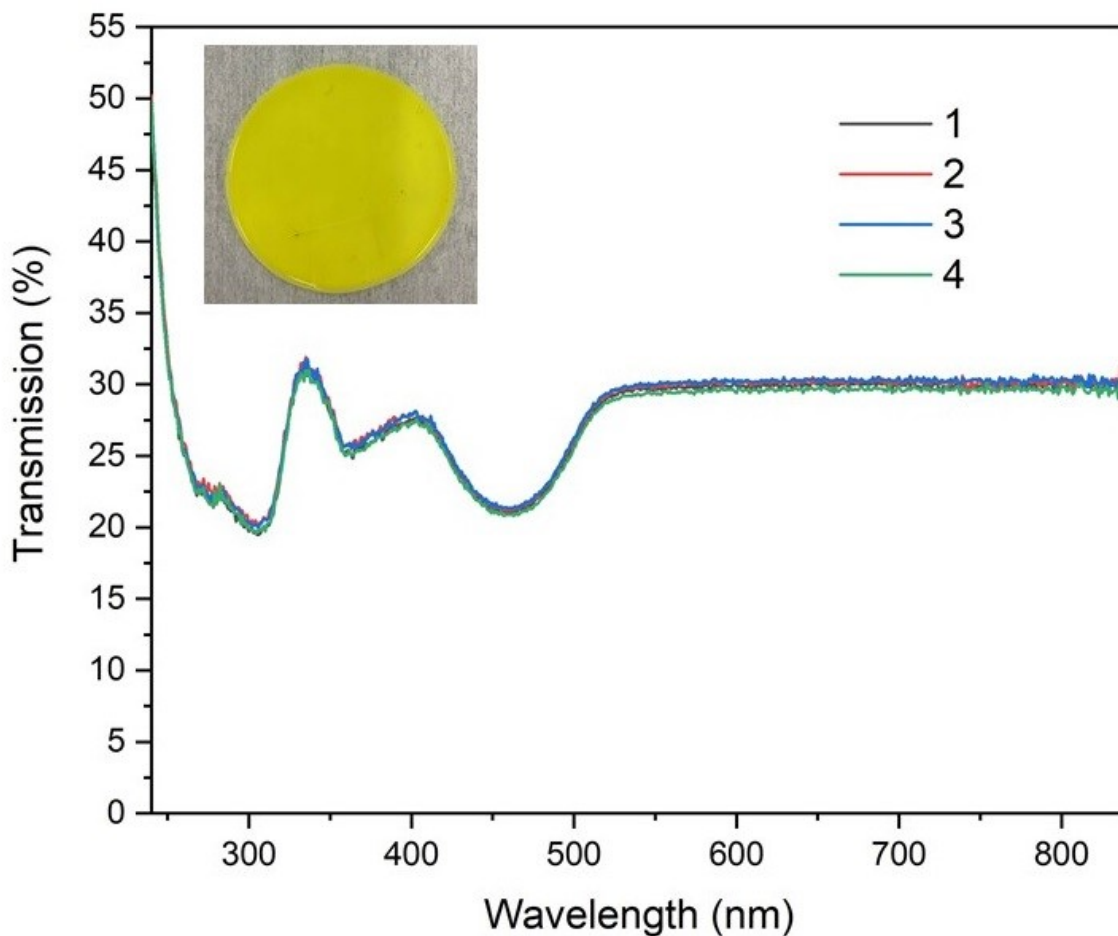
Figure 63. Transmission data at 4 different points of a sample with 14 wt.% phosphors and 6 wt.% CNCs. Inset shows the fabricated sample.

Figure 63 shows the transmission measured by spectrophotometer UV/VIS (Hitachi U-3900H) at 4 different points of a 2-inch diameter sample containing 14 wt.% phosphors and 6 wt.% CNCs. It shows that transmission remains consistent proving a uniform mixing of phosphors and CNCs in the fabricated sample.